Title
Photonic Integrated Devices and Circuits based on Arrayed Waveguide Gratings

Author
Liu, Guangyao

Publication Date
2021

Peer reviewed|Thesis/dissertation

Photonic Integrated Devices and Circuits based on Arrayed Waveguide Gratings

By

GUANGYAO LIU
DISSERTATION

Submitted in partial satisfaction of the requirements for the degree of

DOCTOR OF PHILOSOPHY

in

Electrical and Computer Engineering

in the

OFFICE OF GRADUATE STUDIES

of the

UNIVERSITY OF CALIFORNIA

DAVIS

Approved:

S. J. Ben Yoo, Chair

N. C. Luhmann Jr.

Joshua Hihath

Committee in Charge

2021

To my family members,

Hanqiao Liu, Fenglan Yu, Wei Liu, and Yuehua Dong

Whose love and support have carried me through this wonderful Ph.D journey.

Acknowledgements

I want to express my sincere gratitude to my thesis advisor, Prof. S. J. Ben Yoo, for his continuous support and research insights during my stay at the top-class Next Generation Networking and Computing Systems Group. Prof. Yoo welcomed me to the research group, guided me to the cutting-edge photonics world, and attentively helped me through downtimes. I am honored to have him as my major dissertation professor. In addition, my gratitude goes to Prof. Luhmann and Prof. Hihath for serving as my dissertation committee members and their guidance.

My pains and gains were rooted deeply in the harmonious research group. I appreciate all my colleagues for their friendship and support. Kuanping Shang was my first mentor and took care of me since the first day. He was my role model and enlightened me on every aspect to become a professional researcher. Stanely Cheung and Runxiang Yu instructed me in the initial photonic design and characterization, opening the door to the vivid photonic world. Dr. Katsunari Okamoto and Shibnath Pathak offered me insightful advice and unreserved guidance on the arrayed waveguide gratings. I worked closely with Tiehui Su on the SPIDER projects and obtained systematic design and layout methodology. Shaoqi Feng led the prism-waveguide coupler project and maintained carefulness and professionalism throughout large research projects. Binbin Guan set interesting research tasks and homework for me. His everlasting passion and extensive knowledge deeply influenced me. Mathias Prost taught me the importance of perseverance in the research career, especially in fabrication processes. I lived together with Yu Zhang, Chuan Qin, and Kuanping Shang for years. And I will never forget our warm family and relaxed weekends. I'd also like to thank the rest of my colleagues: Hongbo Lu, Chengchen Liu, Xian Xiao, Yichi

Zhang, Yi-Chun Ling, Mingye Fu, Hang Su, and Jingwei Wan, for the efforts and joy we shared together.

Most of the fabrication took place in Center for Nano-MicroManufacting (CNM2) at UC Davis and Marvell Nanofabrication Laboratory at UC Berkeley. I want to thank all the staff for the help and guidance received in the cleanrooms.

Abstract

The fast development of Photonic Integrated Circuits (PICs) has led to advances not only in the fundamental elements (such as ultra-low loss waveguide platforms and arrayed waveguide gratings (AWGs)) but also in the functionalities including large-scale optical interconnects, miniaturized imaging systems, low-loss and wide bandwidth communication transceivers, and precision metrology. A complete design/simulation, fabrication, and characterization routine is demonstrated on the ultra-low-loss multi-layer Si_3N_4 waveguide platforms in addition to the standard III-V and SOI PIC platforms, offering the superior performance of flexibility in the vertical integration and of minimizing the system throughput loss.

To catch up with the needs and expectations from the modern wavelength division multiplexing (WDM) communication infrastructure, AWGs stand out of its alternatives (cascaded Mach-Zehnder Interferometer lattice filter and Echelle gratings) in the finite impulse response (FIR) multiplexers (MUXs) and demultiplexers (DEMUXs) categories with better performance on the device crosstalk level, insertion loss, and device footprint. A concise and comprehensive AWGs modelling and simulation routine based on Fourier optics is presented. I will introduce the modelling and characterization results of both standard Gaussian and flat-top AWGs on the developed Si_3N_4 waveguide platform with capabilities as MUXs and wavelength routers in the optical communication O and C band as the building blocks for complex PICs.

I will present the new generation PICs based on our proposed Segmented Planar Imaging Detector for Electro-optical Reconnaissance (SPIDER) for a small-scale interferometric imaging system, relying on the sampling in the spatial Fourier domain via multiple baselines in PICs for an image

reconstruction offline. The Si_3N_4 PIC contains path-length matching waveguides, large channel spacing AWGs as DEMUXs, multimode interferometers (MMI), and phase tuning sections. Thorough characterization and study of the PIC performance are carried out, and the sustainability of the PIC for Low Earth Orbit (LEO) mission is confirmed.

In the end, I will propose and show novel and compact prism-waveguide couplers utilizing the evanescent wave coupling phenomenon together with mode size converter (negatively-tapered waveguide) for the efficient on-chip coupling towards the low-index (fluoride compounds) ultra-high-Q resonators for the first time. Thus, it paves the way towards the fully monolithic integrated optical frequency comb (OFC) sources for practical applications in optical communications, precision navigation, and optical sensing.

Table of Contents

List of Figures

List of Tables

Chapter 1 Introduction

1.1 Overview of Photonic Integrated Circuits

The invention of semiconductor diode lasers (DLs) in the 1960s [1] and the commercialization of optical fibers (OFs) in the 1970s [2] provide the foundations for the modern integrated photonics industry. Born out of traditional optics, photonics [3], [4] usually connotes the particle nature of light, the practical application of light (lasers, amplifiers, modulators, detectors, transmission lines, and sensors), and an analogy to electronics. Furthermore, the photonic integrated circuits (PICs) [5]–[7] assemble the aforementioned elements onto a common waveguide platform, achieving complex functionalities similar to the electronic circuits (ICs). The PICs offer significant advantages over the traditional individual bulky optical elements in the following aspects:

(1) small size, weight, and power (*SWaP*) budget.

(2) low-loss coupling and low-loss propagation.

(3) improved immunity to environmental vibrations.

(4) convenient optical alignment techniques.

(5) high-density fabrication economy.

We observe a similar exponential increase in the number of elements in the PIC industry after the millennium, known as the Moore's Law in the IC industry [8]. This rapid development in the PIC industry benefits from the improved individual components, mature mass fabrication experience from the CMOS area, and the increasing emphasis on the optical-electro integrated circuits. For

instance, successful demonstrations of the PICs include externally modulated lasers [9], [10], integrated balanced detectors [11], [12], integrated frequency comb sources [13], [14], and optical transceivers [15], [16].

Above all, the PICs should be built on fundamental waveguide platforms that support other critical elements. The III-V (InP and GaAs combinations) material compositions pop up as the first candidate for the PIC platform since the spread of the first-generation of active devices [17], [18]. This material platform inherently possesses the photon generation capability and rapidly grows to support the rest of the passive devices. It could easily integrate active and passive devices onto a single chip. However, the platform still suffers from the relatively high propagation loss and low batch fabrication ability. The second candidate is the silica waveguide platform, an analogy to the commercialized optical fiber whose core composition is doped SiO_2. The doped oxide waveguide core ensures the lowest propagation loss merit, close to the optical fiber performance (0.4 dB/km), and offers excellent polarization independence. But the low waveguide index contrast results in the largest device footprint. Moreover, there is no direct photon generation taken place in the SiO_2 dielectric. Thus, we mainly use this platform to achieve high-performance passive devices. The Silicon on insulator (SOI) waveguide platform [3] has attracted attention in the past two decades due to its CMOS fabrication capability and the natural SiO_2 serving as the heat passivation barrier. The relatively high waveguide index contrast gives rise to a minimum bending radius at the order of 10μm, indicating the level of the device footprint. The electro-optical effects discovered in the Silicon material guarantee the approach towards direct modulation. And the Germanium on Silicon epitaxy technique [19] provides basics for the on-chip detection. Because Silicon is an indirect bandgap semiconductor, we still do not have photon generation within the platform. Efforts have been made to either externally packaging the diode laser or realizing the photon generation through

wafer bonding. As a result, the SOI platform continues to be the hottest choice for PIC integration regardless of its high propagation loss. The SiN_x material platform comes into the practical application with its index contrast flexibility from 1% to 100%. This unique characteristic enables the platform to simultaneously realize a small device footprint and low-loss propagation with different waveguide thicknesses. Likewise, the nitride platform still lacks the method to achieve the on-chip light generation. I will introduce the above material platforms in detail and some novel platforms, including polymer and Lithium Niobate (LN), in Chapter 2.

People develop and investigate a small set of basic building blocks for the PIC industry based on the above waveguide platforms. First, we achieve the waveguides with different geometries to carry the light on-chip similar to an optical fiber. Then, we create the passive devices for splitting and combining light, including splitters, couplers, filters, and multiplexers. Besides, we also establish the active device category consisting of lasers, modulators, amplifiers, and detectors. Moreover, some more complex structures (phase/amplitude modulator, multiwavelength laser, and polarization splitter/converter) have been realized to manipulate the phase, amplitude, and polarization of the light in the PIC. With the development of the multi-project wafer (MPW) fabrication process in most foundries, researchers could quickly assemble the above building blocks to achieve novel applications such as neuromorphic computing [20], [21] and quantum photonics [22], [23].

Non-radiative recombination dominates most of the previously described material platform excerpt for the III-V combinations. This obstacle drives us to investigate various integration techniques to provide the photon generation ability onto the disabled platforms. The first integration approach is direct butt coupling. This is a well-developed technique to connect different PICs laterally. We could either use optical fibers to connect different PICs or butt-couple the PICs

with the help of edge couplers. This type of integration is widely used in the current transceiver market. But it still needs human resources and is not fully automated. Furthermore, the PIC edge roughness will also create additional loss and optical phase delay. An alternative approach for the PIC integration is wafer bonding in the vertical direction, including direct wafer bonding and adhesive wafer bonding [24], [25]. The direct wafer bonding technique utilizes the Van der Waals force at the two bonding surfaces attached. A successful demonstration is the bonding lasers. On the other hand, the adhesive wafer bonding technique employs a thin layer of adhesive material, benzocyclobutene (BCB), in the typical situation to connect the two platforms. This bonding technique introduces thermal isolation between the two platforms, and the integrated circuit is highly temperature-sensitive. Researchers recently focus on the directly epitaxial growth technique for the III-V material to Silicon integration, providing promising quantum dot lasers on the indirect bandgap material platforms [26].

1.2 Optical Communications and Arrayed Waveguide Gratings

The communication infrastructure has evolved from the original beacon tower fire alarm to the common electromagnetic wave carriers. The driving force behind this evolution is the ever-increasing demand for transmission speed and capacity. The modern optical communication system utilizes the electromagnetic wave with the center frequency around 200 THz. The time-division multiplexing (TDM) technique [27] solves transmission requirements exceeding a single optical channel's capability in the 1990s. The network providers use TDM to combine signals from different users at different time slots and send the aggregated signals in a single transmission cable. This technique is widely used in the early telephone network hierarchy to integrate 64 kb/s voice channels. The transmission capacity, calibrated by the bit-rate-distance product, has increased ten times every four years since the early 1970s. The development of the lasers, detectors, and

amplifiers at 1310 nm and 1550 nm wavelengths has shifted the transmission carrier wavelength. The wavelength-division multiplexing (WDM) technique (shown in Fig 1. 1) further boosts the communication capacity by employing multiple optical sources at slightly different wavelength channels around the center wavelength [28], [29].

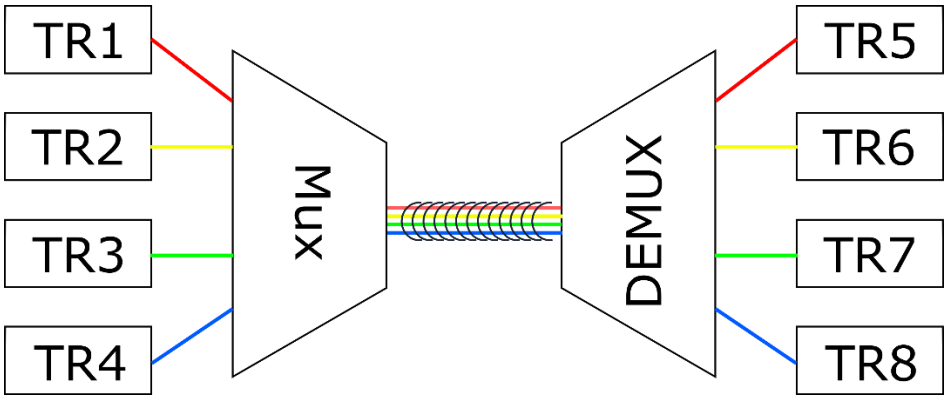

Fig 1. 1 WDM system diagram.

The WDM system utilizes the multiplexers (MUX in Fig 1. 1) to combine the optical signals of the transmitters (TR1 to TR4) at the left-hand side. The mixed optical signals, staying at the standardized channel grids around the center wavelength, are carried to the destination through an optical fiber bundle. Repeaters and amplifiers will be implemented along the transmission fiber to enhance the signal power at specific intervals. In the end, the combined multiwavelength signals travel through the demultiplexer (DEMUX) and split the individual wavelength channel to the corresponding destination (TR5 to TR8). In the recent research and experiment, people have realized above Tb/s single-channel WDM transmission exploiting novel modulation formats and compensation techniques.

We see from Fig 1. 1 that the MUX and DEMUX play critical roles in the WDM communication system to combine and split individual transmission channels. Multiwavelength interferometers, ring resonators, directional couplers are examples of single wavelength channel filters. We could

cascade them into multi-stages to form the desired 1 × N and N × 1 capability. However, this approach is neither compact nor loss-free. The arrayed waveguide gratings (AWGs) [30] are the most popular choices for multiwavelength multiplexing and demultiplexing. The AWG consists of two star-couplers and arrayed waveguides in between. This device takes advantage of a point-to-point imaging system and simultaneously achieves low insertion loss and low crosstalk level. The commercial AWGs are often delivered on the silica waveguide platform due to its ultra-low loss performance and inherent low coupling loss towards the transmission fiber [31]. I will go through the AWG design details in the following chapter and demonstrate integrated AWGs on the low-loss nitride platform.

1.3 Optical Interferometric Imaging

Interferometry [32] is a technique superimposing the light rays passing through the splitter to form the interference pattern. Then, we could retrieve the amplitude, phase, and visibility information from the interference pattern. The building block in the interferometry is the interferometer, such as the Fabry Perot interferometer and Mach Zehnder interferometer. The interferometry technique is widely used in radio astronomy, where signals at different telescopes are combined to generate the interference signal for data analysis. The major advantage is that it could support a huge theoretical aperture equal to the largest baseline distance between telescope antennas. Therefore, people have created very long baseline interferometry (VLBI) radio telescopes [33] with baseline distances exceeding thousands of kilometers, successfully providing high-resolution pictures of nebulas and galaxies.

We follow the same design methodology to develop the Segmented Planar Imaging Detector for Electro-optical Reconnaissance (SPIDER) concept utilizing the interferometry in the light wavelength. The SPIDER system tends to bring the radio interferometry infrastructure to the

integrated photonics domain to take advantage of the commercial CMOS fabrication facility and the simplified electronic driving circuits. We have successfully demonstrated the proof-of-concept PIC on the silica waveguide platform with two baselines. This dissertation will introduce our efforts on the low-loss nitride platform to realize the 18 baselines interferometric imaging engine.

1.4 Optical Coupling to Resonators

Optical coupling is a critical phenomenon utilizing the lightwave interaction between the two adjacent propagating modes. People have developed the coupled mode theory [34] to explain and derive the governing parameters for optical coupling. Integrated photonics elements, such as directional couplers are realized using the coupled mode theory to understand the evanescent wave between adjacent waveguides. On the other hand, optical resonators [35], developed from the optical resonating cavities, have the unique characteristics of highly enhanced optical power, small footprint, and non-linear properties. These optical resonators need an efficient optical coupling mechanism to couple light power in and out of the cavity. The bulky optical prism is the first candidate for this optical coupler towards resonators. It utilizes the inherent evanescent wave coupling [36] mechanism at the prism edge under the total internal reflection condition to achieve the power exchange. This prism optical coupling is also utilized in the thin-film metrology and calibration applications to retrieve the material properties. However, the bulky prism coupling technique needs manual alignment and mechanical stabilization, which hinders its opportunity for batch integration. With the spread of the optical fibers, researchers have developed angled-cut fibers and tapered fibers to act as optical couplers to crystalline resonators. These fiber-based devices simplify the alignment process. But they are not compatible with the modern CMOS fabrication technology and suffer from integration complexity. Researchers have investigated waveguide coupled resonators with the million-level quality factor (Q factor) on the common PIC

platforms (SOI and nitride). These waveguide-coupled resonators employ a similar coupled mode theory to realize the power exchange between the coupling waveguide and resonators. We could control the gap between them to achieve the critical coupling condition for the best dynamic range. We will introduce and demonstrate a prism-waveguide coupler for the ultra-high Q crystalline resonator in the dissertation. Above all, we combine the advantage of waveguide couplers and optical prism to achieve the on-chip coupled resonator system exceeding a billion loaded Q factor.

1.5 Organization of the Thesis

This dissertation will discuss advanced PICs for communications, interferometric imaging, and resonator coupling utilizing AWGs. Chapter 2 introduces the fundamental PIC platforms, the design/simulation routine, and the developed low-loss fabrication technique. We could establish a complete "design, modelling, layout, fabrication, and characterization" process flow with iterations to improve the overall performance. Chapter 2 serves as the technical reference for the following chapters. Chapter 3 discusses the theory, design, modelling, and experimental results of AWG routers and multiplexers. We could realize low insertion loss, low crosstalk level, a large number of channels, and highly flexible AWGs on the nitride platform. Chapter 4 will use the above AWGs as the filter engine in the SPIDER PICs. We successfully develop the next generation SPIDER PIC on the multilayer waveguide platform, leading to an integrated interferometric telescope. In the end, Chapter 5 presents the first demonstration of the on-chip coupler for the ultra-high-Q crystalline resonator, realizing the loaded Q factor exceeding a billion. We build a Kerr frequency comb source based on this waveguide coupled resonator in a commercial butterfly package.

References

[1] L. A. Coldren, S. W. Corzine, and M. L. Mashanovitch, *Diode lasers and photonic integrated circuits*, vol. 218. John Wiley \& Sons, 2012.

[2] T. Okoshi, *Optical fibers*. Elsevier, 2012.

[3] B. Jalali and S. Fathpour, "Silicon photonics," *J. Light. Technol.*, vol. 24, no. 12, pp. 4600–4615, 2006.

[4] B. E. A. Saleh and M. C. Teich, *Fundamentals of photonics*. john Wiley \& sons, 2019.

[5] T. L. Koch and U. Koren, "Semiconductor photonic integrated circuits," *IEEE J. Quantum Electron.*, vol. 27, no. 3, pp. 641–653, 1991.

[6] R. Nagarajan *et al.*, "Large-scale photonic integrated circuits," *IEEE J. Sel. Top. Quantum Electron.*, vol. 11, no. 1, pp. 50–65, 2005.

[7] F. Kish *et al.*, "System-on-chip photonic integrated circuits," *IEEE J. Sel. Top. Quantum Electron.*, vol. 24, no. 1, pp. 1–20, 2017.

[8] M. Smit, J. der Tol, and M. Hill, "Moore's law in photonics," *Laser \& Photonics Rev.*, vol. 6, no. 1, pp. 1–13, 2012.

[9] H. Kogelnik and C. V Shank, "Coupled-wave theory of distributed feedback lasers," *J. Appl. Phys.*, vol. 43, no. 5, pp. 2327–2335, 1972.

[10] R. Tkach and A. Chraplyvy, "Regimes of feedback effects in 1.5-$μ$m distributed feedback lasers," *J. Light. Technol.*, vol. 4, no. 11, pp. 1655–1661, 1986.

[11] B. L. Kasper, C. A. Burrus, J. R. Talman, and K. L. Hall, "Balanced dual-detector receiver for optical heterodyne communication at Gbit/s rates," *Electron. Lett.*, vol. 22, no. 8, pp. 413–415, 1986.

[12] H. R. Carleton and W. T. Maloney, "A balanced optical heterodyne detector," *Appl. Opt.*, vol. 7, no. 6, pp. 1241–1243, 1968.

[13] V. Brasch *et al.*, "Photonic chip--based optical frequency comb using soliton Cherenkov radiation," *Science (80-.).*, vol. 351, no. 6271, pp. 357–360, 2016.

[14] T. J. Kippenberg, R. Holzwarth, and S. A. Diddams, "Microresonator-based optical frequency combs," *Science (80-.).*, vol. 332, no. 6029, pp. 555–559, 2011.

[15] J. Kim and J. F. Buckwalter, "A 40-Gb/s optical transceiver front-end in 45 nm SOI CMOS," *IEEE J. Solid-State Circuits*, vol. 47, no. 3, pp. 615–626, 2012.

[16] C. Doerr *et al.*, "Silicon photonics coherent transceiver in a ball-grid array package," in *2017 Optical Fiber Communications Conference and Exhibition (OFC)*, 2017, pp. 1–3.

[17] M. Smit *et al.*, "Generic foundry model for InP-based photonics," *IET Optoelectron.*, vol. 5, no. 5, pp. 187–194, 2011.

[18] M. Smit *et al.*, "An introduction to InP-based generic integration technology," *Semicond. Sci. Technol.*, vol. 29, no. 8, p. 83001, 2014.

[19] H. Ye and J. Yu, "Germanium epitaxy on silicon," *Sci. Technol. Adv. Mater.*, 2014.

[20] C. D. Schuman *et al.*, "A survey of neuromorphic computing and neural networks in hardware," *arXiv Prepr. arXiv1705.06963*, 2017.

[21] E. Goi, Q. Zhang, X. Chen, H. Luan, and M. Gu, “Perspective on photonic memristive neuromorphic computing,” *PhotoniX*, vol. 1, no. 1, pp. 1–26, 2020.

[22] A. Politi, J. C. F. Matthews, M. G. Thompson, and J. L. O’Brien, “Integrated quantum photonics,” *IEEE J. Sel. Top. Quantum Electron.*, vol. 15, no. 6, pp. 1673–1684, 2009.

[23] J. W. Silverstone *et al.*, “Silicon quantum photonics,” in *2016 International Conference on Optical MEMS and Nanophotonics (OMN)*, 2016, pp. 1–2.

[24] D. Liang and J. E. Bowers, “Recent Progress in Heterogeneous III-V-on-Silicon Photonic Integration,” *Light Adv. Manuf.*, vol. 2, no. 1, pp. 1–25, 2021.

[25] D. Liang and J. E. Bowers, “Recent progress in lasers on silicon,” *Nat. Photonics*, vol. 4, no. 8, pp. 511–517, 2010.

[26] J. C. Norman *et al.*, “A review of high-performance quantum dot lasers on silicon,” *IEEE J. Quantum Electron.*, vol. 55, no. 2, pp. 1–11, 2019.

[27] R. S. Tucker, G. Eisenstein, and S. K. Korotky, “Optical time-division multiplexing for very high bit-rate transmission,” *J. Light. Technol.*, vol. 6, no. 11, pp. 1737–1749, 1988.

[28] C. A. Brackett, “Dense Wavelength Division Multiplexing Networks: Principles and Applications,” *IEEE J. Sel. Areas Commun.*, vol. 8, no. 6, pp. 948–964, 1990, doi: 10.1109/49.57798.

[29] H. Ishio, J. Minowa, and K. Nosu, “Review and status of wavelength-division-multiplexing technology and its application,” *J. Light. Technol.*, vol. 2, no. 4, pp. 448–463, 1984.

[30] M. K. Smit, “New focusing and dispersive planar component based on an optical phased array,” *Electron. Lett.*, vol. 24, no. 7, pp. 385–386, 1988.

[31] C. R. Doerr and K. Okamoto, “Advances in silica planar lightwave circuits,” *J. Light. Technol.*, vol. 24, no. 12, pp. 4763–4789, 2006.

[32] M. Françon, “Optical interferometry,” in *Neutron interferometry*, 1979.

[33] C. Ma *et al.*, “The international celestial reference frame as realized by very long baseline interferometry,” *Astron. J.*, vol. 116, no. 1, p. 516, 1998.

[34] A. Yariv, “Coupled-mode theory for guided-wave optics,” *IEEE J. Quantum Electron.*, vol. 9, no. 9, pp. 919–933, 1973.

[35] I. S. Grudinin, V. S. Ilchenko, and L. Maleki, “Ultrahigh optical Q factors of crystalline resonators in the linear regime,” *Phys. Rev. A*, vol. 74, no. 6, p. 63806, 2006.

[36] D. R. Rowland and J. D. Love, “Evanescent wave coupling of whispering gallery modes of a dielectric cylinder,” *IEE Proc. J-Optoelectronics*, vol. 140, no. 3, pp. 177–188, 1993.

Chapter 2 Design, Fabrication, and Characterization of Photonic Integrated Circuits

2.1 Photonic Integrated Circuits Platforms

The invention of Diode Lasers (DLs) [1], [2] in the 1960s and optical fibers (OFs) [3]–[6] in the 1970s paved the way for photonic integration similar to the development of IC technology in the area of electronic circuits. DLs and OFs offer us the alternatives to densely connect various optical components and get rid of the bulky glass optics components. Since then, the III-V (InP and GaAs) materials stand out as the first candidate for the fundamental platform that supports individual optical elements (i.e., Lasers, modulators, waveguides, filters, and detectors) [7]–[9]. After the commercialization of the optical fiber with the SiO_2/GeO_2 fiber core, the silica waveguide platform has emerged as a clear favorite to function as the fundamental building block since it possesses the inherently low-loss coupling to the optical fiber in the near-infrared wavelength range [10]–[13]. However, the fact that SiO_2 is an insulator and the corresponding low heat-modulation efficiency hinder the development of any active optical devices on this platform. Besides, the investigation into the electro-optical effects in Silicon [14] gives rise to the increasing emphasis on the possibility of photonic integration based on this golden material, which supports the industry of electronics integration [15], [16]. The Silicon on Insulator (SOI) platform come into being after the millennium [17]–[19]. Its CMOS compatibility and relevant high material index contrast offer a new opportunity for mass production and dense integration. Alongside the development of the SOI platform, researchers and entrepreneurs have gradually focused on novel material platforms such as SiN_x, providing the superior performance of the propagation loss and non-linear property compared to the SOI platform [20], [21]. With the recent improvements on the fabrication

techniques of the thin-film Lithium Niobate (LN) [22] on the insulator application, LN platform starts to attract attention with its unique characteristics, supporting electro-optical, acoustic-optical, and non-linear optical properties at the same time. Passive integrated waveguides, resonators, electro-optical modulators, and wavelength converters are realized on this new integrated platform with competitive performance. Polymers also pop up as an essential material for the PICs due to their mechanical flexibility and wide transparency window [23], [24]. Several passive optical components are investigated and delivered in polymer photonics that complements the rest of the photonic integrated platforms. Table 1 summarizes the critical parameters of the PIC platforms discussed above.

Table 1 List of critical properties of the PIC platforms discussed in the chapter

PIC Platform	III-V	Silica	SOI	SiN_x	$LiNbO_3$	Polymer
Waveguide Materials	*InP/GaAs/ AlAs*	Doped SiO_2/SiO_2	Silicon/ SiO_2	SiN_x/SiO_2	$LiNbO_3/SiO_2$ SiN_x	Polymers
Waveguide Confinement	Medium	Low	Strong	Medium – low	Medium – low	Low
Bending Radius (μm)	~400	~2000	~10	100~3000	80~3000	~3000
Mode Radius (μm)	1	3	0.25	1~3	0.5~4	3
Modulation capability	Strong	No	Medium	No	Strong	Medium
Optical Gain	Strong	No	No	No	No	No
Integration	High	Low	High	Medium	Medium	Low

Selecting the waveguide platform serves as the first step in the PIC design process flow. The III-V material compounds such as *InP* and *GaAs* inherently possess the direct bandgap property, guaranteeing their superior performance on the light generation. The III-V waveguide platform

could generate the optical light wavelength in the infrared range with different Group III and Group V materials compositions. Despite the limitations on the wafer-scale fabrication capability and the relatively high propagation loss (> 0.5 dB/cm), the III-V waveguide platform could provide various combinations of passive and active optical components (lasers, modulators, detectors, Demux/Mux, filters). As a result, this waveguide platform supports high-level integration towards complicated systems such as transmitters and comb generators. Extensive efforts are made to examine and successfully establish the multi-project wafer (MPW) facility for the III-V waveguide platform [25].

The silica waveguide platform has a unique similarity to the optical fiber that is dominantly utilized in modern communication infrastructures. The doped SiO_2/SiO_2 waveguide core ensures below 0.1 dB coupling loss towards transmitting fibers. And the ultra-low propagation loss resulting from the extremely low mode confinement factor in the waveguide core makes it a perfect candidate for the passive propagating elements such as filters and AWGs. It also holds low temperature dependence and low polarization dependence. However, the significant bending radius gives rise to the increasing device footprint and hinders its feasibility of low-cost heterogeneous integration. There is also no inherent photon generation mechanism and electro-optical modulation capability within this waveguide platform.

The SOI platform benefits from the mature CMOS fabrication technology in the electronics IC and provides the most cost-effective and compact optical elements. The strong optical mode confinement factor resulting from the large core-cladding index contrast offers sharp bending on the order of 10 μm. The travelling wave modulators and Ge-on-Si photodetectors equip the SOI platform with promising active optical capability. However, similar to the silica platform, Silicon is an indirect bandgap material so that the photon generation stays as the top question to be solved.

Furthermore, the coarse waveguide sidewalls make the propagation loss in the platform orders of magnitude higher than that in the communication fibers. Some emerging technologies such as wafer bonding and epitaxial growth on the Silicon substrate present promising approaches for heterogeneous integration of other materials onto the SOI platform to mitigate the disadvantages [26], [27].

The thin film on LN platform has recently been commercialized with the advances in ion-slicing and wafer bonding technologies. This breakthrough in the fabrication process brings the LN waveguide platform back to the integrated platform table. Various integrated optical elements have been realized in the past decade, enabling complex systems such as broadband frequency comb sources and high-speed modulators. The monolithic ridge waveguide configuration and the rib loading waveguides support approximately 100 μm bending radius, sufficient for dense integration. The LN platform could provide strong electro-optical modulation, all-optical non-linearity, and piezo-optical mechanism simultaneously. However, the lack of the photon generation capability makes us turn to external lasers or heterogeneous integration for the robust photon source. And the material property of LN makes it relatively difficult for consecutive etching processes and vertical integration [28], [29].

The polymer platform mainly uses polymer materials such as PMMA and SU8 as the waveguide core to achieve lower-cost production and higher flexibility in the production process. The polymer process chain could deliver low-loss waveguides with mechanical flexibilities superior to other semiconductor platforms. However, the UV-cure process makes the platform unstable in a higher temperature environment. And there are only limited functional optical elements achieved on the platform.

The nitride platform is the critical waveguide platform discussed and investigated in this dissertation. Thin nitride material core offers the confinement factor similar to that in the silica platform, realizing the sub dB/m propagation loss. On the other hand, the thick nitride material core resembles the SOI platform with sharp bending and a small device footprint. The smooth waveguide sidewalls created through the lithography and etching process result in the low insertion loss and low crosstalk level of the elements achieved on this platform. Like the silica platform, the nitride platform still lacks feasible approaches for monolithic photon generation and electro-optical modulation. The heterogeneous integration with other waveguide platforms serves as a solution to this obstacle.

2.2 Simulation Methodology

After choosing the best waveguide platform for the PIC application, we need to run simulations under certain approximations to gather the design parameters for the PIC elements. The Maxwell equations govern the propagation of the lightwave within the medium. I will introduce three popular numerical solvers for the three-dimensional Maxwell equations of the electromagnetic waves, including Eigenmode Expansion (EME) Solver [30], [31], Beam Propagation Method (BPM) Solver [32], [33], and Finite Difference in Time Domain (FDTD) Solver [34], [35]. We usually start with analytical calculations of the device parameters and obtain the coarse parameter range. Then, we will choose the best numerical simulator to confirm the design parameters with efficiency in time and memory.

2.2.1 Eigenmode Solver and Eigenmode Expansion

The EME starts with the two-dimensional mode solution in a structure where the refractive index does not vary in the propagation *z*-direction. The mode solution in the rectangular coordinate system could be written as:

$$\Phi_n(x,y,z) = \Phi_n(x,y)e^{j\beta_n z}e^{-j\omega t} \tag{2.1}$$

The term $\Phi_n(x,y)$ is the electric field distribution in the cross-section plane perpendicular to the propagation direction. The term $e^{j\beta_n z}$ demonstrates the concise waveform with the harmonic dependence on the propagation distance *z*. The term $e^{-j\omega t}$ shows that we are analyzing single wavelength light propagation with exponential time dependence. This assumption requires that the transmission medium varies slowly in the *z*-direction. Thus, we could define the β_n value and the electric field distribution as the eigenvalue and the eigenfunction of the electromagnetic wave.

Solving Eq.(2.1), we could obtain a complete set of the eigenfunctions in the given structure, consisting of guided modes and radiative modes. The guided mode propagates lossless through the structure. On the other hand, the radiative mode transmits the power away from the simulation regime. Therefore, we could solve the Maxwell equations within the structure with the linear combination of the guided modes and radiative modes calculated from Eq.(2.1). These solutions could be written as the superposition of the bi-directional modes shown as below:

$$\Phi(x,y,z) = \sum_{n=1}^{m}\left(A_n e^{-j\beta_n z} + B_n e^{j\beta_n z}\right)\Phi_n(x,y)e^{-j\omega t} \tag{2.2}$$

Where the solution of the electric field is the combination of *m* number of forward-propagating and backward-propagating eigenfunctions. The term A_n is the amplitude coefficient of the forward-propagating modes, and the term B_n is the amplitude coefficient of the backward-propagating modes. Eq.(2.2) will be the exact solution of the electric field in this linear structure if we include all guided and radiative modes. When the electromagnetic wave arrives at an interface between two mediums, as shown in Fig 2. 1, we utilize the scattering matrix to conclude the relationship between the coefficients.

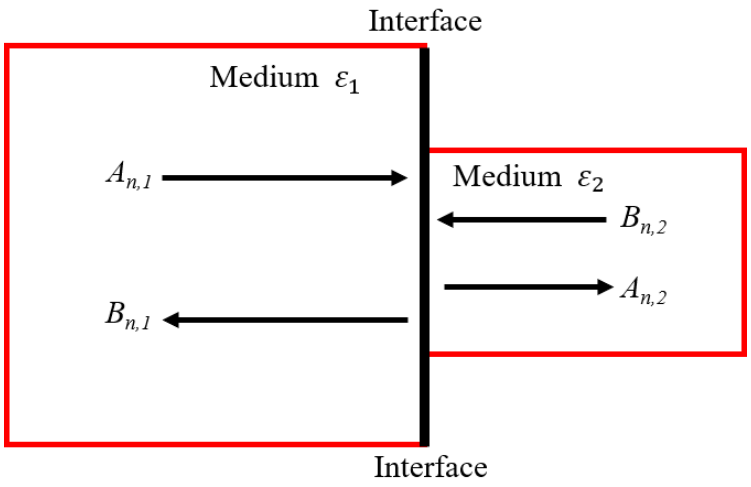

Fig 2. 1 Eigenmode analysis on the medium interface based on bi-directional propagating modes.

The continuity condition at this interface requires that the tangential components of the electric field should be equal on both sides of the interface:

$$\sum_{n=1}^{m}\left(A_{n,1}e^{-j\beta_n z}+B_{n,1}e^{j\beta_n z}\right)\Phi_{n,1}(x,y)=\sum_{n=1}^{m}\left(A_{n,2}e^{-j\beta_n z}+B_{n,2}e^{j\beta_n z}\right)\Phi_{n,2}(x,y) \tag{2.3}$$

We could conclude a scattering matrix *S* from Eq.(2.3), representing the relationship between parameters *A* and *B*. In the end, we could combine Eq.(2.2) and Eq.(2.3) to solve the propagation of the electromagnetic wave in the linear medium with any interfaces.

In theory, we could obtain the exact solution to the Maxwell equation if we have the infinite number of basic modes in Eq.(2.1). But in the practical situation, we must limit the number of basic modes used in the calculation, and this restriction brings numerical errors in this simulation process. Another advantage of the EME method is that we simultaneously solve the transmitted and reflected modes, and delivers a fully vectorial simulation environment. Thus, EME could provide the fastest simulation for structures with slow or zero variations in the propagation direction and it is also superior to other algorithms in calculating periodic structures. However, the EME method is unsuitable for optical structures with significant cross-sections such as AWGs and

PICs. We could perform EME simulation for the target structures in the commercial software such as Lumerical MODE® and Photon Design FIMMPROP®.

2.2.2 Beam Propagation Method

The BPM algorithm is another widely used simulation approach for the light travelling in the slowly varying mediums. It is also a powerful technique to investigate the light wave propagation and non-linear effects simultaneously. The BPM analysis starts with the three-dimensional Helmholz equations governing the propagation of the monochromatic electromagnetic waves.

$$\nabla^2(\Phi) + k_0^2 n^2(x,y,z)\Phi = 0 \tag{2.4}$$

The Φ in Eq.(2.4) represents the monochromatic electric field, k_0 denotes the wave number in the vacuum, *n(x,y,z)* denotes the three-dimensional refractive index distribution. In most guided propagation circumstances, the most rapid variation part in the electric field is the phase term associated with the propagation distance. And the rest is a slowly varying field envelope. Thus, we could further decompose the field Φ shown as below with the cladding index presented as n_0.

$$\Phi(\mathrm{x},\mathrm{y},\mathrm{z}) = \Psi(\mathrm{x},\mathrm{y},\mathrm{z})e^{-jk_0 n_0 z} \tag{2.5}$$

Substituting Eq.(2.5) into Eq.(2.4), we obtain the new governing equation of the field propagation.

$$\nabla^2(\Psi) - 2jk_0 n_0 \frac{\partial \Psi}{\partial z} + k_0^2(n^2 - n_0^2)\Psi = 0 \tag{2.6}$$

We use the assumption that the optical field varies slowly in the *z*-direction in Eq.(2.6), so that the field's second-order derivative on the *z*-direction is equal to zero. And we can further simplify Eq.(2.6) if we assume the optical field is weakly guided in the core region (i.e., optical fibers and silica waveguides).

$$\frac{\partial \Psi}{\partial z} = -\mathrm{j}\frac{1}{2k_0 n_0}\nabla^2(\Psi) - jk_0(n - n_0)\Psi \tag{2.7}$$

The first term on the right-hand side of Eq.(2.7) represents the free propagation of the light wave in the medium with the refractive index n_0. And the second term means the phase change of the light wave resulting from the index variation. These two terms influence the propagation of the light field simultaneously. In realizing the BPM algorithm, we assume that these two terms could affect the light wave separately and alternatively in a short distance of *L* in the propagating *z*-direction. Under this assumption, we could use Eq.(2.8) to simulate the field propagation in the two halves of the propagating distance *L*, and use Eq.(2.9) to add the phase shift due to the index variation in the middle of the propagation length.

$$\frac{\partial \Psi}{\partial z} = -\mathrm{j}\frac{1}{2k_0 n_0}\nabla^2(\Psi) \tag{2.8}$$

$$\frac{\partial \Psi}{\partial z} = -jk_0(n - n_0)\Psi \tag{2.9}$$

We could implement either Fast Fourier Transform (FFT) or Finite difference (FD) method to simulate the short propagating distance *L* alternatively and obtain the final simulation result at the end of the waveguides. The BPM method could provide time-efficient simulation on the mode and intensity in the waveguiding structures with high accuracy. But it highly relies on the weakly guiding assumption and the slowly varying assumption. Thus, it is not suitable for problems with high index contrast or rapidly changing boundaries. We could perform the BPM simulation in commercial software such as Rsoft BeamPROP®.

2.2.3 Finite-difference in Time-domain Method

KS. Yee [35] demonstrated the FDTD method for solving three-dimensional electromagnetic wave propagation for the first time during the 1960s. And this technique quickly spreads in the photonics area and has been investigated with numerous improvements [36], [37]. In the three-dimensional rectangular coordinate system (the unit cell shown in Fig 2. 2), we could write the two partial differential equations governing the electromagnetic wave propagation shown as below.

$$\nabla \times \vec{E} = -\frac{\partial \vec{B}}{\partial t} \tag{2.10}$$

$$\nabla \times \vec{H} = \frac{\partial \vec{D}}{\partial t} + \vec{J} \tag{2.11}$$

We define the spatial coordinates *(i,j,k)* as $(i\Delta x, j\Delta y, k\Delta z)$ with the intervals in the three dimensions to be Δx, Δy, and Δz. And we use the superscript number *n* to represent the time step in the FDTD process. Thus, we could rewrite the *x*-direction components in Eq.(2.10) and Eq.(2.11) in the unit cell defined in Fig 2. 2 as below.

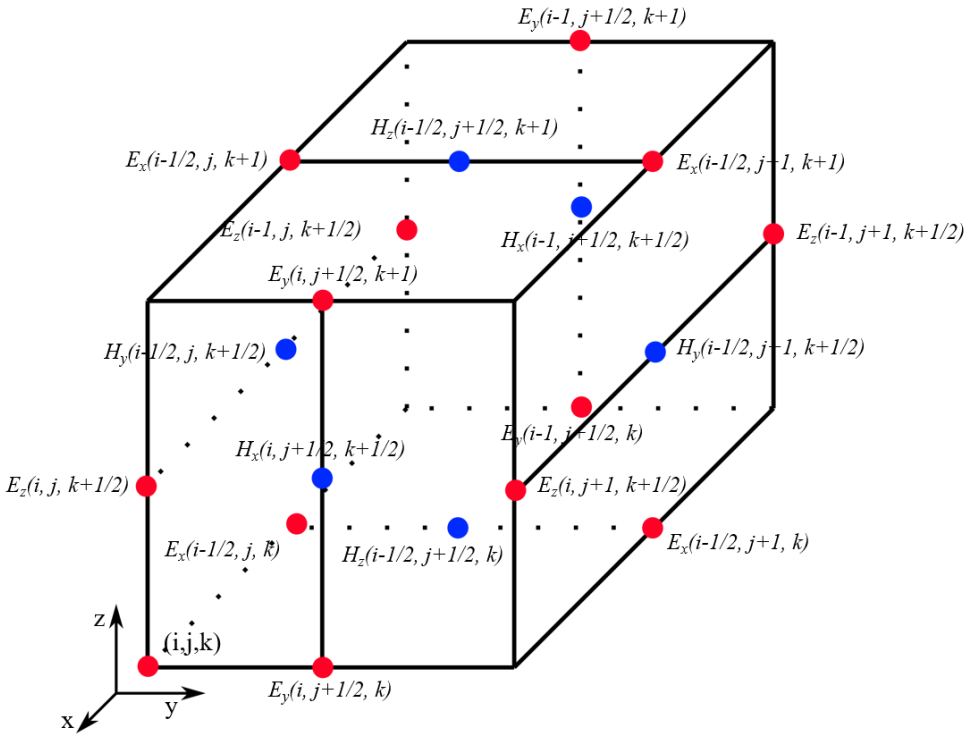

Fig 2. 2 The unit cell in FDTD 3d dimensions with E and H components in the rectangular coordinate system.

$$\frac{B_x^{n+\frac{1}{2}}\left(i,j+\frac{1}{2},k+\frac{1}{2}\right)-B_x^{n-\frac{1}{2}}\left(i,j+\frac{1}{2},k+\frac{1}{2}\right)}{\Delta t}=\frac{E_y^n\left(i,j+\frac{1}{2},k+1\right)-E_y^n\left(i,j+\frac{1}{2},k\right)}{\Delta z}-\frac{E_z^n\left(i,j+1,k+\frac{1}{2}\right)-E_z^n\left(i,j,k+\frac{1}{2}\right)}{\Delta y} \quad (2.12)$$

$$\frac{D_x^n\left(i-\frac{1}{2},j,k\right)-D_x^{n-1}\left(i-\frac{1}{2},j,k\right)}{\Delta t}=\frac{H_z^{n-1/2}\left(i-1/2,j+\frac{1}{2},k\right)-H_z^{n-1/2}\left(i-\frac{1}{2},j-\frac{1}{2},k\right)}{\Delta y}-\frac{H_y^{n-\frac{1}{2}}\left(i-\frac{1}{2},j,k+\frac{1}{2}\right)-H_y^{n-\frac{1}{2}}\left(i-\frac{1}{2},j,k-\frac{1}{2}\right)}{\Delta z}+$$

$$J_x^{n-\frac{1}{2}}(i-\frac{1}{2},j,k) \quad (2.13)$$

Eq.(2.12) and Eq.(2.13) provide the individual component of the electric and magnetic field at the $(i\Delta x, j\Delta y, k\Delta z, n\Delta t)$ space-time grid point based on the previous step in the finite difference analysis. Suppose we ensure that the electromagnetic field does not vary significantly during each space-time step. In that case, we could use such a finite difference method to calculate the

electromagnetic field distribution at the given location at any time starting from the electromagnetic source under boundary conditions such as perfect matching layer (PML).

This powerful technique provides the exact solution to the electromagnetic wave distribution at any space-time grid point. And it could solve complex problems such as irregular structures and anisotropic mediums. However, the accuracy and universality of this algorithm come at a price of extremely long simulation time and significant memory space. And it is also not time-efficient when dealing with resonating structures. Nevertheless, we could perform the FDTD simulation in the commercial software such as Lumerical FDTD®.

Above all, we tend to use analytical calculations to obtain the coarse range for the design parameters in the first step. And we shall use time-efficient sweep simulation engines in either EME or BMP to acquire featured design values. In the end, we could build a precise three-dimensional simulation environment in FDTD to confirm the best choice of the design parameters. Once we are satisfied with the range of design parameters, we shall use the layout environment described in the next chapter to create the lithography mask for the fabrication process.

2.3 Layout Environment

We perform the sweep simulation of Si_3N_4 waveguide platforms utilizing the above simulation methods to obtain the essential platform design parameters shown in Fig 2. 3. Fig 2. 3 presents the simulated optical mode effective index with respect to the core width for four different cases. The "SM" and "MM" marks in Fig 2. 3 represent the choice for single-mode condition and multi-mode condition. It is critical that we choose the optimal single-mode core width to balance the propagation loss and extra mode excitation. The multi-mode width is specifically picked that we have the two lowest-order of the TE modes. Therefore, this multi-mode waveguide could help to

increase the optical power confinement in the waveguide core region. And it will result in the mitigation of the propagation loss in the AWGs discussed in the following chapters.

Table 2 summarizes the critical design parameters of the 150 nm-thick and 200 nm-thick Si_3N_4 waveguide platform used in the lithography mask layout process. We have developed a Python-script-based photonic mask layout environment based on the IPKISS design framework [38], [39]. The open-source IPKISS design framework provides various fundamental geometric elements (i.e., circles, rectangles). Thus, we could establish our photonic design kits (PDKs) by combining different geometric elements with simulated design parameters similar to the EDA process in the electronic IC industry. We build our Python PDK environment in a hierarchical structure. First, we simulate and conclude individual elements such as straight waveguides, edge couplers, directional couplers, MMIs, star-couplers as the library class, with the example shown in Fig 2. 4.(a). Then, we could create a new class in a higher hierarchy that calls and combine the fundamental elements from the library into complex PICs. Because each component in the library class is independent, we could add and update anyone without affecting the existing layouts. In the end, the design environment could generate the corresponding GDSII format mask layout for production shown in Fig 2. 4.(b).

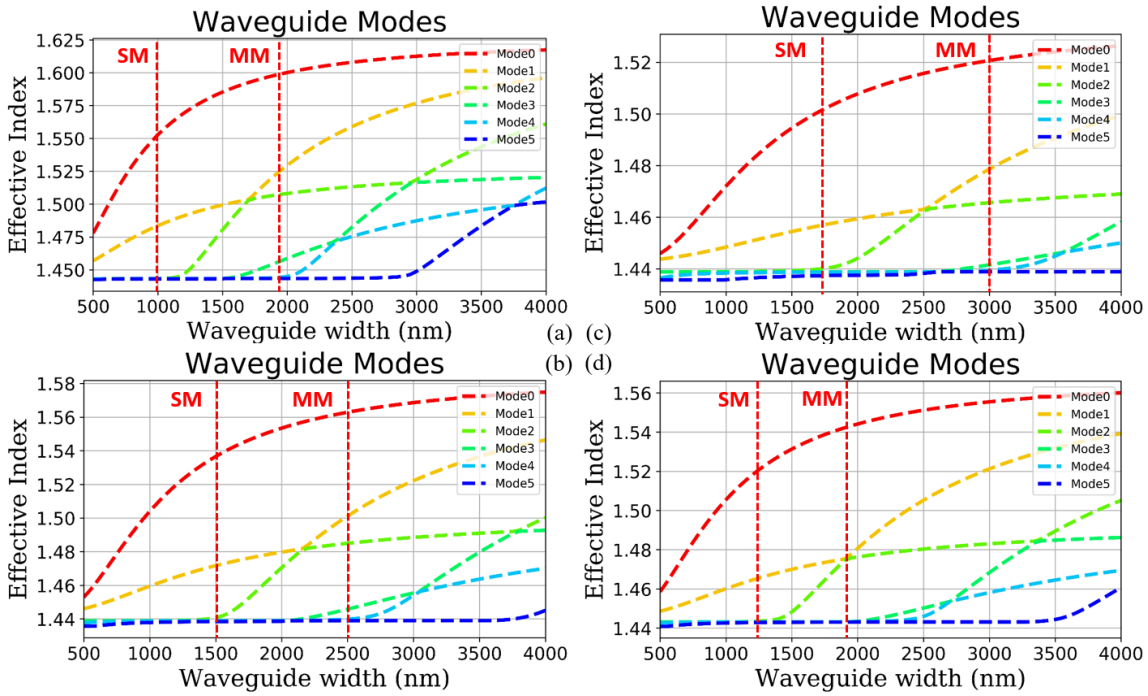

Fig 2. 3 Waveguide simulation results of (a) 200 nm-thick Si_3N_4 platform at 1310 nm wavelength; (b) 200 nm-thick Si_3N_4 platform at 1550 nm wavelength; (c) 150 nm-thick Si_3N_4 platform at 1550 nm wavelength; (d) 150 nm-thick Si_3N_4 platform at 1310 nm wavelength.

Table 2 Critical design parameters of the nitride waveguide platforms

PIC Platform	150 nm Si_3N_4	150 nm Si_3N_4	200 nm Si_3N_4	200 nm Si_3N_4
Center Wavelength (nm)	1550	1310	1550	1310
Single-mode Core width (μm)	1.7	1.2	1.5	1.0
Multi-mode Core width (μm)	3.0	1.9	2.5	1.9
Minimum Bending Radius (μm)	200.0	150.0	100.0	100.0
Slab index	1.530	1.558	1.584	1.624
Single-mode Waveguide index	1.502	1.519	1.536	1.553
Multi-mode Waveguide index	1.521	1.538	1.563	1.598

The most significant advantage of this developed layout environment compared to the traditional GUI alternative is the object-oriented programming and the separation between design parameters and layout details. We could manipulate the design parameters in a distinctive window shown in Fig 2. 4.(a) without any influence on the actual geometric feedback shown in Fig 2. 4.(b). This characteristic also enables us to efficiently combine various elements from the design library free of manual placing and arrangements. Fig 2. 4 demonstrates that we could simultaneously realize a complex component (eight-channel star-coupler at 1310 nm wavelength) with a significant number of design parameters.

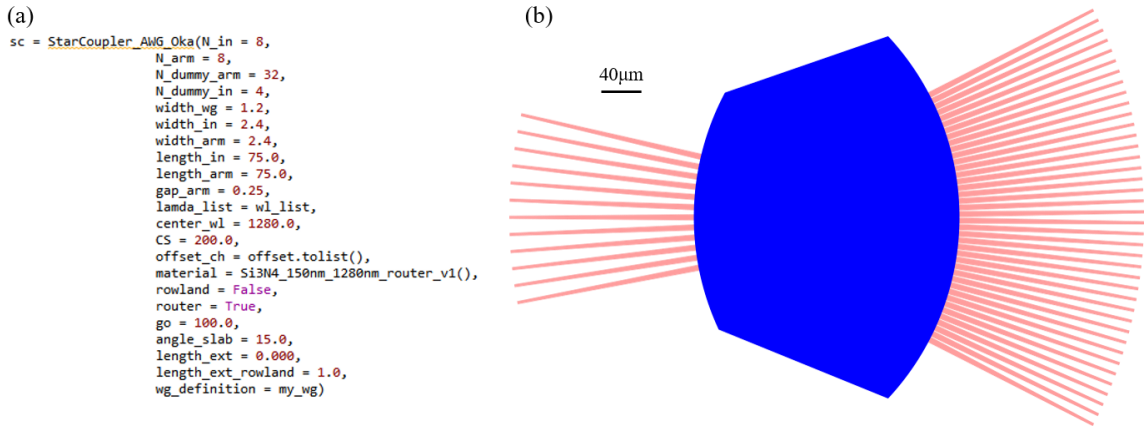

Fig 2. 4 (a) The AWG star-coupler design class in our component PDK; (b) The corresponding star-coupler layout in the GDSII format.

2.4 Low-loss Fabrication Process

After the device simulation and generating lithography mask layouts of specific photonic elements and PICs, we will perform the fabrication process in cleanrooms to realize practical devices. All fabrication processes take place in the Center for Nano-MicroManufacturing in UC Davis and Marvell Nanolab in UC Berkeley. We develop the fabrication process for low-loss Si_3N_4 waveguide platforms shown in Fig 2. 5.

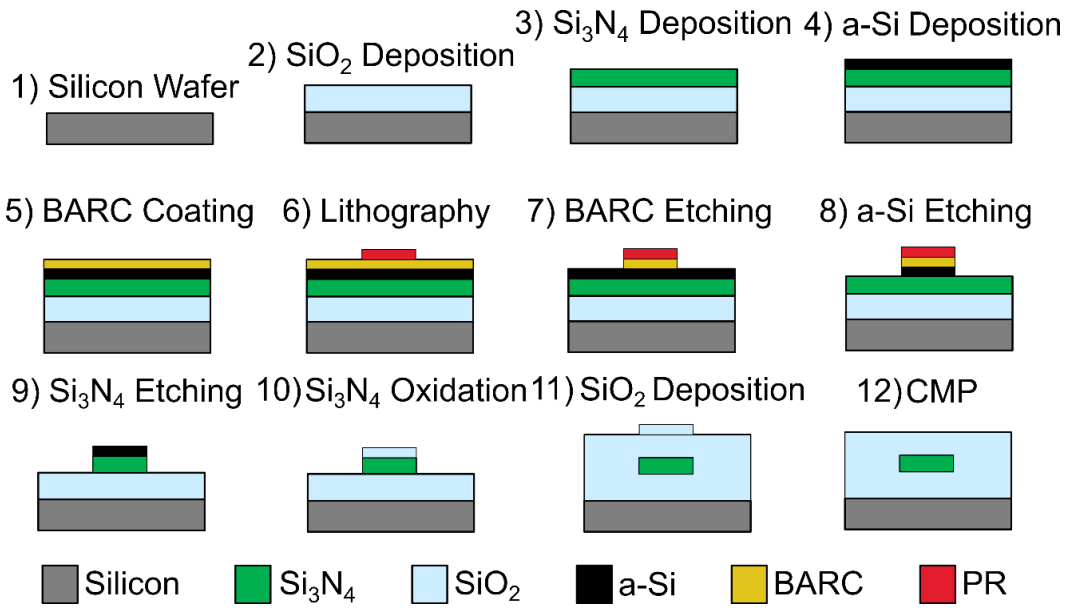

Fig 2. 5 Low-loss Si_3N_4 fabrication process flow.

We start the fabrication process on a six-inch diameter p-type Silicon wafer with wafer cleaning through acetone rinse and hot piranha bath shown as step.1) in Fig 2. 5. First, we perform the low-pressure chemical vapor deposition (LPCVD) to obtain approximately a 5 μm-thick SiO_2 layer as the bottom cladding for all photonic devices shown as step.2). Then, we perform the LPCVD at 800 ℃ for approximately 40 minutes to deposit a 150 nm-thick stoichiometric Si_3N_4 layer shown as step.3) in Fig 2. 5. This Si_3N_4 layer serves as the waveguide core region for entire devices and PICs. Then we deposit approximately 130 nm-thick amorphous Silicon (a-Si) by LPCVD at 550 ℃ in step.4) serving as the hard mask for the nitride core layer during the following etching process. We ensure the wafer goes through the high-temperature annealing step at the end of each LPCVD process to remove the extra dangling *-OH* and *-NH* bonds. In step.5) in Fig 2. 5, we begin the lithography process on the wafer with the spin coating of a 50 nm-thick bottom anti-reflective coating (BARC) layer on the top of the a-Si layer. This BARC layer is critical in the low-loss fabrication process to improve the linearity and roughness control of the deep-UV (DUV)

photoresists. Next, we expose and define the DUV photoresists pattern utilizing the ASML 5500/300 stepper at the 18.5 mJ/cm^2 exposure energy level in step.6). The developed star-coupler output section is shown in Fig 2. 6.(a). The BARC layer covers the dark brown region around the exposed star-coupler.

Fig 2. 6 Microscope photos of the star-coupler on the 1st waveguide layer after (a) step.6) in Fig 2. 5; (b) step.8) in Fig 2. 5; (c) step.9) in Fig 2. 5; (d) step.10) in Fig 2. 5.

We perform the BARC etching process in step.7) using the standard C_4F_8 active gas at approximately 5 nm/s removal rate. The 50 nm-thick BARC layer is completely removed in Fig 2. 6.(b), and the light-yellow a-Si layer is exposed. Fig 2. 7.(a) presents the SEM cross-section photo

of the test structure after the BARC etching process with smooth sidewalls and 85° etching angle. Then, we use the *HBr* gas in step.8) to etch the a-Si hard-mask at 4 nm/s etching rate. Fig 2. 7.(b) shows the SEM cross-section photo of the a-Si hard-mask etching result. We confirm the 130 nm-thick photoresist, 51 nm-thick BARC layer, and 128 nm-thick a-Si sandwich structure with the 64° etching angle generated by the *HBr* gas dry etcher. And there is no extra sidewall roughness caused in this hard-mask dry etching process. Furthermore, we remove the additional photoresist on the top of the wafer with an electronic asher.

The step.9) in Fig 2. 5 is the essential step to achieve low-loss performance on the nitride waveguide platform. We conduct different trials and conclude the combination of dry and wet etching to be the best choice to realize the low-loss performance. We remove approximately a 140 nm-thick Si_3N_4 layer in an inductively coupled plasma (ICP) etching system with a combination of C_4F_8, O_2, and H_2 gas, followed by a quick wet etching in the hot H_3PO_4 acid bath to remove the rest of the nitride layer. We calibrate the etching rate on dummy samples before conducting the etching process on the actual processing wafers: 4 nm/s removal rate for Si_3N_4 in the dry etcher; 2 nm/s removal rate for Si_3N_4 in the 160 ℃ H_3PO_4 acid bath. In the end, we perform each etching approach with appropriate selectivity towards the a-Si hard mask. Finally, we over-etch the Si_3N_4 layer approximately 20 nm into the SiO_2 bottom substrate to ensure the complete removal of the nitride core layer. Fig 2. 6.(c) presents the microscope image of the star-coupler output region after this etching process. A thin a-Si hard mask covers the star-coupler, and the nitride layer is completely removed at the rest of the area. Fig 2. 7.(d) provides the cross-section SEM photo of the waveguide core region after the etching process with 49 nm-thick a-Si layer on the top of the 150 nm-thick nitride waveguide core. The a-Si hard-mask layer and the combination of the dry and wet etching process deliver the excellent sidewall quality shown in the photo.

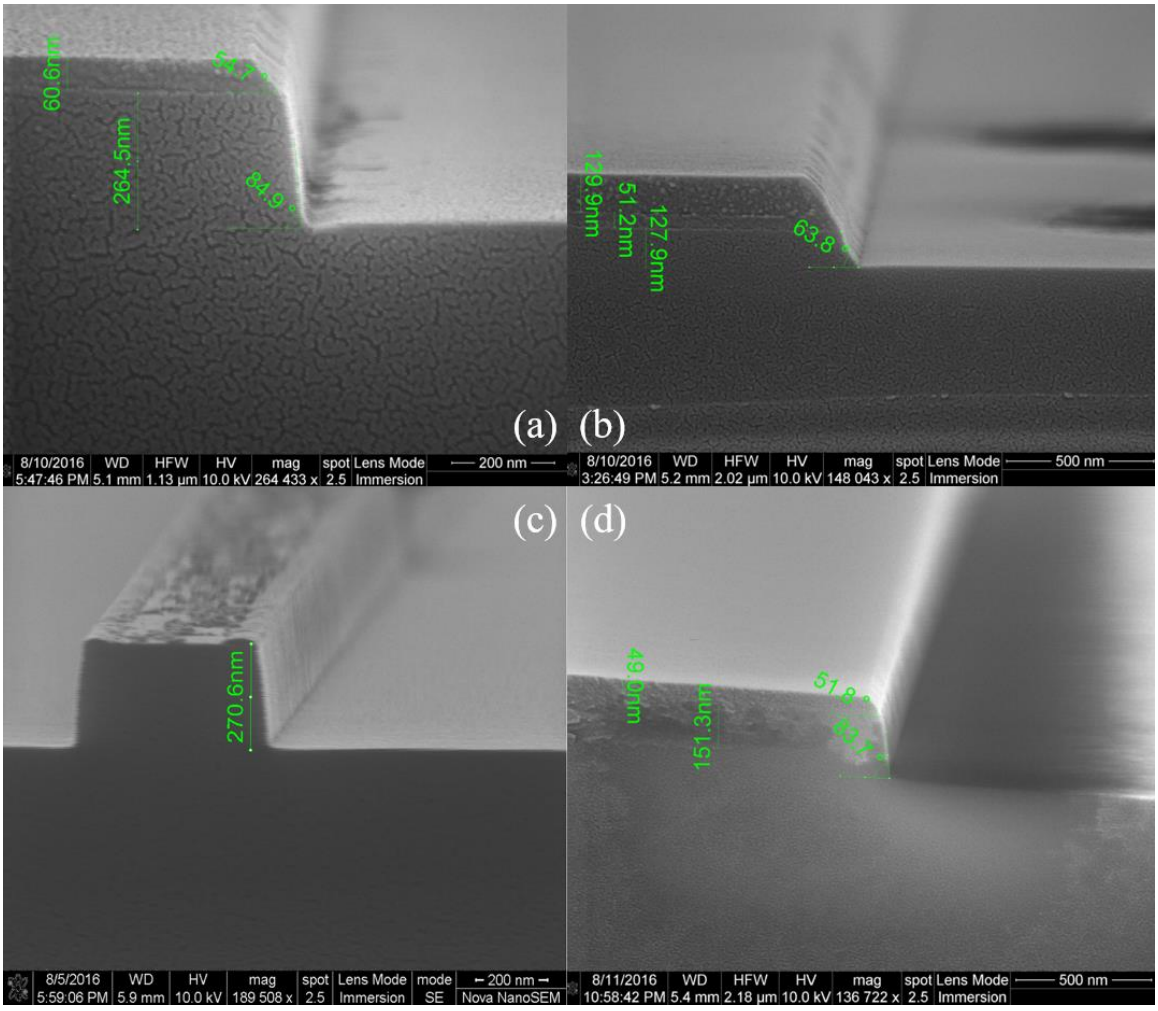

Fig 2. 7 SEM photos of the 1st layer waveguide cross-section after (a) step.7) in Fig 2. 5; (b) step.8) in Fig 2. 5; (c) the photoresist removal process after step.8) in Fig 2. 5; (d) step.9) in Fig 2. 5.

We perform the wet oxidation at 1150 ℃ after the core Si_3N_4 etching process to remove the extra a-Si hard-mask layer at the top of the wafer in step.10). Fig 2. 6.(d) shows a top-down view photo of the star-coupler region after the wet oxidation process, confirming the complete removal of all a-Si hard-mask. We could maintain this wet-oxidized SiO_2 layer since we will continue to use the LPCVD to deposit a 4 µm-thick SiO_2 layer as the waveguide over-cladding in step.11). In the end, we perform a 6-hour high-temperature (>1150C) annealing process on the wafer to remove all *O*-

H and *N-H* bonds in the deposited material. Step.12) in Fig 2. 5 shows the chemical mechanical polishing (CMP) technique to remove the SiO_2 bumps and realize the sub-nanometer roughness surface for the heterogeneous integration in the vertical direction. We could choose between the dicing and the deep etching process to shape the chip facets at the optical precision.

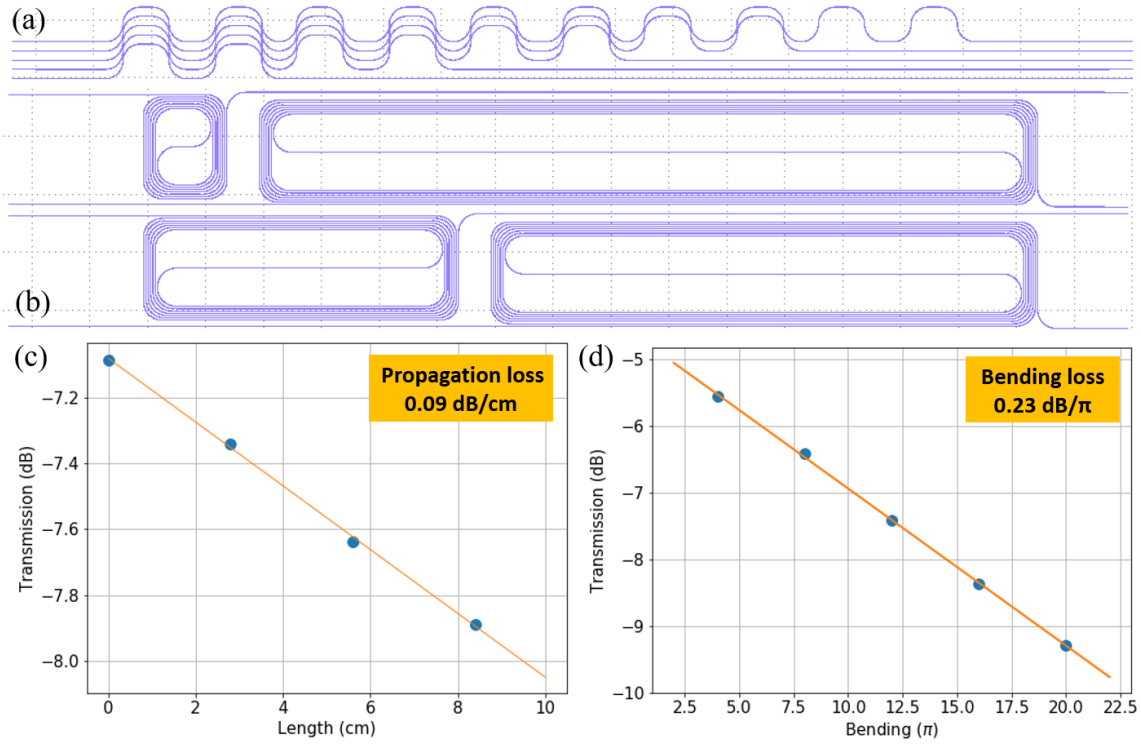

Fig 2. 8 (a) Photonic mask layout of testing structures for the waveguide bending loss; (b) Photonic mask layout of testing structures for the waveguide propagation loss; (c) The measurement result of the propagation loss of 150 nm-thick Si_3N_4 waveguides; (d) The measurement result of the bending loss of 150 nm-thick Si_3N_4 waveguides.

We conduct the device characterization utilizing the in-house optical vector network analyzer (OVNA) setup to retrieve the transmission matrix of the device-under-test (DUT) in the 1500 nm to 1600 nm wavelength range on testing structures shown in Fig 2. 8.(a) and Fig 2. 8.(b). Fig 2. 8.(a) presents the mask layout of the testing structures for the waveguide bending loss. We could perform the linear fitting on the insertion loss data of entire pass-through waveguides to retrieve

the slope value defined as the 180° bending loss. Fig 2. 8.(d) includes the insertion loss of all five pass-through waveguides with the linear fitting of a 0.23 dB/180° bending loss. Fig 2. 8.(b) illustrates four spiral waveguides with different lengths in the mask layout for the cut-back method to characterize the propagation loss. The a-Si hard-mask-assisted lithography process and the combination of the dry and wet etching approach help improve the propagation loss to the value of 0.09 dB/cm for the 150 nm-thick Si_3N_4 waveguides.

We design and layout a gyro structure shown in Fig 2. 9.(a) with a total length of 8.5 m in a single layer to further test the propagation loss on the nitride platform achieved by our low-loss fabrication process. We fabricate and deliver the gyro structure on the 50 nm-thick Si_3N_4 waveguide platforms with the image shown in Fig 2. 9.(b). The back-reflection measurement in the OVNA system confirms the dB/m level propagation loss from our low-loss fabrication process.

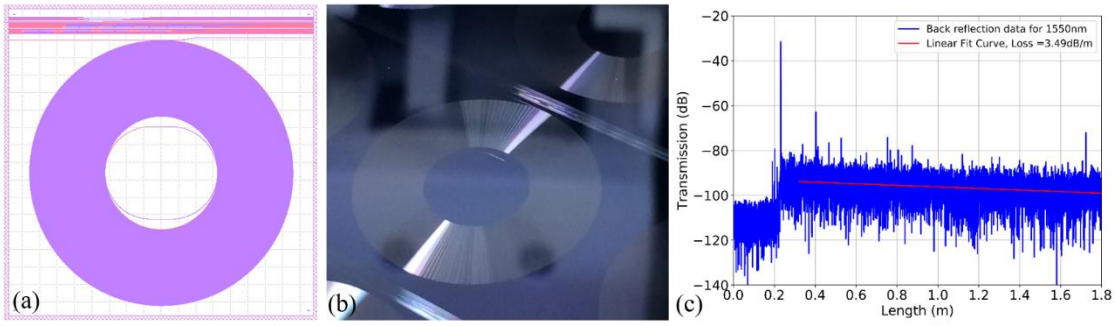

Fig 2. 9 (a) Photonic mask layout of gyro structure with a total length of 8.5 meters; (b) The image of the fabricated gyro based on the 50 nm-thick Si_3N_4 waveguide platform; (c) The back-reflection measurement result of the propagation loss.

References

[1] R. Diehl, *High-power diode lasers: fundamentals, technology, applications*, vol. 78. Springer Science \& Business Media, 2000.

[2] L. A. Coldren, S. W. Corzine, and M. L. Mashanovitch, *Diode lasers and photonic integrated circuits*, vol. 218. John Wiley \& Sons, 2012.

[3] G. Keiser, *Optical fiber communications*, vol. 2. McGraw-Hill New York, 2000.

[4] K. Kikuchi, "Fundamentals of coherent optical fiber communications," *J. Light. Technol.*, vol. 34, no. 1, pp. 157–179, 2015.

[5] T. Okoshi, *Optical fibers*. Elsevier, 2012.

[6] A. W. Snyder, "Understanding monomode optical fibers," *Proc. IEEE*, vol. 69, no. 1, pp. 6–13, 1981.

[7] M. Smit, K. Williams, and J. van der Tol, "Past, present, and future of InP-based photonic integration," *APL Photonics*, vol. 4, no. 5, p. 50901, 2019.

[8] L. M. Augustin *et al.*, "InP-based generic foundry platform for photonic integrated circuits," *IEEE J. Sel. Top. quantum Electron.*, vol. 24, no. 1, pp. 1–10, 2017.

[9] M. Smit *et al.*, "An introduction to InP-based generic integration technology," *Semicond. Sci. Technol.*, vol. 29, no. 8, p. 83001, 2014.

[10] C. R. Doerr and K. Okamoto, "Advances in silica planar lightwave circuits," *J. Light. Technol.*, vol. 24, no. 12, pp. 4763–4789, 2006.

[11] A. Himeno, K. Kato, and T. Miya, "Silica-based planar lightwave circuits," *IEEE J. Sel. Top. quantum Electron.*, vol. 4, no. 6, pp. 913–924, 1998.

[12] A. Kaneko, T. Goh, H. Yamada, T. Tanaka, and L. Ogawa, "Design and applications of silica-based planar lightwave circuits," *IEEE J. Sel. Top. quantum Electron.*, vol. 5, no. 5, pp. 1227–1236, 1999.

[13] T. Miya, "Silica-based planar lightwave circuits: passive and thermally active devices," *IEEE J. Sel. Top. quantum Electron.*, vol. 6, no. 1, pp. 38–45, 2000.

[14] R. Soref and B. Bennett, "Electrooptical effects in silicon," *IEEE J. Quantum Electron.*, vol. 23, no. 1, pp. 123–129, 1987.

[15] N. H. E. Weste and K. Eshraghian, "Principles of CMOS VLSI design: a systems perspective," *NASA STI/Recon Tech. Rep. A*, vol. 85, p. 47028, 1985.

[16] Y. Taur and T. H. Ning, *Fundamentals of modern VLSI devices*. Cambridge university press, 2013.

[17] C. R. Doerr, "Silicon photonic integration in telecommunications," *Front. Phys.*, vol. 3, p. 37, 2015.

[18] P. Dong, Y.-K. Chen, G.-H. Duan, and D. T. Neilson, "Silicon photonic devices and integrated circuits," *Nanophotonics*, vol. 3, no. 4–5, pp. 215–228, 2014.

[19] R. Soref, "The past, present, and future of silicon photonics," *IEEE J. Sel. Top. quantum Electron.*, vol. 12, no. 6, pp. 1678–1687, 2006.

[20] K. Shang, S. Pathak, B. Guan, G. Liu, and S. J. B. Yoo, "Low-loss compact multilayer silicon nitride platform for 3D photonic integrated circuits," *Opt. Express*, vol. 23, no. 16, pp. 21334–21342, 2015.

[21] D. J. Moss, R. Morandotti, A. L. Gaeta, and M. Lipson, "New CMOS-compatible platforms based on silicon nitride and Hydex for nonlinear optics," *Nat. Photonics*, vol. 7, no. 8, pp. 597–607, 2013.

[22] D. Zhu *et al.*, “Integrated photonics on thin-film lithium niobate,” *Adv. Opt. Photonics*, vol. 13, no. 2, pp. 242–352, 2021.

[23] M. Rezem, A. Günther, B. Roth, E. Reithmeier, and M. Rahlves, “Low-cost fabrication of all-polymer components for integrated photonics,” *J. Light. Technol.*, vol. 35, no. 2, pp. 299–308, 2017.

[24] H. Zuo, S. Yu, T. Gu, and J. Hu, “Low loss, flexible single-mode polymer photonics,” *Opt. Express*, vol. 27, no. 8, pp. 11152–11159, 2019.

[25] M. Smit *et al.*, “Generic foundry model for InP-based photonics,” *IET Optoelectron.*, vol. 5, no. 5, pp. 187–194, 2011.

[26] A. W. Fang, H. Park, O. Cohen, R. Jones, M. J. Paniccia, and J. E. Bowers, “Electrically pumped hybrid AlGaInAs-silicon evanescent laser,” *Opt. Express*, vol. 14, no. 20, pp. 9203–9210, 2006.

[27] D. Liang and J. E. Bowers, “Recent Progress in Heterogeneous III-V-on-Silicon Photonic Integration,” *Light Adv. Manuf.*, vol. 2, no. 1, pp. 1–25, 2021.

[28] P. Rabiei, J. Ma, S. Khan, J. Chiles, and S. Fathpour, “Heterogeneous lithium niobate photonics on silicon substrates,” *Opt. Express*, vol. 21, no. 21, pp. 25573–25581, 2013.

[29] Y. Qi and Y. Li, “Integrated lithium niobate photonics,” *Nanophotonics*, vol. 9, no. 6, pp. 1287–1320, 2020.

[30] D. F. G. Gallagher and T. P. Felici, “Eigenmode expansion methods for simulation of optical propagation in photonics: pros and cons,” in *Integrated optics: devices, materials, and technologies VII*, 2003, vol. 4987, pp. 69–82.

[31] P. Bienstman and R. Baets, “Optical modelling of photonic crystals and VCSELs using eigenmode expansion and perfectly matched layers,” *Opt. Quantum Electron.*, vol. 33, no. 4, pp. 327–341, 2001.

[32] J. Van Roey, J. der Donk, and P. E. Lagasse, “Beam-propagation method: analysis and assessment,” *Josa*, vol. 71, no. 7, pp. 803–810, 1981.

[33] W. P. Huang and C. L. Xu, “Simulation of three-dimensional optical waveguides by a full-vector beam propagation method,” *IEEE J. Quantum Electron.*, vol. 29, no. 10, pp. 2639–2649, 1993.

[34] G. Mur, “Absorbing boundary conditions for the finite-difference approximation of the time-domain electromagnetic-field equations,” *IEEE Trans. Electromagn. Compat.*, no. 4, pp. 377–382, 1981.

[35] K. Yee, “Numerical solution of initial boundary value problems involving Maxwell’s equations in isotropic media,” *IEEE Trans. Antennas Propag.*, vol. 14, no. 3, pp. 302–307, 1966.

[36] C. R. Doerr, “Sparse finite difference time domain method,” *IEEE Photonics Technol. Lett.*, vol. 25, no. 23, pp. 2259–2262, 2013.

[37] C. Doerr, “3D sparse finite-difference time-domain simulation of silicon photonic integrated circuits,” in *Optical Fiber Communication Conference*, 2015, pp. W4A--6.

[38] W. Bogaerts, M. Fiers, M. Sivilotti, and P. Dumon, “The IPKISS photonic design framework,” in *Optical Fiber Communication Conference*, 2016, pp. W1E--1.

[39] W. Bogaerts, P. Dumon, E. Lambert, M. Fiers, S. Pathak, and A. Ribeiro, “Ipkiss: A parametric design and simulation framework for silicon photonics,” in *The 9th International Conference on Group IV Photonics (GFP)*, 2012, pp. 30–32.

Chapter 3 Arrayed Waveguide Gratings

Wavelength division multiplexing (WDM) technology [1] has revolutionized the data communication and transmission infrastructure surpassing the traditional electrical cable system with the capability of supplying multiple optical signals with different wavelengths simultaneously in one fiber. Passive optical filtering devices such as multiplexers (Mux) and demultiplexers (Demux) [2] play principal roles in the WDM systems to gather and distribute the abundant wavelength channels at different communication nodes. Arrayed waveguide gratings (AWGs) stand out of the alternatives (e.g., cascaded Mach-Zehnder Interferometer lattice filters and Echelle gratings) within the finite impulse response (FIR) Mux and Demux category, possessing the superior performance on the device crosstalk level, insertion loss, and device footprint [3]. The AWGs are developed and improved by Smit [4], Dragone [5], Takahashi [6], and Okamoto [7] in the early 1990s and have been realized on various material platforms (InP [8], Silica [9], silicon-on-insulator (SOI) [10], [11], Ge [12]) for applications not only in optical communication [13] but also in sensing [14] and signal processing [15]. AWGs could also be designed into a cyclic spectrum pattern [16], [17] enabling the low-cost and low-power optical interconnect functionalities for high-performance computing (HPC) [18]. Device footprint, insertion loss, inter-channel crosstalk, intra-channel crosstalk [19] are the most critical device parameters for AWGs in the photonic integrated circuits (PICs). The ultra-low-loss Si_3N_4 waveguide platform discussed in the previous chapter provides low-loss and small-footprint passive AWGs with the convenience of heterogeneous integration to III-V and SOI platforms.

This chapter details the operational theory of AWGs, explains the modelling and simulation methodology of AWGs, and experimentally demonstrates Si_3N_4 AWGs in the telecommunication O and C band.

3.1 Theory

An AWG consists of two star-couplers (free propagation regions (FPR)) and arrayed arms of waveguides with linearly adjacent path-length increase (ΔL as the path-length difference between the (j-1)-th path (red) and j-th path (blue), L_c represents the minimum path length in the arrayed arms of waveguides), shown in Fig 3. 1. The AWG system could be analogized to an imaging system with two lenses and a prism working on a specific wavelength range [20]. Two star-couplers are functioning like lenses that diffract and focus the light rays. The arrayed arms of waveguides are operating as a prism that refracts light with wavelength dispersion. The input star coupler (Star-Coupler 1) receives the waveguide light modes from the input apertures (locate at different x_i values), propagates them in its slab region with the radius of f_i, and generates diffracted mode at the interface between the input star coupler and the arrayed arms of waveguides (d_i denotes the pitch between adjacent arrayed waveguides). The phase fronts of light modes with two different wavelengths are shown in green (λ_1, shorter wavelength) and yellow (λ_2, longer wavelength) dashed lines in Fig 3. 1. These phase fronts are ideally circular resulting from the Fraunhofer diffraction [7] in the FPR. Due to the chromatic dispersion inside the arrayed waveguides, the phase fronts (green and yellow) from different wavelengths of light will obtain different phase delays. These light modes with differently tilted phase fronts will refocus at different output waveguides (locate at different x_o values) after the free propagation in the output star coupler (Star-Coupler 2) with the radius of f_o. The arrayed waveguides pitch in the output start coupler is denoted as d_o. Usually, we will set the geometric parameters in the input and output star couplers to be the

same ($d_i = d_o, f_i = f_o$). Star couplers could be designed to use confocal mounting or Rowland circle mounting [21]. The latter could help to mitigate the second-order and the third-order imaging aberrations.

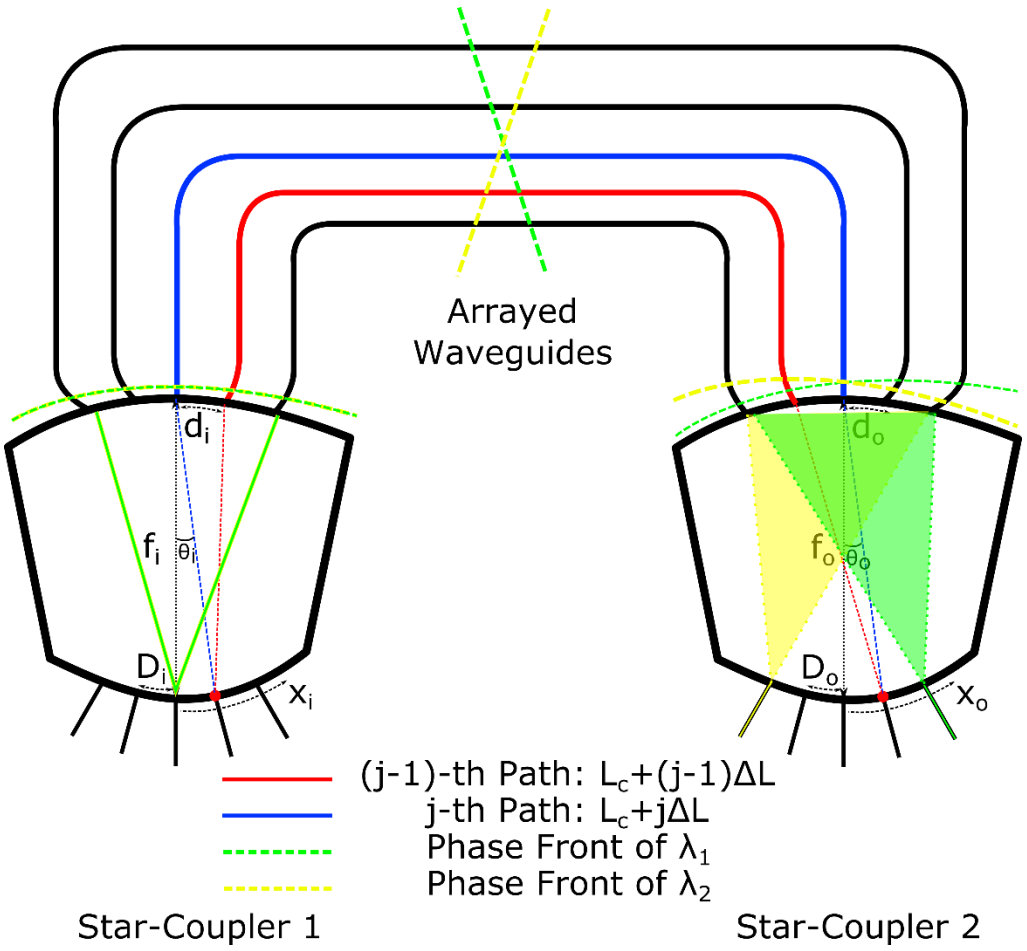

Fig 3. 1 Detailed AWG design diagram consists of two star-couplers (input and output) and arrayed arms of waveguides. Two optical paths (blue and red) refer to the adjacent optical paths for the center wavelength light travelling from input port to output port under the constructive interference condition.

We define the geometric, systematic, and material parameters for the design of AWGs (shown in Fig 3. 1) as the following (shown in Table 3): (1) Geometric parameters: input and output star coupler radius (f_i and f_o); arrayed waveguides pitch at the input and output star coupler (d_i and d_o). The arrayed waveguides pitch is the sum of the arrayed waveguide aperture and waveguide gap,

which is usually kept at the minimum resolution in the lithography process to minimize the footprint and reduce the insertion loss; input and output waveguides spatial spacing (D_i and D_o); input and output waveguide spatial locations (x_i and x_o); input and output waveguide angular locations (θ_i and θ_o); path length difference between adjacent arrayed waveguides (ΔL). The output waveguide spatial and angular locations should follow the Eq.(3.1) relationship for small diffraction angles:

$$\theta \approx \frac{x}{f} \tag{3.1}$$

We usually balance the geometric parameters to achieve a better trade-off between the small footprint and the low-loss performance. (2) Systematic parameters: the number of channels at input and output star couplers (N_{ch}); the number of arrayed arms (N_{arms}). Empirically, N_{arms} is designed within 2.5 to 4 times the number of wavelength channels to avoid unnecessary insertion loss and phase error; center wavelength/frequency (λ_0/υ_0); wavelength channel spacing (CS). (3) Material parameters: the field divergence angle inside the free propagation region (φ); the star coupler slab region effective index with respect to the wavelength ($n_{slab}(\lambda, \upsilon)$); arrayed arms of waveguides effective index with respect to the wavelength ($n_{wg}(\lambda, \upsilon)$); arrayed arms of waveguides group index with respect to the wavelength ($n_g(\lambda, \upsilon)$). We acquire systematic parameters, usually governed by specific system-level requirements; 1) What is the operating wavelength (*O*- or *C*-band)? 2) Is it $1 \times N$ demux or $N \times N$ router? 3) What is the channel spacing (DWDM or CWDM)? These application aspects of questions are the first step in the design procedure. Based on the chosen PIC platform (SOI, Si_3N_4, III-V, or silica), we could use simulation methods described in the previous chapter to obtain material parameters as the second step of the design procedure. We

then need to design and calculate geometric parameters following the constructive interference condition described below as the last step in designing AWGs.

Table 3 Design parameters for AWGs

Parameters	Definitions
f_i and f_o	Input and output star-coupler radius
d_i and d_o	Arrayed waveguides pitch at input and output star couplers
D_i and D_o	Input and output waveguides spatial spacing
x_i and x_o	Input and output waveguide spatial locations
θ_i and θ_o	Input and output waveguide angular locations
ΔL	Path length difference
N_{ch}	Number of wavelength channels
N_{arms}	Number of arrayed arms of waveguides
λ_0/υ_0	Center wavelength / frequency
CS	Channel spacing
φ	Star coupler divergence angle
$n_{slab}(\lambda, \upsilon)$	Star coupler slab effective index
$n_{wg}(\lambda, \upsilon)$	Arrayed waveguides effective index
$n_g(\lambda, \upsilon)$	Arrayed waveguides group index

The constructive interference condition of the refocusing light shown in Fig 3. 1 requires that the path-length difference between the No.(j-1)-th arrayed arm and No.j-th arrayed arm for the light mode inputting at x_i location of the input star coupler (Star-Coupler 1) and outputting at x_o location of the output star coupler (Star-Coupler 2) should equal to an integer multiple of the light mode wavelength. Thus, this interference condition could be expressed as:

$$\beta_{slab}(\lambda)\left(f_i - \frac{d_i x_i}{2f_i}\right) + \beta_{wg}(\lambda)(L_c + (j-1)\Delta L) + \beta_{slab}(\lambda)\left(f_o + \frac{d_o x_o}{2f_o}\right) = \beta_{slab}(\lambda)\left(f_i + \frac{d_i x_i}{2f_i}\right) + \beta_{wg}(\lambda)(L_c + j\Delta L) + \beta_{slab}(\lambda)\left(f_o - \frac{d_o x_o}{2f_o}\right) - 2m\pi \quad (3.2)$$

where m denotes the grating diffraction order, L_c denotes the minimum length in the array waveguide arms and β_{slab}, β_{wg} represents the propagation constant in the star coupler slab region

and the arrayed waveguides region, which could be simulated from the EME or BPM method mentioned in chapter 2. Subtracting the common terms in Eq.(3.2), we have:

$$\beta_{slab}(\lambda)\left(\frac{d_i x_i}{f_i}\right) + \beta_{wg}(\lambda)(\Delta L) - \beta_{slab}(\lambda)\left(\frac{d_o x_o}{f_o}\right) = 2m\pi \tag{3.3}$$

Since the light with the center wavelength λ_0 from the center input at the input star coupler should focus at the center output at the output star coupler, assuming x_i = 0 and x_0 = 0 in this center wavelength case, we can derive from Eq.(3.3):

$$\beta_{wg}(\lambda_0)(\Delta L) = 2m\pi \tag{3.4}$$

$$\lambda_0 = \frac{n_{wg}(\lambda_0)\Delta L}{m} \tag{3.5}$$

We could use Eq.(3.4) to define the grating diffraction order *m* by taking the round to get an integer number $\hat{m}$ to maintain the constructive interference condition:

$$\hat{m} = round(\frac{n_{wg}(\lambda_0)\Delta L}{\lambda_0}) \tag{3.6}$$

To simplify the design and minimize the loss from fabrication variation, we usually design the input star coupler and the output star coupler with the same size: $f_i = f_o = f$ and $d_i = d_o = d$, leave the input/output waveguide locations and the star coupler radius to be design parameters.

According to Eq. (3.4) and Eq.(3.6), the $\hat{m}$-th order of light and the ($\hat{m}$+1)-th order of light coming from the center input of the input star coupler will refocus at the exact center output location of the output star coupler, which could be written as:

$$\beta_{wg}(\lambda_{m'})(\Delta L) = 2\hat{m}\pi \tag{3.7}$$

$$\beta_{wg}(\lambda_{m'+1})(\Delta L) = 2(\hat{m}+1)\pi \tag{3.8}$$

Combining Eq.(3.7) and Eq.(3.8), we should get:

$$\frac{n_{wg}(\lambda_{\widehat{m}+1})}{\lambda_{\widehat{m}+1}} - \frac{n_{wg}(\lambda_{\widehat{m}})}{\lambda_{\widehat{m}}} = 1 \tag{3.9}$$

Since we are considering the AWG functioning around the center wavelength λ_0, the center wavelength is the $\widehat{m}$-th order wavelength: $\lambda_{\widehat{m}} = \lambda_0$. Thus the ($\widehat{m}$+1)-th order of light should have the wavelength one free spectral range away: $\lambda_{\widehat{m}+1} = \lambda_0 - \lambda_{FSR}$, where λ_{FSR} is the free spectral range (FSR) in the wavelength domain. λ_{FSR} and the free spectral range in the frequency domain (υ_{FSR}) follow Eq.(3.10)

$$\frac{\lambda_{FSR}}{\lambda_0} = \frac{\upsilon_{FSR}}{\upsilon_0} \tag{3.10}$$

After defining and using the group index in the arrayed arms of waveguides region defined as Eq.(3.11), we could simplify and deduce the free spectral range of the AWG in Eq.(3.12) and Eq.(3.13):

$$n_g(\lambda) = n_{eff}(\lambda) - \lambda \frac{dn_{eff}(\lambda)}{d\lambda} \tag{3.11}$$

$$\lambda_{FSR} = \frac{n_{eff}(\lambda_0) \times \lambda_0}{n_g(\lambda_0) \times \widehat{m}} \tag{3.12}$$

$$\upsilon_{FSR} = \frac{n_{eff}(\lambda_0) \times \upsilon_0}{n_g(\lambda_0) \times \widehat{m}} \tag{3.13}$$

Combining Eq.(3.5), Eq.(3.10), and Eq.(2.13) we obtain:

$$\Delta L = \frac{c}{n_g(\lambda_0) \times \upsilon_{FSR}} = \frac{{\lambda_0}^2}{n_g(\lambda_0) \times \lambda_{FSR}} \tag{3.14}$$

From Eq.(3.14), we could conclude that the size of AWGs (governed by the ΔL) is inversely proportional to the FSR of the device. Since the FSR of the AWG is directly related to the channel

spacing, the smaller the channel spacing, the larger the size of the AWG. Thus, on the one hand, we could minimize the AWG footprint by increasing the device FSR. But on the other hand, we will face geometric layout obstacles when the ΔL value is too small. Thus, the AWG FSR and device footprint is an actual design trade-off to be considered in the practical layout process.

We could calculate the angular dispersion (Eq.(3.16)) of the light with respect to the wavelength in the output waveguides from Eq.(3.1) and Eq.(3.5) when the light inputs at the center of the input star coupler (Star-Coupler 1), using the spatial dispersion and angular dispersion relationship in Eq.(3.15):

$$\frac{ds}{dv} = f\frac{d\theta}{dv} \tag{3.15}$$

$$sin(\theta_0) = \hat{m}\frac{\lambda_0 n_{eff}(\lambda) - \lambda n_{eff}(\lambda_0)}{n_{eff}(\lambda_0) \times n_{slab}(\lambda) \times d} \tag{3.16}$$

From Eq.(3.16), we could see that the dispersion angle $\theta_o = 0$ when the wavelength is set to be the center wavelength λ_0. Therefore, the light with the shorter wavelength ($\lambda_1 < \lambda_0$ in Fig 3. 1) will have a positive dispersion angle (θ_o) represented by the green color and will have a negative dispersion angle (θ_o) represented by the yellow color the with longer wavelength ($\lambda_2 > \lambda_0$ in Fig 3. 1). This equation relies on the accuracy of the waveguide effective index profile and the star coupler slab effective index profile. These index profiles should be simulated and verified following the simulation methodology described in the previous chapter.

Another critical parameter for the AWG design is the radius of the star coupler. We usually simulate the beam diffraction angle φ using the analytical method or numerical method (commercial software), and the radius is calculated as:

$$f = \frac{N_{arms} d}{\varphi} \tag{3.17}$$

The spectrum response of the AWG is illustrated in Fig 3. 2 with characterization parameters listed as: (1) wavelength FSR (λ_{FSR}); (2) insertion loss represents the transmission loss of the functioning wavelength channel with the highest transmission power; (3) insertion loss non-uniformity defines the insertion loss roll-off between the highest and lowest transmitting channels; (4) inter-channel crosstalk represents the crosstalk value between the adjacent wavelength channels; (5) intra-channel crosstalk defines the crosstalk value from the accumulation of the phase error within the same wavelength channel; (6) 1dB, 3dB, and 10dB bandwidth. The ratio between the 1dB and 10dB bandwidth is further defined as the aspect ratio, which demonstrates the wavelength channel filtering sharpness.

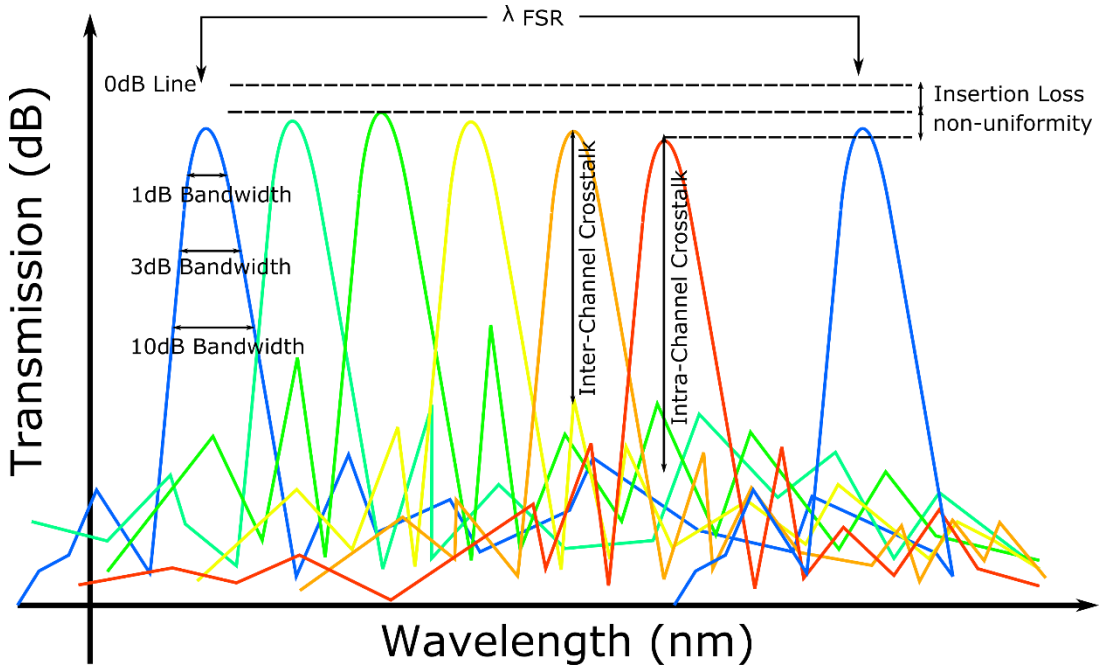

Fig 3. 2 Transmission spectrum diagram of an AWG device with listed parameters: wavelength FSR, insertion loss, loss non-uniformity, inter-channel crosstalk, intra-channel crosstalk, 1dB bandwidth, 3dB bandwidth, and 10dB bandwidth.

3.2 Modelling and Simulations

An AWG consists of 1) two star-couplers; and 2) arrayed arms of waveguides, with the size of over $1mm^2$ on traditional photonics platforms (SOI, III-V). The Eigenmode expansion (EME), the

Beam propagation method (BPM), and the Finite Difference in Time Domain (FDTD) methods described in the previous chapter could only provide time-efficient simulations for optical devices with the maximum size far below 1 mm. Thus, as the complexity of the AWG increases, people have made efforts to investigate alternative semi-analytical modelling methods on circuit level for faster and more accurate AWG simulations. Dragone [5] provided the fundamental analysis based on the Fourier optics for an efficient design and modelling methodology for $N \times N$ star coupler. Smit [22] and others [23], [24] continued to develop the circuit-level simulator based on the Gaussian approximation of the fundamental mode and the paraxial approximation of the free propagation region. Commercial softwares (such as Rsoft [25], and IPKISS.flow [26]) have also been developed utilizing the transmission matrix method and the approximation of the free propagation region. I will introduce the concise in-house Gaussian AWG design/modelling model based on the Fourier Transform algorithm in the following session, which offers the spectrum modelling capability with the fast simulation time.

3.2.1 AWGs Modelling and Simulation Theory

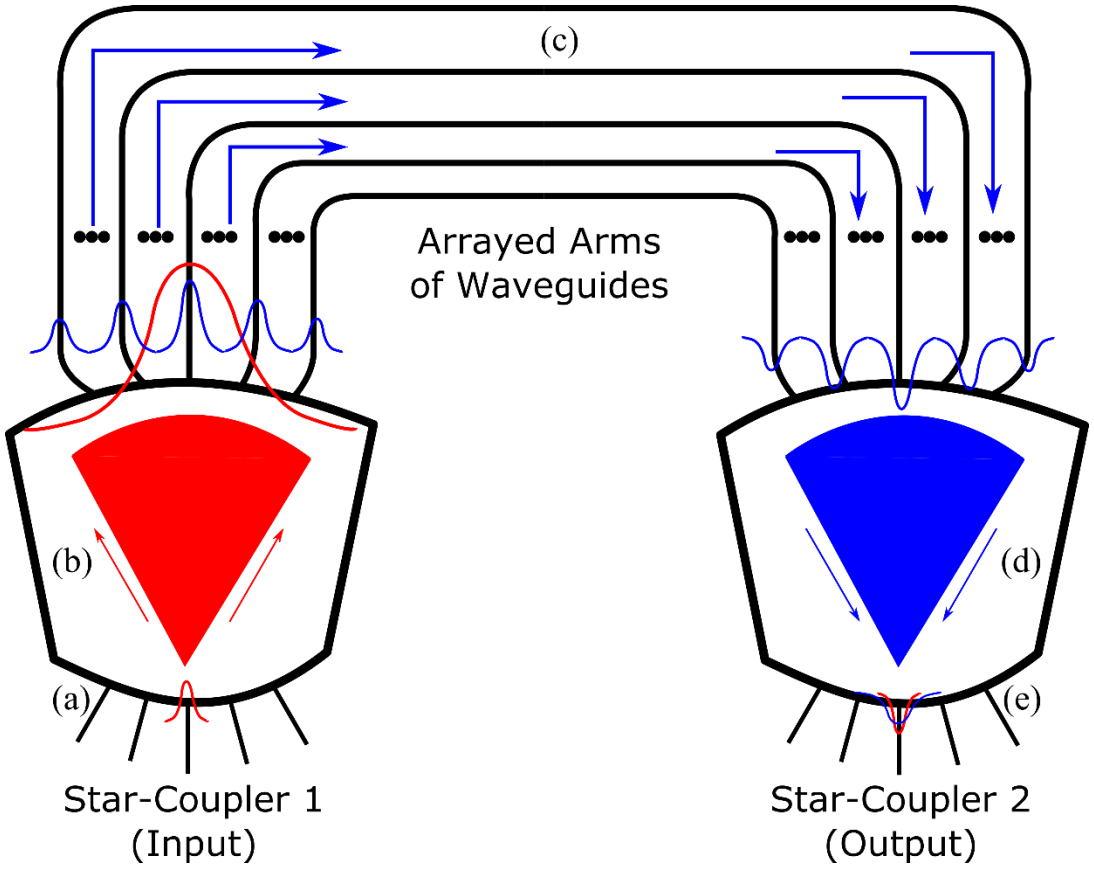

Fig 3. 3 Gaussian AWG analytical modelling diagram with steps (a) the fundamental mode at the input aperture; (b) free propagation of the mode in the input star-coupler; (c) the mode coupling into the arrayed arms of waveguides and the propagation of the mode in the arrayed waveguides; (d) free propagation of the mode in the output star-coupler; (e) mode coupling into the output waveguide.

Fig 3. 3 illustrates the step-by-step AWG analytical modelling methodology based on the approximation of the fundamental Gaussian mode and the Fourier spatial propagation in the star-coupler region within the Fraunhofer diffraction regime. Light is diffracted and re-focused in star-couplers in the Fraunhofer diffraction regime and the phase-front shift is added corresponding to the specific path length delay value (ΔL) provided in the arrayed waveguides region. The modelling procedure is divided into following five steps:

(a) Simulate and define the fundamental mode at given input locations.

We directly use the power normalized Gaussian function (Eq.(3.18)) as the default input mode as it provides a good approximation to the real input waveguide mode (channel and slab waveguides). And we also add an additional function into the current AWG model with the flexibility of loading random input mode to facilitate the mode shaping at the input aperture, which is essential for the flat-top AWG design. In Eq.(3.18) x_i represents the mode spatial location and ω_i denotes the mode radius (shown as the red Gaussian curve in Fig 3. 3).

$$\mathrm{f}(x_i) = \sqrt[4]{\frac{2}{\pi {\omega_i}^2}}\, e^{-(x_i/\omega_i)^2} \tag{3.18}$$

(b) Mode propagation in the input star-coupler region

We use Fraunhofer diffraction equations (Spatial Fourier transformation) to get the mode profile after the free propagation in the input star-coupler region since the length of the star coupler usually satisfies the Fraunhofer diffraction regime as shown in Eq.(3.19). In Eq.(3.19), *f* denotes the star-coupler radius, *D* represents the mode diameter, and λ represents the functioning wavelength (shown as the red sector and the large red Gaussian curve in Fig 3. 3).

$$\mathrm{f} > \frac{\pi D^2}{4\lambda} \tag{3.19}$$

(c) Mode coupling and propagation in arrayed arms of waveguides

We utilize Eq.(3.18) to define the individual mode profile in each arrayed arm of waveguides. We will calculate the overlap integral between the diffracted mode profile after step.(b) and the arrayed waveguides mode profile to define the power coupling ratio into each arm. The mode propagation in entire arrayed waveguides will follow the phasor definition, adding the propagation loss and

phase corresponding to the path-length delay value (ΔL) (shown as the blue curves and arrows in Fig 3. 3).

(d) Mode propagation/re-focus in the output star-coupler region

The mode profile at the end of arrayed waveguides will arrive at the arc of the output star-coupler. This mode profile will once again pass through a free propagation region (blue sector in Fig 3. 3) following the spatial Fourier transformation in the Fraunhofer diffraction regime. This will provide the refocused mode at output waveguides locations.

(e) Mode coupling into the output waveguide

The refocused mode profile from step.(d) will go through an overlap integral step together with the local fundamental waveguide mode at the output waveguide either defined by the Eq.(3.18) or the user defined mode profile. This overlap integral result is the final coupling ratio for this specific wavelength. Thus, by repeating the step (a)~(e) for the given wavelength range, we could model the transmission spectrum of the designed AWG.

3.2.2 Modelling and Simulation Results for standard AWG

This section will present step-by-step simulation/modelling results for an 8 channel, 200 GHz channel spacing, Gaussian AWG Demux at 1550 nm center wavelength. All the systematic and material design parameters are shown in Table 4 for the target AWG Demux.

We select the 200 nm-thick Si_3N_4 waveguide platform for this AWG Demux for the future integration functioning as a multi-wavelength laser combiner. As described in chapter 2, we have simulated and chosen the single-mode waveguide width to be 1.5 μm, the multimode waveguide width to be 2.5 μm, and the minimum bending radius to be 100 μm to maintain the tradeoff between the loss performance and the device scale. Following design equations and guidelines shown

previously in this chapter, we obtain essential design parameters listed in Table 4. The focal length is simulated to be around 234.1 μm, and the input/output/arrayed waveguides width is set to be 3.0 μm in to provide specific mode expansion before star-couplers for the loss reduction. The arrayed waveguides arm pitch is 3.25 μm, indicating the minimum gap (250 nm) in the star-coupler region, which is our current lithography resolution. All waveguide index information is pre-simulated following techniques shown in chapter 2. The grating order is chosen to be 60, and we could further reduce it if we want to reduce the transmission spectrum roll-off.

Table 4 Design parameters for 1550nm 8×200GHz AWG Demux

Design Parameters	Symbol	Design Values
Center wavelength	λ_0	1.55 μm
Number of channels	N_{ch}	8
Channel spacing	CS	200 GHz
Focal length	f_i and f_o	234.09 μm
Waveguide group index	$n_g(\lambda_0)$	1.820199
Waveguide effective index	$n_{eff}(\lambda_0)$	1.562801
Slab effective index	$n_g(\lambda_0)$	1.584236
Number of arms	N_{arms}	44
Input waveguide width	w_i	3.0 μm
Arrayed arms pitch	w_{arms}	3.25 μm
Output waveguide width	w_o	3.0 μm
Path length difference	ΔL	59.51 μm
Grating order	m	60
Wavelength points	N	400
Modelling Time	T	251.37 s

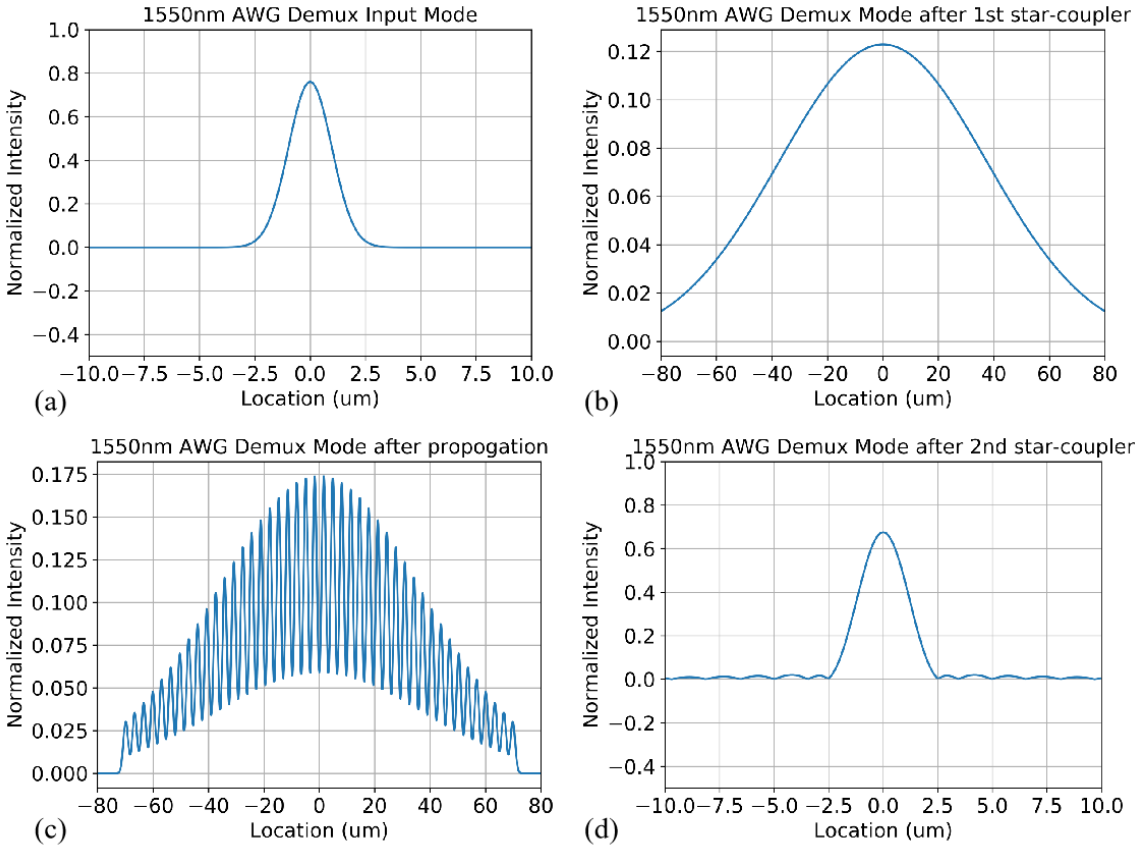

Fig 3. 4 1550nm 8×200 GHz AWG Demux modelling steps: (a) The Gaussian approximation of the fundamental mode at the input waveguide; (b) The mode received at the end of the input star-coupler; (c) The mode received at the end of the arrayed waveguides; (d) The refocused mode at the center output waveguide.

Fig 3. 4 shows intermediate simulation results at the center wavelength 1550 nm following modelling steps shown in chapter 3.2.1. We use the power normalized Gaussian function with the mode radius ~ 1.38 μm to present the input mode profile. Fig 3. 4.(b) shows the normalized mode profile at the end of the propagation in the input star-coupler. We could see that the Gaussian mode is expanded in this free propagation region to a mode radius ~ 41 μm. The number of arrayed arms and the arrayed arms pitch are both set to cover over 95% of the mode power to minimize the power loss in this transition region. Fig 3. 4.(c) shows the mode profile at the end of the arrayed

waveguides region. Most of the mode power from Fig 3. 4.(b) is well captured into the arrayed arms, and different phase shifts are added to each arrayed arm under the path length difference of 59.51 μm. In the end, the mode travels through the output star-coupler and refocus at the output waveguides interface with the mode profile shown in Fig 3. 4.(d).

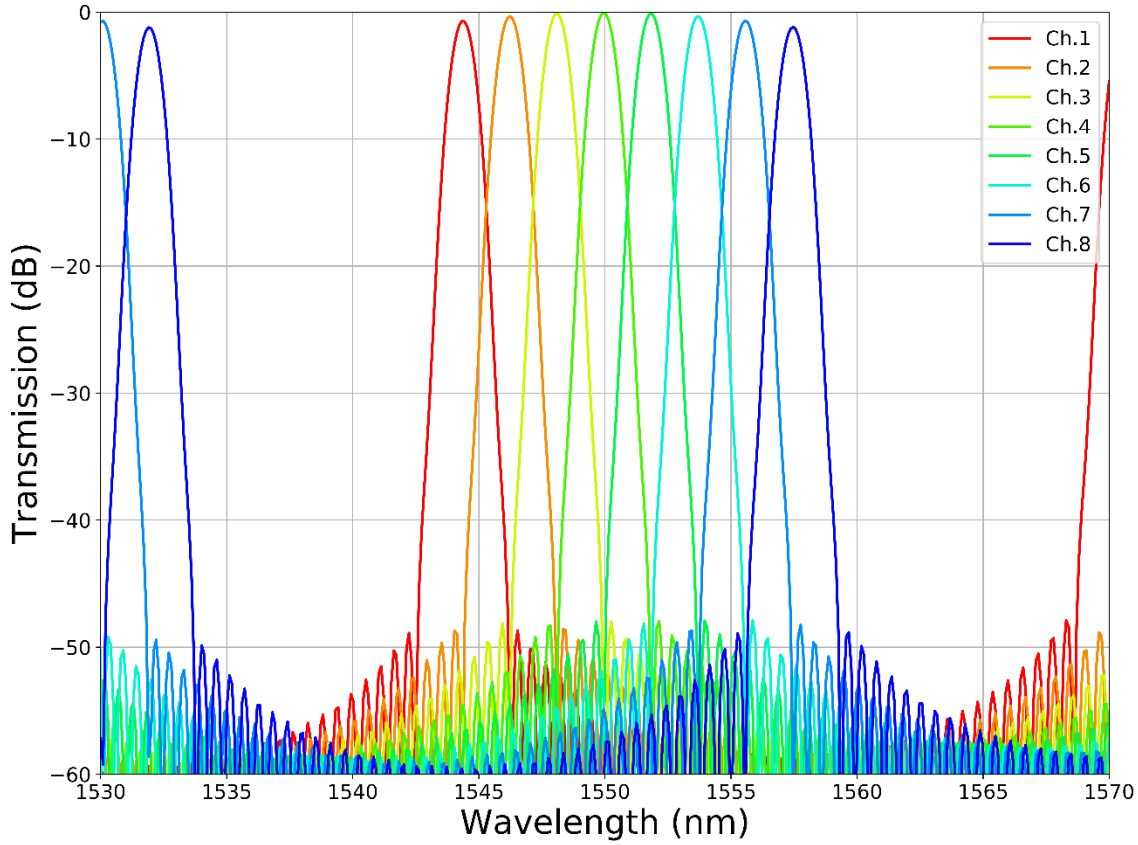

Fig 3. 5 Simulation result of the 8 channel 200 GHz channel spacing AWG Demux at 1550nm center wavelength.

We finally use this mode profile to perform a mode overlap integral with the output waveguide mode to get the transmission power ratio. This whole process for the center wavelength 1550 nm is presented in Fig 3. 4 where we have a successful mode reproduction at the center output. We

repeat this simulation process for the wavelength range of 40 nm around the center wavelength with 400 wavelength points and combine all power transmission ratios shown in Fig 3. 5.

The center wavelength precisely locates at 1550 nm with the average channel spacing around 200 GHz. We see that the transmission spectrum of the No.60 grating order is distinctly separated from the adjacent grating orders to reduce the roll-off of the spectrum to ~0.98 dB. The center two channels possess the lowest transmission loss (0.04 dB). This transmission loss will increase if we include a more accurate waveguide loss model into simulation steps in the future. We also get the average channel bandwidth to be ~115 GHz. The inter-channel and intra-channel crosstalk are at ~50 dB level due to the simple assumption of zero loss in all AWG sections. The total simulation time for 400 wavelengths points is 251 s, which is suitable for a personal laptop.

Table 5 Design parameters for 1280 nm 8×200GHz AWG Router

Design Parameters	Symbol	Design Values
Center wavelength	λ_0	1.28 μm
Number of channels	N_{ch}	8
Channel spacing	CS	200 GHz
Focal length	f_i and f_o	107.97 μm
Waveguide group index	$n_g(\lambda_0)$	1.78609
Waveguide effective index	$n_{eff}(\lambda_0)$	1.523770
Slab effective index	$n_g(\lambda_0)$	1.571710
Number of arms	N_{arms}	32
Input waveguide width	w_i	2.4 μm
Arrayed arms pitch	w_{arms}	2.65 μm
Output waveguide width	w_o	2.4 μm
Path length difference	ΔL	104.162 μm
Grating order	m	126
Wavelength points	N	400
Modelling Time	T	219.17 s

All systematic and material design parameters for an 8 channel, 200 GHz channel spacing, Gaussian AWG router at 1280 nm center wavelength are shown in Table 5. We select the 150 nm-

thick Si_3N_4 waveguide platform for this AWG Router application. As described in chapter 2, we have simulated and chosen the single-mode waveguide width to be 1.2 μm, the multi-mode waveguide width to be 1.9 μm, and the minimum bending radius to be 150 μm to achieve both the low-loss performance and the minimum device scale. Following design equations and guidelines shown in chapter 3.1, we get essential design parameters for 1280 nm AWGR on the 150nm-thick Si_3N_4 waveguide platform in the Table 5. The input and output waveguide width are set to be 2.4 μm, which is in the multimode regime. We use this particular design to reduce the mode expansion in the free propagation region. And it can further reduce both the star-coupler scale and the mode expansion loss. The grating order is chosen to be 126 to satisfy the router condition. The focal length is calculated to be ~108 μm, and the corresponding path length difference is ~104.2 μm. These two numbers are ideal simulation/modelling value, and we should provide various tweaks in the manufacturing run to mitigate the fabrication drift. All waveguide indices are simulated following techniques shown in chapter 2.

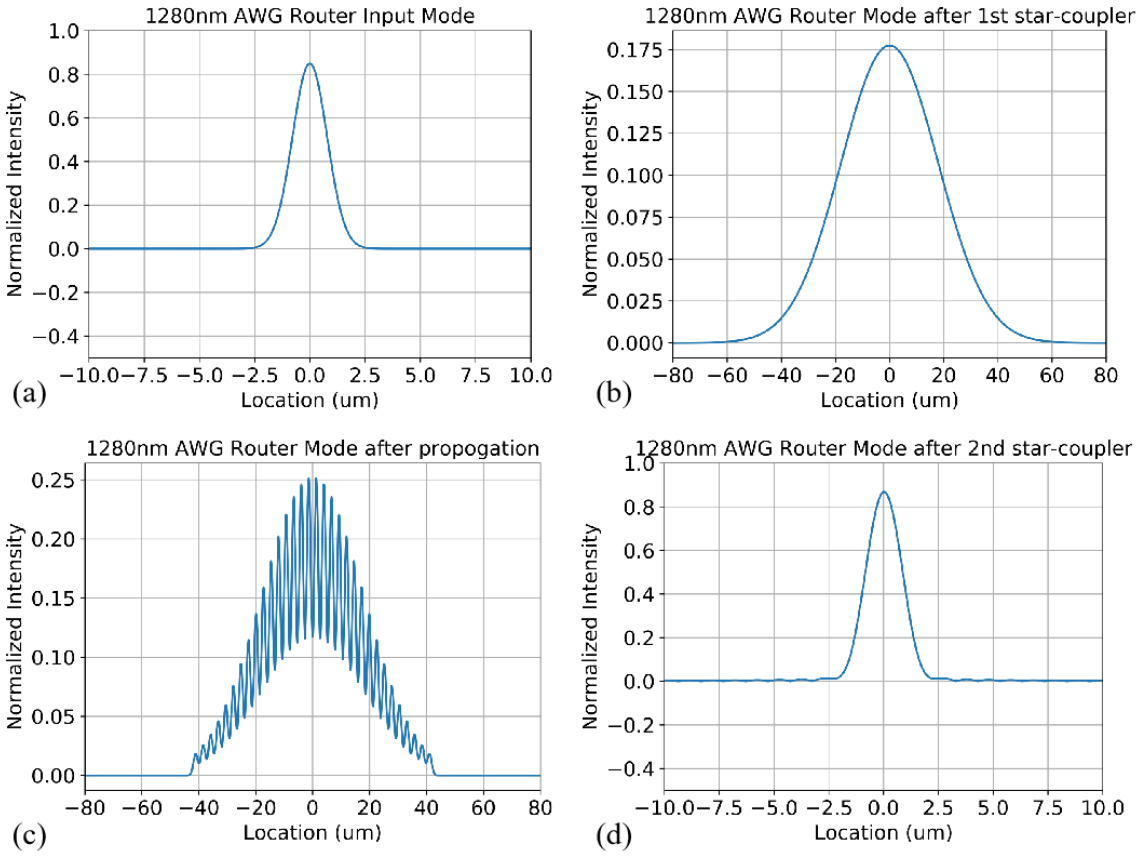

Fig 3. 6 The modelling steps of a 8 × 200 GHz AWG Router centered at 1280nm wavelength: (a) the Gaussian approximation of the fundamental mode at the input waveguide; (b) the mode received at the end of the input star-coupler; (c) the mode received at the end of the arrayed waveguides; (d) the refocused mode at the center output waveguide.

Fig 3. 6.(a) shows the normalized fundamental Gaussian mode at the 1280 nm center wavelength at the center input waveguide port with a mode radius of 1.1 μm. After the complete propagation in the 108 μm-long star-coupler region, the input mode profile expands at the beginning of the arrayed waveguides section shown in Fig 3. 6.(b). this mode profile is power normalized with the minimum loss resulting from the absorption and diffraction in the free propagation region. The current mode profile has a mode radius of ~22 μm, and above 95% of the mode power is captured by 32 arrayed waveguides. Some reflection and mode mismatch loss will occur at this interface.

Fig 3. 6.(c) presents the mode profile at the end of the arrayed waveguides. The fundamental Gaussian mode is separately coupled into individual arrayed waveguide, and the phase difference is applied through the path length difference (104.2 μm). In the end, this combined arrayed waveguides mode travels through the output star-coupler and refocus at the output waveguide interface following the Fraunhofer diffraction with the mode profile shown in Fig 3. 6.(d). This output mode profile is a precise mirror image of the input mode profile with a mode radius of 1.1 μm. And this output mode will be coupled into the center output waveguide with the power ratio governed by the mode overlap integral. We could maximize this power coupling ratio by choosing the same input/output waveguide aperture to maintain the best mode match condition. The whole process for the center wavelength 1280 nm simulation is shown in Fig 3. 6. We repeat the process for 400 wavelength points in the 40 nm wavelength range around the center wavelength for the transmission spectrum shown in Fig 3. 7.

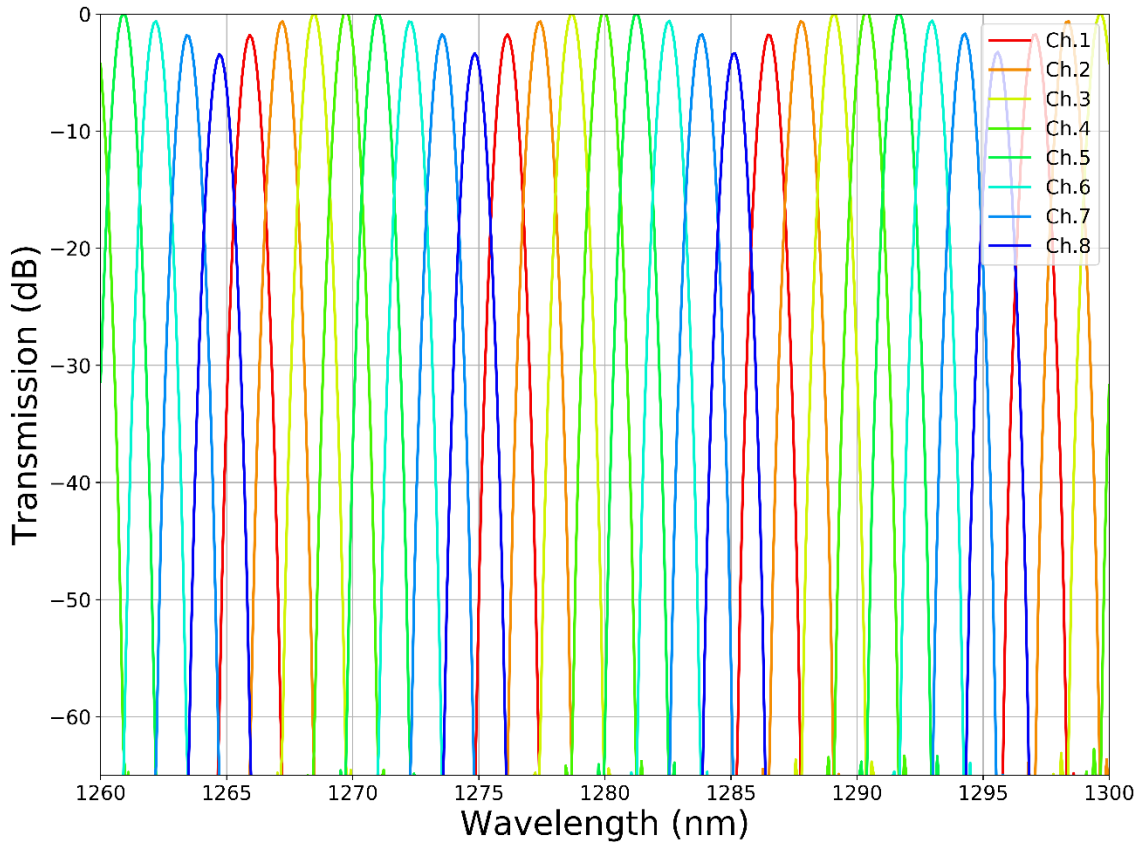

Fig 3. 7 Simulation result of the 8 channel 200GHz channel spacing AWG Router at 1280nm center wavelength.

The center wavelength (4^{th} channel output) locates closely to the desired 1280nm with the average channel spacing of approximately 200 GHz in Fig 3. 7. The adjacent order of spectrum is separated from the center order with the 200 GHz spacing satisfying the router requirement. The average insertion loss for the center order (grating order 126) is 1.16 dB with the maximum power roll-off of 3.3 dB. This power roll-off between the center and the side channel directly arises from the router application. The simulated inter-channel and intra-channel crosstalk are at 60 dB level. All these loss values and the crosstalk values will increase if we apply a more sophisticated waveguide loss model but they still provide a good indication of the overall performance. The average channel

3 dB bandwidth in Fig 3. 7 is 110 GHz. In the end, the entire simulation time of total 400 points is 219.17 s on a personal laptop.

3.2.3 Modelling and Simulation Results for flat-top AWGs

To facilitate the dense integration of an optical filter/router for the coarse wavelength division multiplexing (CWDM) application in the datacenter-to-datacenter and rack-to-rack communication, various techniques have been developed to flatten and broaden the AWG transmission passband. There are two popular approaches to create such a flattened transmission response in AWGs. One is to generate flattened or even concave mode field distribution at the input waveguide using parabolic waveguide horns [27]. The other is to use multimode interference couplers to create such flattened mode field distribution at input waveguides [28], [29]. We choose the second approach (multimode interference couplers) on our 200 nm-thick Si_3N_4 waveguide platform at the CWDM wavelength grid (center wavelength at 1291 nm), considering the tradeoff between the device scale and the loss reduction.

Table 6 Design parameters for 1291nm 4× 3.5THz Flat-top AWG Router

Design Parameters	Symbol	Design Values
Center wavelength	λ_0	1.291 μm
Number of channels	N_{ch}	4
Channel spacing	CS	3500 GHz
Focal length	f_i and f_o	88.40 μm
Waveguide group index	$n_g(\lambda_0)$	1.878574
Waveguide effective index	$n_{eff}(\lambda_0)$	1.557210
Slab effective index	$n_g(\lambda_0)$	1.628056
Number of arms	N_{arms}	24
Input waveguide width	w_i	2.0 μm
Arrayed arms pitch	w_{arms}	2.25 μm
Output waveguide width	w_o	6.5 μm
Path length difference	ΔL	10.78 μm
Wavelength points	N	200
Grating order	m	13
MMI Length	L_{MMI}	28.55 μm
MMI Width	W_{MMI}	7.0 μm

Modelling Time	T	202.46 s

As described in chapter 2, we have simulated and chosen the single-mode waveguide width to be 1.0 μm, the multi-mode waveguide width to be 1.7 μm, and the minimum bending radius to be 150 μm to achieve a good tradeoff between the low-loss performance and the minimum device scale. Following design equations and guidelines shown in chapter 3.1, we calculate essential design parameters for a 1291 nm-wavelength AWGR on the 200 nm-thick Si_3N_4 waveguide platform in Table 6. The most important simulation step is the multimode interferometer presented in Fig 3. 8. A simulation sketch for the 25 μm-long, 4.5 μm-wide MMI region is shown in Fig 3. 8.(a). The single mode inserted at the 1 μm wide input aperture will initiate higher order modes in the multimode region. Those who satisfy the constructive interference condition will survive and contribute to the interfered mode in the multimode region. As shown in Fig 3. 8, at a certain multimode length, we could capture the optical mode with desired flattened or concave electric field profile (highlighted as the grey region). Through iterations, we conclude that the MMI region with the length of 28.55 μm and the width of 7 μm could provide the best mode profile at the input aperture shown in Fig 3. 9.(a). We also add a taper region before the MMI to expand the input optical mode to reduce the mode mismatch. The waveguide width is linearly tapered from 1.0 μm to 2.0 μm, followed by the multimode section. The output waveguide width is simulated to be the best at 6.5 μm to maintain a good overlap integral with the MMI mode profile. Besides the MMI region parameters, we set the focal length of the AWG to be 88.40 μm and the corresponding path length difference to be 10.78 μm for a successful router application at the grating order thirteen. 24 arrayed waveguides with the 2 μm width are placed evenly at the input/output star-coupler for the maximum power transmission.

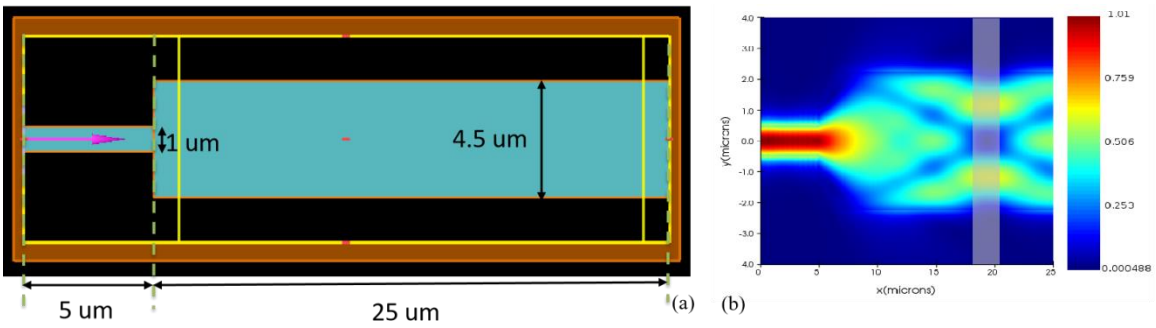

Fig 3. 8 (a) MMI simulation regime in FDTD software with 1μm single mode waveguide width and 4.5 μm multi-mode waveguide width; (b) The mode power distribution in the simulation regime where the grey region is the area of interest.

Fig 3. 9.(a) illustrates the mode profile at 1291 nm wavelength at the end of the MMI region with two peaks and a dip in between. The overlap integral between this mode profile and a traditional Gaussian mode profile will provide a flat spectrum response over the wavelength range where the mode profile in Fig 3. 9.(a) maintains. The peak distance and the dip depth could be engineered by chosen different MMI length and width values for the optimally flat response performance. After the propagation in the 88.40 μm free propagation region, this optical mode profile arrives at the beginning of the arrayed waveguides section with the shape shown in Fig 3. 9.(b). Fig 3. 9.(c) provides the mode profile at the end of the arrayed waveguides section where the 10.78 μm path length difference induces specific phase shifts. The full mode profile is a combination of individual mode profiles in all 24 arrayed waveguides. Finally, Fig 3. 9.(d) shows the refocused mode at the center output waveguide, similar to the input optical mode with certain loss reduction. Thus, the whole step-by-step simulation process for the center wavelength 1291 nm is presented in Fig 3. 9. We repeat this simulation process for 200 wavelength points in the 100 nm wavelength range around the center wavelength and obtain the power transmission spectrum shown in Fig 3. 10.

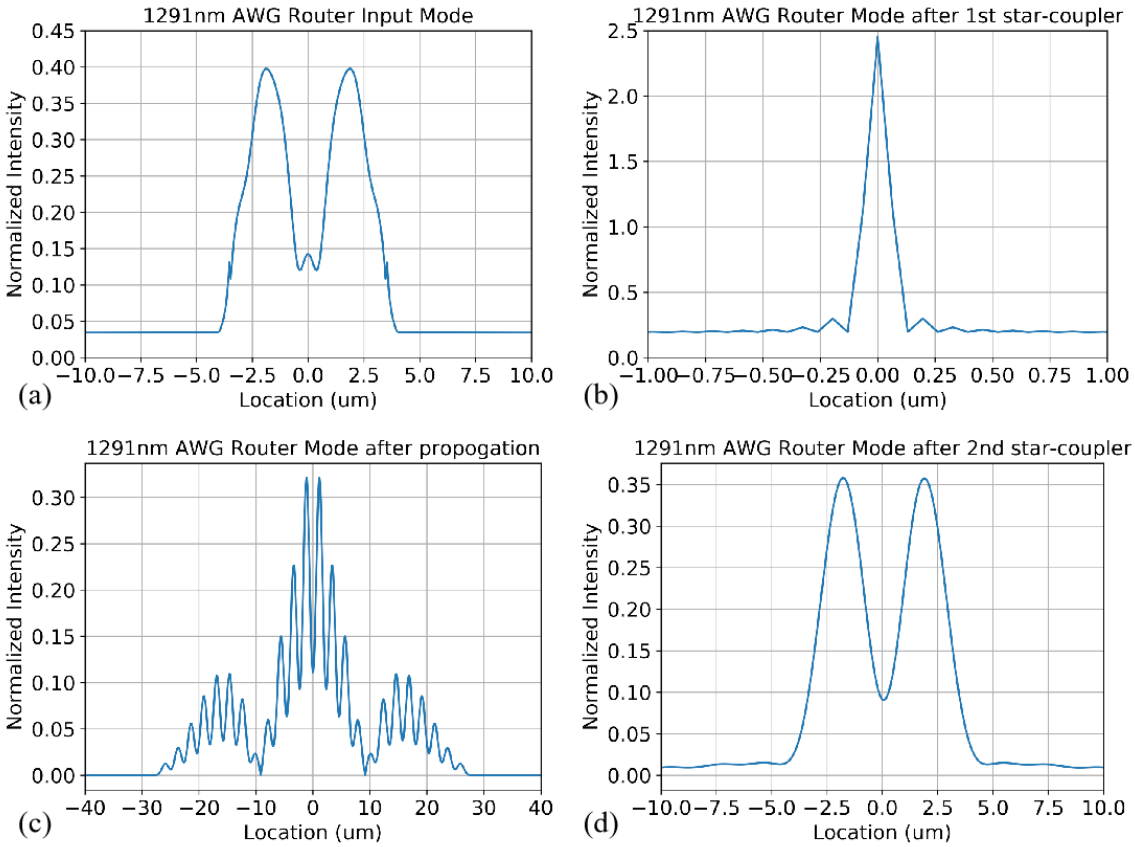

Fig 3. 9 The modelling steps of a 4×3.5THz AWG Router centered at 1291 nm wavelength: (a) the simulated input mode in the MMI region from Fig 3. 8.(b); (b) the mode received at the end of the input star-coupler; (c) the mode received at the end of the arrayed waveguides; (d) the refocused mode at the center output waveguide.

The center wavelength (2nd channel output) locates closely to the desired 1291 nm with the 3 dB bandwidth ~ 3.3 THz. The average insertion loss of the center order (grating order 13) is 6.81 dB with the maximum power roll-off of 3.06 dB. This relatively high insertion loss should result from the mode mismatch between the MMI mode and the output waveguide mode, and the transmission loss within the AWG region. This spectrum simulation provides a good indication of the crosstalk level around 25 dB. Lastly, the entire simulation time of total 200 points is 202.46 s.

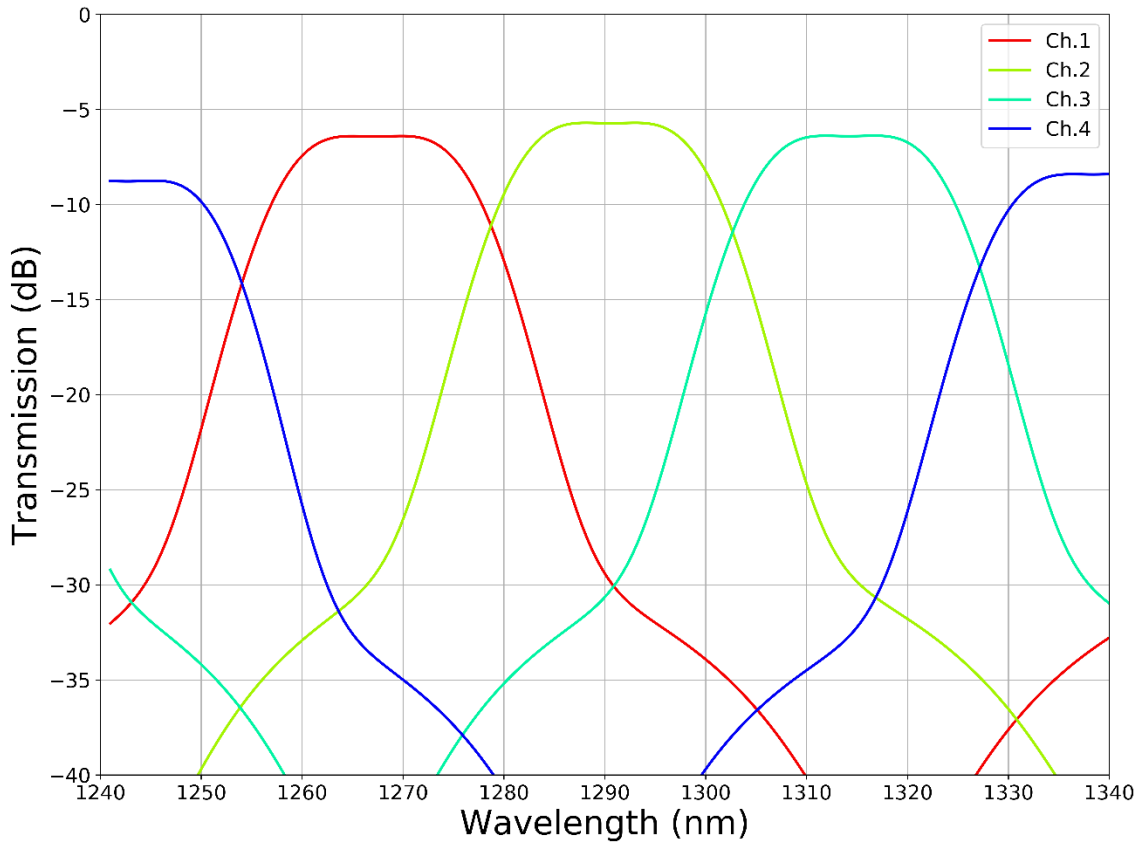

Fig 3. 10 Simulation result of the 4 channel 3.5 THz channel spacing AWG flat-top Router at 1291 nm center wavelength.

The pseudo codes for the AWG simulation/modelling are shown below:

1) class AWG_Gaussian: #AWG simulation section for the Gaussian input mode

    def __init__(): #Define design paramenters

    def Calculation(): #Simualtion in the given wavelength range

        for wl in wl_list: #wavelength sweep

            Set the Gaussian input mode profile

Diffraction in the 1st star-coupler

Coupling into arrayed waveguides

Adding phase delays/loss at the end of arrayed waveguides

Diffraction in the 2nd star-coupler

Coupling into output waveguides

Writing data into files

def Plot_Figure():

2) class AWG_Random_Input: #AWG simulation section for the given input mode

def __init__(): #Define design paramenters

def Calculation(): #Simualtion for the given wavelength range

for wl in wl_list: #wavelength sweep

Set the given input mode profile

Diffraction in the 1st star-coupler

Coupling into arrayed waveguides

Adding phase delays/loss at the end of arrayed waveguides

Diffraction in the 2nd star-coupler

Coupling into output waveguides

Writing data into files

def Plot_Figure():

3.3 Design and Layout

3.3.1 AWG Design and Layout Environment

We developed an in-house AWG design and layout package named “Chhogori” based on the theory and simulation strategies shown in the previous section. The “Chhogori” package is built on the IPKISS design flow and contains four sub-packages: 1) The “Material” package includes all material and platform-related default parameters; 2) The “StarCoupler” package includes the design routine of the star-coupler region customized for various applications (Rowland mounting, MMI inputs, parabolic inputs); 3) The “Routing” package includes all necessary routing algorithms of the arrayed waveguides region to achieve the target path length difference; 4) The “AWG” package could call all functions and algorithms defined the in previous three sub-packages and layout the AWG Demux or Router in the given shape. I will introduce these four sub-packages in following sections.

We start the AWG design and layout process by choosing the desired waveguide platform. All essential waveguide data (waveguide width, effective index, group index, bending radius) are defined in the “Material” sub-package. We could also get optimal device parameters following the simulation process in the previous section. Once we have all design parameters, we could refer to the design flow chart shown in Fig 3. 11 to complete the AWG design and layout. The flow chart begins with a checkpoint on whether we are aiming for a router or not. To design a router, we need to meet the demanding requirement in Fig 3. 11.Eq.(1) that the free spectrum range (FSR) of the device equals the multiplication of input/output channel numbers and the channel spacing (CS). The next step in the router design is to calculate the star-coupler region diameter through Fig 3.

11.Eq.(2). d_a represents the pitch between adjacent arrayed waveguides, N_{arms} represents the number of arrayed waveguide arms, and θ_{da} denotes the mode divergence angle in the star-coupler region. For a given center wavelength λ_0, we could calculate the arrayed arms grating order m following the Fig 3. 11.Eq.(3). This calculated grating order m value might not be an integer. Thus, we take the ceiling value of this m value as a new $\hat{m}$ value, an integer grating order satisfying the constructive interference condition. Fig 3. 11.Eq.(5) represents the necessary step to update the path length difference value according to the new integer grating order $\hat{m}$. Finally, we could use the Fig 3. 11.Eq.(6) to get the angular position of each input/output waveguide. We now have all design parameters for an AWG router, and the "AWG" sub-package could help to layout the AWG router for the further manufacture.

On the other hand, the right column tree in Fig 3. 11 presents the design flow for the demultiplexer application. We do not need to meet the FSR requirement in the router case, and we should control the FSR value to reduce the channel loss roll-off. In this case, we will define the grating order (as shown in the Fig 3. 11.Eq.(8)) in the first step and derive other design parameters. We should notice that the maximum grating order m_{max} is the exact router case, and the possible grating orders used in the demultiplexer application should not exceed this value. In the end, we could use Fig 3. 11.Eq.(9) and Fig 3. 11.Eq.(10) to obtain angular/spatial positions of input/output waveguides and the exact path-length difference. The design checkpoint "Does the angle meet requirements" sets a design loop so that we should pick the optimal grating order integer value $\hat{m}$. This grating order should satisfy both FSR requirements and the minimum input/output waveguides separation requirement.

Fig 3. 12 presents a sketch of the circular AWG designed and patterned by the “Chhogori” design package. A complete layout should contain input/output waveguides, corresponding routing sections, and two star-couplers.

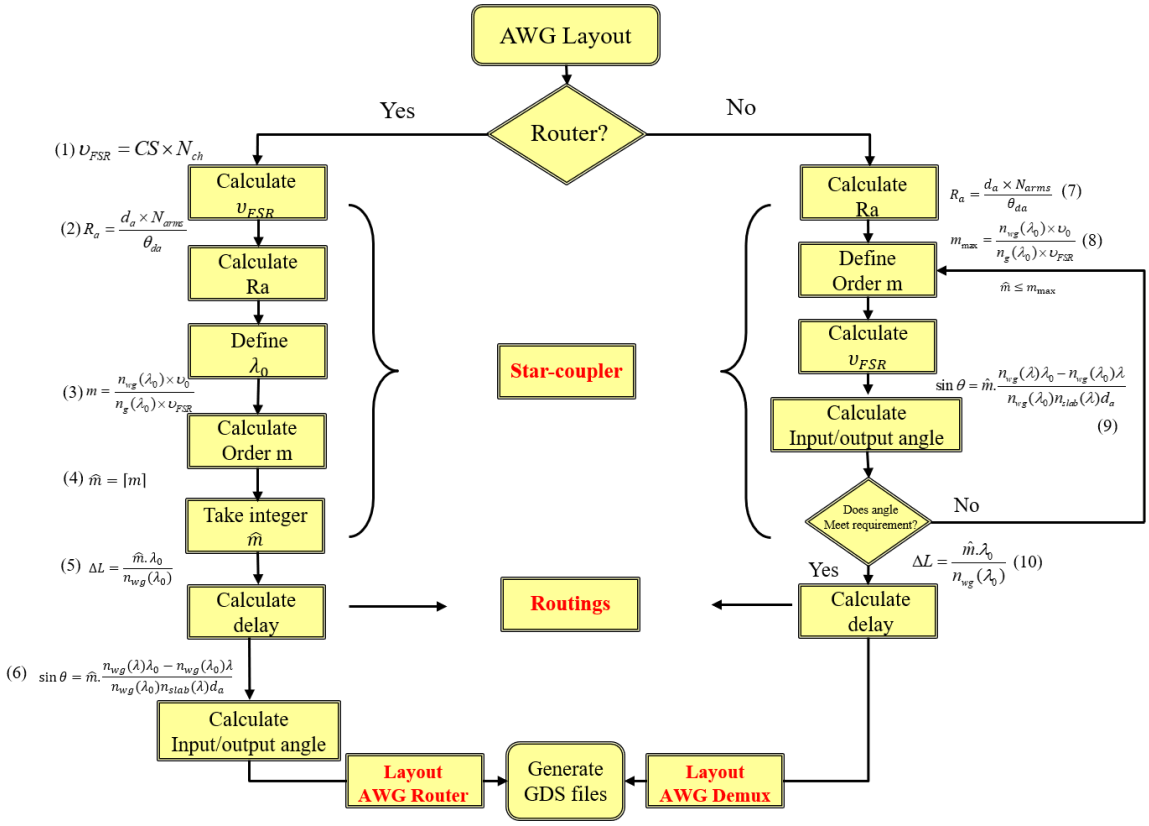

Fig 3. 11 AWG design flow chart for demultiplexer and router applications.

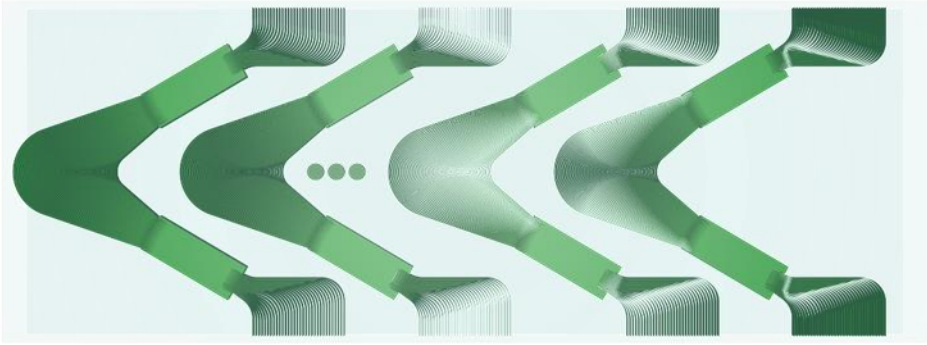

Fig 3. 12 Circular AWG layout example utilizing the “Chhogori” design package.

3.3.2 Design Routine for Star Couplers

The “Material” sub-package contains the platform indices information for following designs. A complete material database contains the rest of design parameters: (1) single-mode waveguide width (w_{sm}); (2) multi-mode waveguide width (w_{mm}); (3) waveguide effective index (n_{eff}); (4) waveguide group index (n_g); (5) slab waveguide index (n_{slab}); (6) bending waveguide index (n_{bend}); (7) minimum bending radius (R_{min}); (8) minimum taper length (T_{min}); (9) star-coupler diffraction angle (α_{diff}). We could continue the design flow with these given parameters. Fig 3. 13 shows layout details for a confocal mounting star-coupler and a Rowland mounting star-coupler. We use combined parameters shown in Table 6 for the design shown in Fig 3. 13.(a). The full layout consists of 4 steps: (1) Complete the input waveguides sector shown in color black; (2) Complete the arrayed waveguides sector shown in color green; (3) Complete the free propagation region shown in color blue; (4) Place input waveguides and arrayed waveguides corresponding to the simulated angular distribution. The input waveguides sector and the arrayed waveguides sector share the same bending radius (focal length), testifying the confocal mounting. The arc in the sector should be chosen with the optimal angle that maintains the tradeoff between the power reduction and the device footprint. We usually place four dummy waveguides at both sides of arrayed waveguides so that the side waveguide could have similar optical mode excitation compared to center ones. We should place a certain number of dummy waveguides besides input waveguides for the same reason. All the taper transition regions in input waveguides and arrayed waveguides should not be shorter than the T_{min} value. Therefore, we could achieve the adiabatic condition for all tapers. In the free propagation region, we have full control of the angle of two arcs so that there is no extra power leakage. In the end, all input waveguides locations and arrayed waveguides

locations (coordinates and angles) are open to the "AWG" sub-package for further integration. Fig 3. 13.(b) introduces the alternative Rowland mounting configuration in the free propagation region. The input waveguides sector takes only half of the focal length as the bending radius. This configuration should help to reduce the third-order image loss in the large number of channels situation.

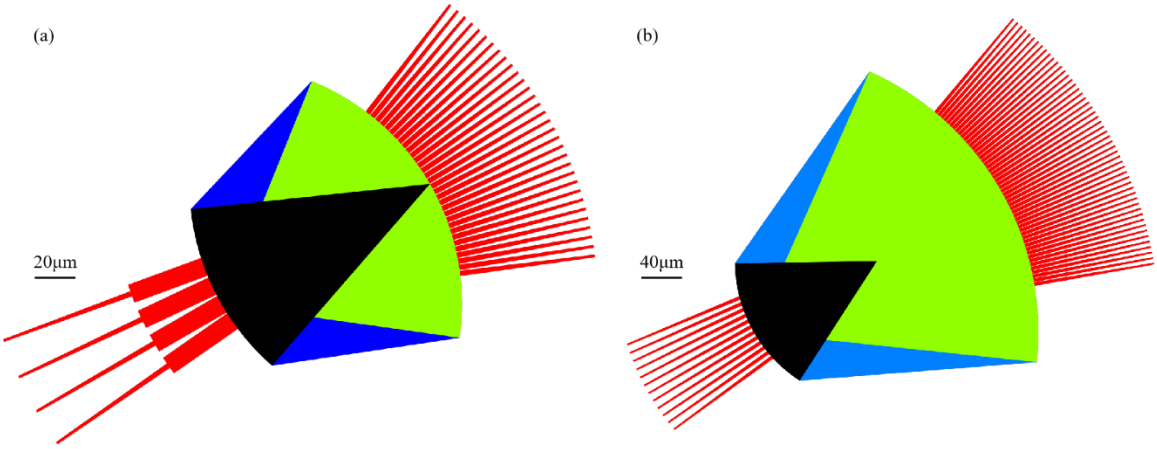

Fig 3. 13 (a) Star-coupler layout with MMI input waveguides and confocal mounting; (b) Star-coupler layout with standard input waveguides and Rowland mounting.

3.3.3 Design Routine for Box Shape AWGs

One important routing technique in the "Routing" sub-package is the box shape routing illustrated in Fig 3. 14. One arm of the routing contains (a) extending waveguides; (b) the first waveguide tapers from the single mode region to the multimode region (tp1); (c) the first straight multimode waveguides section (str1); (d) the second waveguide tapers from the multimode region to the single mode region (tp2); (e) the 90 degrees bending (b1); (f) the third waveguide tapers from the single mode region to the multimode region (tp3); (g) the second straight multi-mode waveguides section (str2). The other arm of the routing is a mirror image of the previous component. So the path length difference condition should be simplified shown in Eq.(3.19).

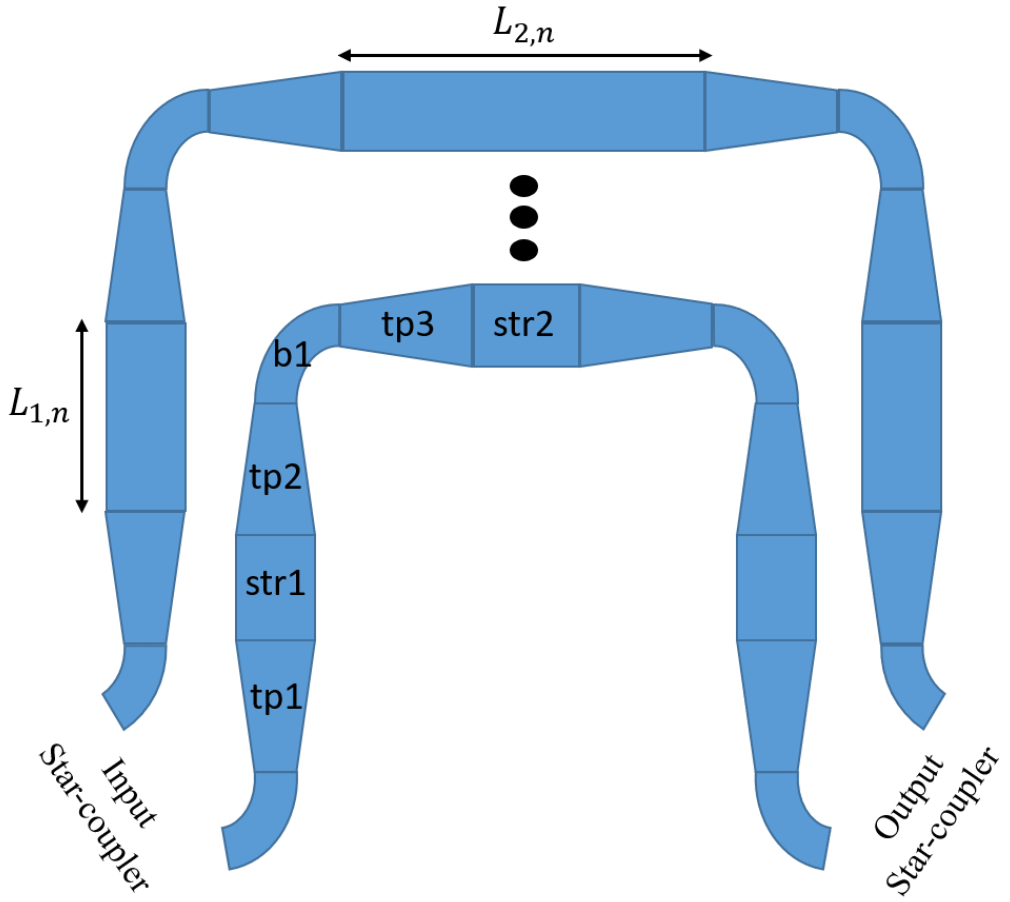

Fig 3. 14 detailed Box shape routing sketch from the input star-coupler to the output star-coupler.

$$\Delta L = \left(2 \times L_{1,n} + L_{2,n}\right) - \left(2 \times L_{1,n-1} + L_{2,n-1}\right) \tag{3.19}$$

A significant advantage of the box routing shown in Fig 3. 14 is that the path length difference only comes from straight multimode waveguide sections (str1 and str2). We keep tapers and the bending to be the same for each arrayed arm. This design immediately removes the loss variation resulting from the waveguide bending. Another benefit of this routing is that we intentionally taper the single mode waveguide to the multimode waveguide. The fundamental optical mode profile is more constrained in the multimode waveguide. It can further reduce the propagation loss resulting

from the waveguide sidewall roughness inherently in the device fabrication process. However, the total routing length is much longer than the circular routing introduced below, and the device footprint is compromised. Because we only create the path length difference in multimode waveguide sections, there is a minimum path length difference required for this routing technique. In other words, this routing technique might not be able to satisfy the design that needs either larger channel spacing or larger device FSR. Above all, the box shape routings are favorable to high index contrast waveguide platforms, and we have delivered high-quality AWGs in the thick Si_3N_4 waveguide platforms with this routing technique.

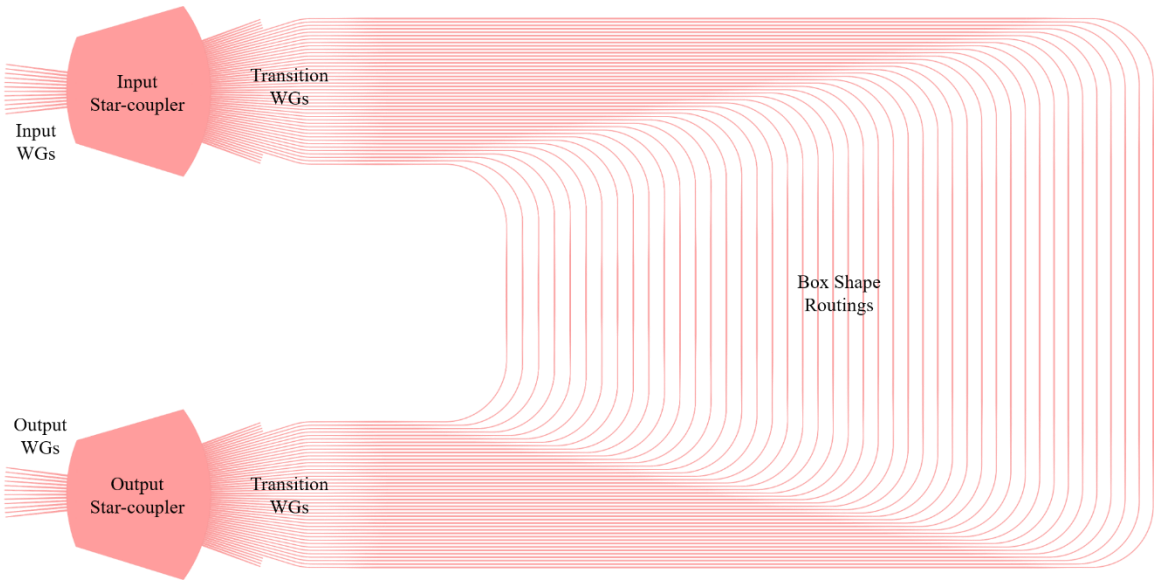

Fig 3. 15 8 channel 200 GHz channel spacing AWG Demux layout based on the design parameters shown in Table 4.

Fig 3. 15 presents the final layout of the 8 × 200 GHz AWG Demux detailed in chapter 3.2.2. The "BoxAWG" function in the "AWG" sub-package calls the desired star-coupler in the "StarCoupler" sub-package and the box shape routings in the "Routing" sub-package. The whole device is designed on the 200 nm-thick Si_3N_4 waveguide platform with a minimum routing length of 950

μm. We control the bending radius and the length of waveguides in the transition region so that the optical path is balanced. The separation between adjacent arrayed waveguides should be large enough so that there is no unnecessary power coupling between arrayed waveguides. All input and output waveguides are tapered to the single mode waveguide width.

3.3.4 Design Routine for Circular Shape AWGs

Fig 3. 16 shows the schematic circular shaper routing for the AWG design. Two star-couplers are separated by the distance S_iS_o denoted as L_{slab} and rotated by the angle θ ($A_jS_iS_o = T_oS_oS_i$). Each routing consists of two straight waveguides (A_iB_i, A_jB_j) with variable length and an arc waveguide (B_iC_i, B_jC_j) smoothly connecting the two straight waveguides. The path length difference relationship between the i-th and j-th routes requires:

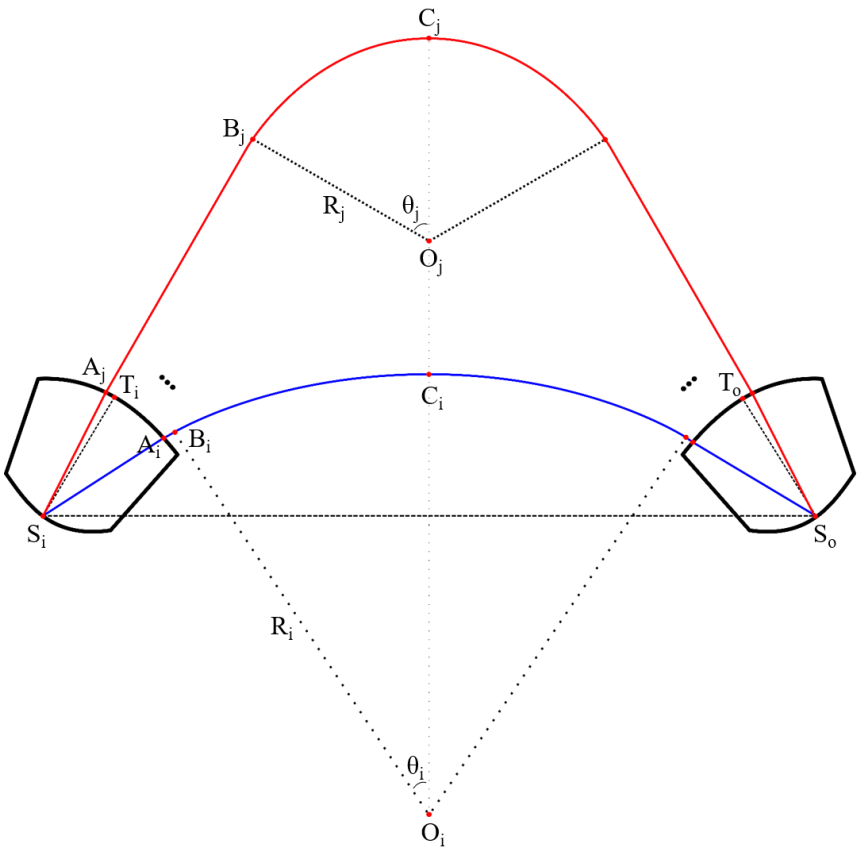

Fig 3. 16 Detailed circular shape routing sketch with i-th path shown in blue and j-th path shown in red.

$$L_j + R_j\theta_j = L_i + R_i\theta_i + (i-j)\frac{\Delta L}{2} \tag{3.20}$$

The horizontal geometric relationship between the i-th and j-th routes requires:

$$(f + L_j)\cos\theta_j + R_j \sin\theta_j = L_{slab}/2 \tag{3.21}$$

Where $L_{i,j}$ is the straight waveguide length connecting $A_{i,j}$ and $B_{i,j}$. $\theta_{i,j}$ is the arc angle connecting $B_{i,j}$ and $C_{i,j}$. $R_{i,j}$ is the arc radius that connects $B_{i,j}$ and $C_{i,j}$. For the total number of N arms in the circular design, we have $2N$ variables for L and R. We have N-1 equations from Eq.(3.20) and N equations from Eq.(3.21). Thus, we need to pre-define variables such as θ and L_{slab}. The manual control on these two design parameters offers us the freedom to balance the device footprint and the channel performance. Once we have all L and R values, we could finish the layout shown in Fig 3. 17 for the 1291 nm 4× 3.5 THz Flat-top AWG Router described in chapter 3.2.3.

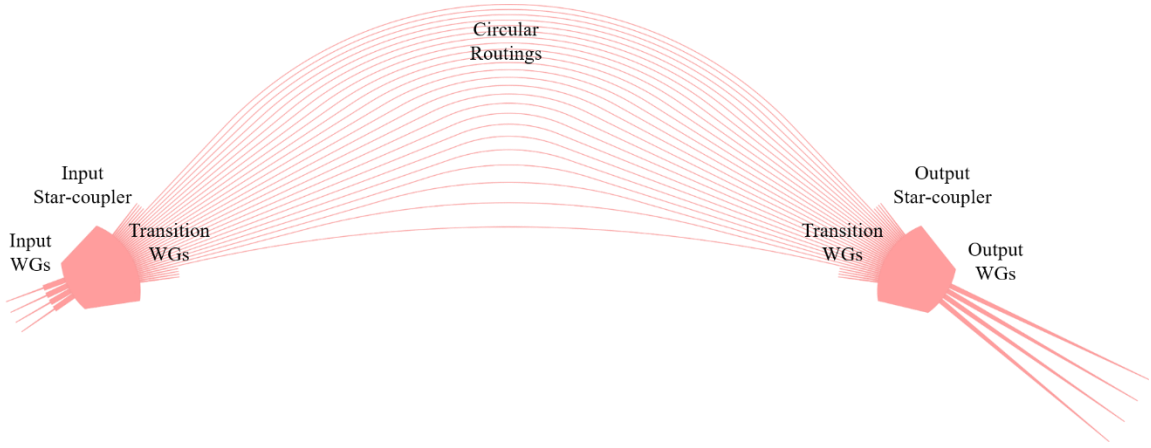

Fig 3. 17 1291nm 4× 3.5THz Flat-top AWG Router layout based on the design parameters shown in Table 6.

Fig 3. 17 shows the final layout of the 4× 3.5 THz Flat-top AWG Router detailed in Chapter 3.2.2. The “CircularAWG function” in the “AWG” sub-package calls the desired star-coupler in the

"StarCoupler" sub-package and the circular shape routings in the "Routing" sub-package. The whole device is designed on the 200 nm-thick Si_3N_4 waveguide platform with a minimum routing length of 840 μm. The star coupler detailed in Fig 3. 13.(a) enables the flat-top transmission with the flattened mode profile in the input MMI region. We need to fine-tune the θ and L_{slab} values to ensure that the minimum bending radius is satisfied, and the separation between adjacent arrayed waveguides is large enough for lossless propagation. The complete AWG size is 1400 μm × 420 μm.

3.4 Experimental Characterizations

This chapter introduces experimental characterizations of the AWG Demux and Routers in the communication O (1310 nm) and C (1550 nm) band. We manufactured the above AWG Demux and Routers following the ultra-low-loss Si_3N_4 fabrication process in the cleanroom in UC Davis and UC Berkeley. And we use the OVNA characterization setup for the C band devices and the traditional OSA characterization setup for the O band devices.

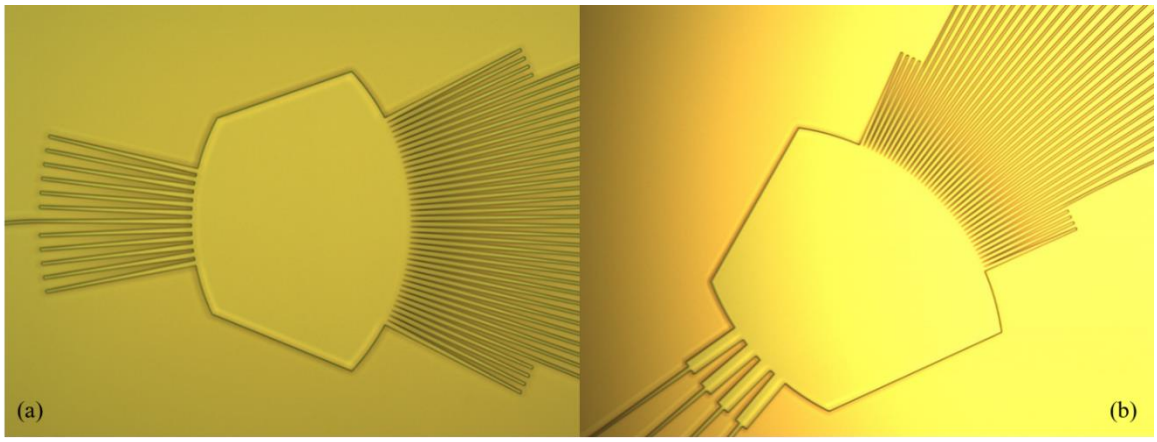

Fig 3. 18 (a) Etching photo of the 1550nm AWG Demux input star-coupler detailed in 3.2.2. (b) Etching photo of the 1291nm AWG input star-coupler detailed in 3.2.3.

We fabricated the Si_3N_4 devices using the 248 nm deep UV lithography process with the etching profile presented in Fig 3. 18. Fig 3. 18.(a) shows the 1550 nm wavelength AWG Demux etching

profile on the 200 nm Si_3N_4 layer. Four dummy waveguides are mounted beside the arrayed waveguides, and the AWG is connected at the center input. The designed 250 nm arrayed waveguides separation is well exposed, indicating the lithography quality. Fig 3. 18.(b) shows the etching profile of the 1291nm wavelength AWGR input star-coupler. The four input channels pass through the designed MMI region to create a flattened response over the 10 nm wavelength range.

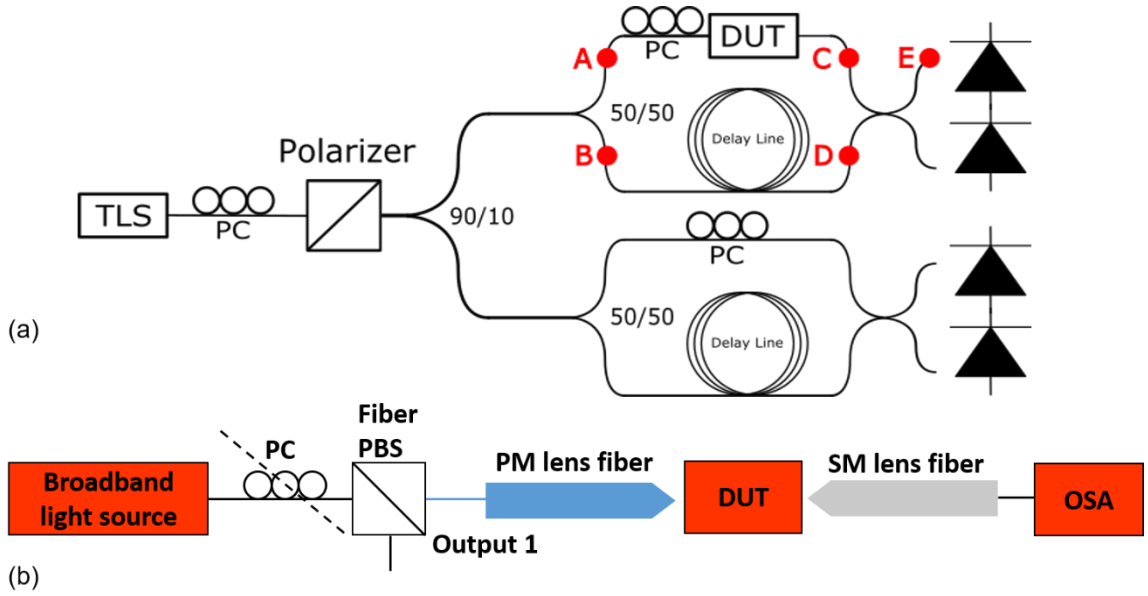

Fig 3. 19 in-house OVNA characterization setup of device's transmission matrix in C band. (b) characterization setup for O band devices using a broadband light source.

We use two setups shown in Fig 3. 19 for the AWG transmission characterization. The in-house optical vector network analyzer (OVNA) [30] setup is built on a fast sweep Laser source (TLS). The polarization of the laser light is controlled by the polarization controller (PC) and the following Polarizer. The 90/10 power splitter divides the light into the top and bottom routes. The laser mode travels through the interferometer containing the device-under-test (DUT) in the top route and arrives at the balanced detector. On the other hand, the laser mode goes through the bottom route, acting as a reference with no DUT presented. We keep the length of delay lines (optical fibers) to be the same in both routes. By comparing the data received at both balanced detectors, we could

derive the transmission matrix of the DUT at the given polarization in the wavelength range set by the TLS. Fig 3. 19.(b) illustrates the alternative characterization setup based on the broadband light source. This setup starts at the broadband light source emitting non-polarized light. We focus the light into the SMF-28 fiber via a collimated lens system and further direct the light beam through a fiber polarization beam splitter (PBS) to divide the light into two orthogonal polarizations. We fine-tune the polarization maintaining (PM) fiber (2.5μm spot size) into the specific TE mode direction utilizing the additional free space setup. Then we combine the PBS and the PM fiber to guide the light into the DUT successfully. At the output end, we use a 2.5μm spot size single mode (SM) lens fiber to collect the light power and send it into the optical spectrum analyzer (OSA) for data processing. The broadband light source sets the characterization wavelength range.

3.4.1 Characterization Results for C band AWGs

Fig 3. 20 shows the characterization result of the 8 channels 200 GHz channel spacing AWG Demux at the 1550 nm center wavelength designed and simulated in the previous sections. The design targets are 1550 nm center wavelength, 200 GHz channel spacing, and 2060 GHz FSR. We measure the center wavelength of the fabricated device to be 1552.62 nm with ~0.17% offset using the OVNA setup described in Fig 3. 19.(a). The average channel spacing is 200.07 GHz with an offset below 0.1%. The device FSR is measured to be 2100.6 GHz with ~2% offset. This 0.17% center wavelength drift is mainly due to the mismatch between simulation parameters and those parameters in the practical fabrication condition. Several designs and characterization loops should help to optimize waveguide platform models. The insertion loss of the center channel (Ch.4) is 0.78 dB, and the insertion loss of the side channel (Ch.1) is 1.43 dB. The inter-channel and intra-channel crosstalk are at the 30 dB level. The channel spacing and FSR values match the design and simulation targets. Furthermore, we observe the degradation of the loss performance compared

to the simulation data. The majority of the loss accumulation comes from the extra propagation loss and scattering loss resulting from device sidewalls.

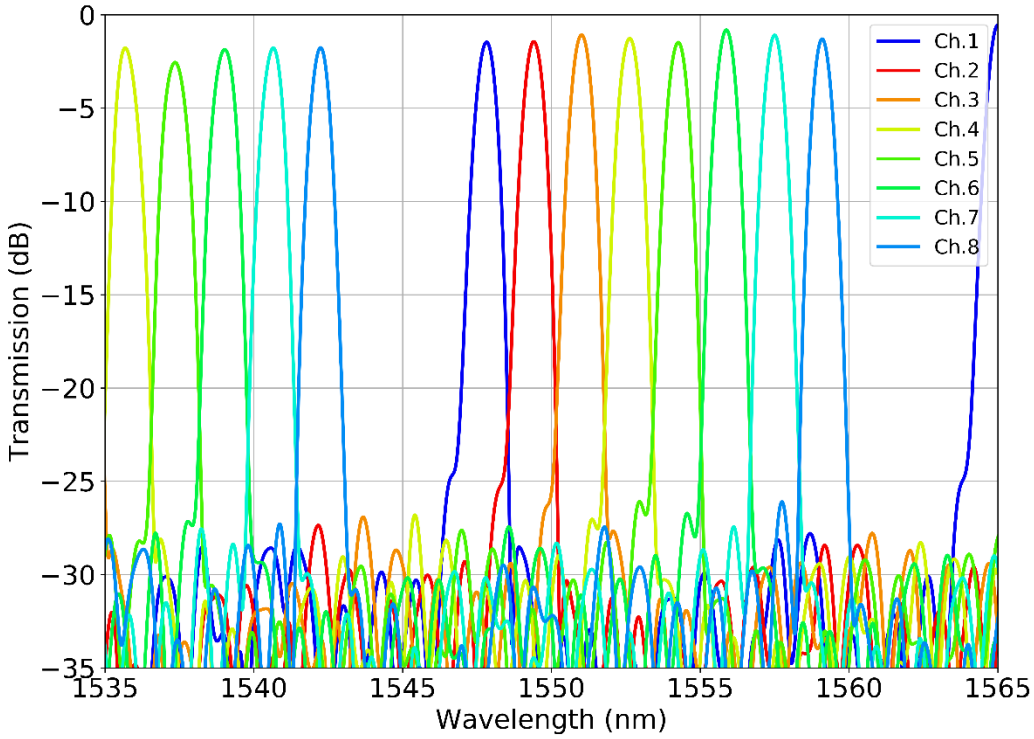

Fig 3. 20 Characterized result of the 8 channel 200 GHz channel spacing AWG Demux at 1550 nm center wavelength.

3.4.2 Characterization Results for O band AWGs

Fig 3. 21 shows the characterization result of the 8 channels 200 GHz channel spacing AWG Router at the 1280 nm center wavelength. The design targets are 1280 nm center wavelength, 200 GHz channel spacing, and 1600 GHz cyclic FSR. We characterize the center wavelength of the fabricated device to be 1282.93 nm with ~0.23% offset using the broadband light source setup introduced in Fig 3. 19.(b). The average channel spacing is 202.12 GHz with ~0.1% offset. The device FSR between the center grating order and the lower grating order is 1650 GHz with ~3.12%

offset. The 0.23% center wavelength drift is mainly due to the manufacturing variation. And the ~3.12% FSR drift is accumulated through each wavelength channel. The insertion loss of the center channel (Ch.4) is 1.23 dB, and the insertion loss of the side channel (Ch.1) is 3.7 dB. The inter-channel and intra-channel crosstalk are at the 30 dB level. We confirm the 3 dB transmission power roll-off between the center and side wavelength channels. The optical loss performance is approximately 1 dB higher than the simulation results.

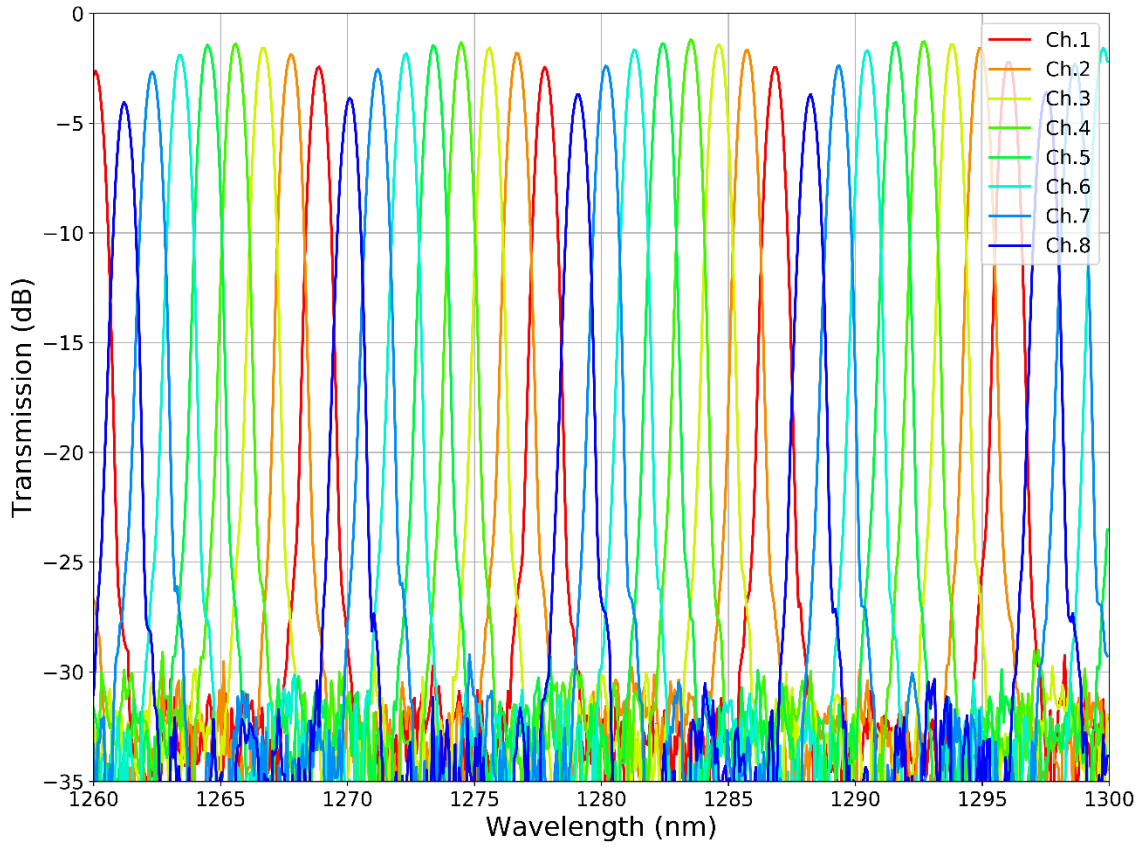

Fig 3. 21 Characterized result of the 8 channel 200 GHz channel spacing AWG Router at 1280 nm center wavelength.

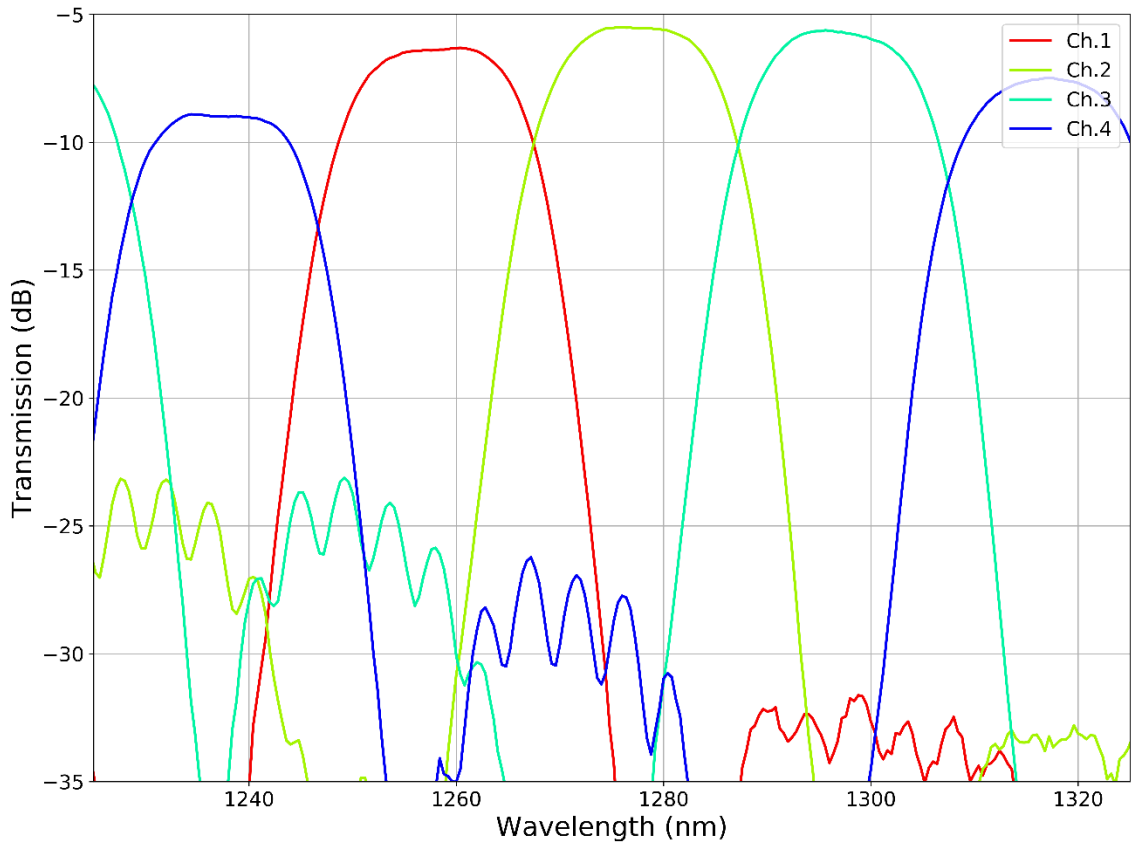

Fig 3. 22 Characterized result of the 4 channel 3.5 THz channel spacing AWG flat-top Router at 1291 nm center wavelength.

Fig 3. 22 presents the characterized result of the 4 channel 3.5 THz channel spacing AWG flat-top Router at 1291 nm center wavelength designed in the previous section. Design targets are 1291 nm center wavelength, 3.5 THz channel spacing, and 14 THz device FSR. We measure the device utilizing the broadband light source setup described in Fig 3. 19.(b). The center wavelength is characterized to be 1282.0 nm with a 0.7% offset. The average channel spacing is 3.506 THz with a 0.2% offset. The device FSR between the center grating order and the higher grating order is 14.7 THz with a 5% offset. We observe a higher loss value and a larger offset due to the wide bandwidth (>14 THz). The adjacent channel crosstalk is at the 32 dB level, and the self-crosstalk is at the 28 dB level. An important parameter to justify the flatness of the transmission spectrum is the channel aspect ratio. The 1 dB, 3 dB, and 10 dB bandwidth of the center wavelength channel

is measured to be 11.6 nm, 17 nm, and 25 nm, respectively. Thus, the corresponding aspect ratio of the device is 46%.

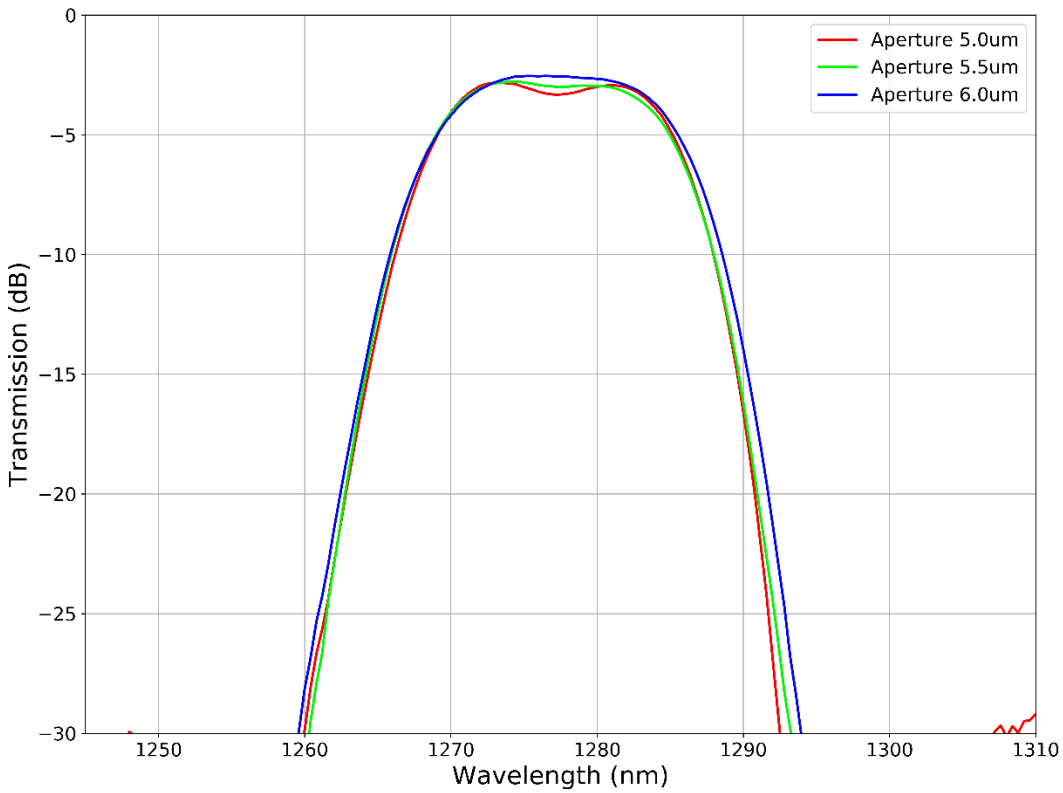

Fig 3. 23 Center channel transmission response with different output waveguide apertures.

We further investigate the influence of the output waveguide aperture on the flatness of the transmission shown in Fig 3. 23. We could see that the output waveguide with a 6.0 μm aperture value demonstrates the best flat-top performance compared to the other two cases. Furthermore, the output waveguide mode profile matches well with the input MMI mode in the wavelength range between 1270 nm and 1281 nm.

We also deliver the 128 channels AWGR with 50 GHz channel spacing (the spectrum shown in Fig 3. 24) as a possible solution for the high-speed switching and communication. The average channel insertion loss is at the 3 dB level. And the intra-channel and inter-channel crosstalk are at

the 20 dB level. Some individual channels experience higher losses resulting due to the defects at device facets.

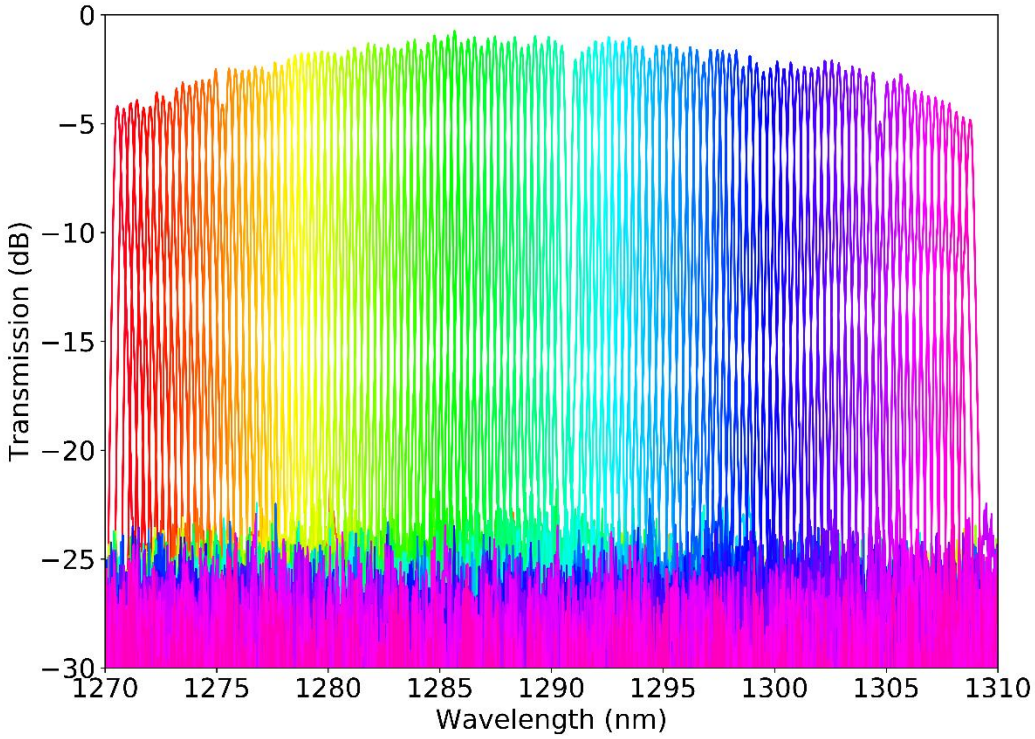

Fig 3. 24 Characterized result of the 128 channel 50 GHz channel spacing AWG Router at 1280 nm center wavelength.

References

[1] C. A. Brackett, "Dense Wavelength Division Multiplexing Networks: Principles and Applications," *IEEE Journal on Selected Areas in Communications*, vol. 8, no. 6, pp. 948–964, 1990, doi: 10.1109/49.57798.

[2] C. Dragone, *Optical multiplexer/demultiplexer*. Google Patents, 1991.

[3] W. Bogaerts, S. Pathak, A. Ruocco, and S. Dwivedi, "Silicon photonics non-resonant wavelength filters: comparison between AWGs, echelle gratings, and cascaded Mach-Zehnder filters," in *Integrated Optics: Devices, Materials, and Technologies XIX*, 2015, vol. 9365, p. 93650H.

[4] M. K. Smit, "New focusing and dispersive planar component based on an optical phased array," *Electronics letters*, vol. 24, no. 7, pp. 385–386, 1988.

[5] C. Dragone, “Efficient N× N star coupler based on Fourier optics,” *Electronics Letters*, vol. 24, no. 15, pp. 942–944, 1988.

[6] H. Takahashi, S. Suzuki, K. Kato, and I. Nishi, “Arrayed-waveguide grating for wavelength division multi/demultiplexer with nanometre resolution,” *Electronics letters*, vol. 26, no. 2, pp. 87–88, 1990.

[7] K. Okamoto, *Fundamentals of optical waveguides*. Academic press, 2006.

[8] M. Zirngibl, C. Dragone, and C. H. Joyner, “Demonstration of a 15* 15 arrayed waveguide multiplexer on InP,” *IEEE Photonics technology letters*, vol. 4, no. 11, pp. 1250–1253, 1992.

[9] C. R. Doerr and K. Okamoto, “Advances in silica planar lightwave circuits,” *Journal of lightwave technology*, vol. 24, no. 12, pp. 4763–4789, 2006.

[10] S. Pathak, D. van Thourhout, and W. Bogaerts, “Design trade-offs for silicon-on-insulator-based AWGs for (de) multiplexer applications,” *Optics letters*, vol. 38, no. 16, pp. 2961–2964, 2013.

[11] S. T. S. Cheung, B. Guan, S. S. Djordjevic, K. Okamoto, and S. J. B. Yoo, “Low-loss and high contrast silicon-on-insulator (SOI) arrayed waveguide grating,” in *CLEO: science and innovations*, 2012, p. CM4A. 5.

[12] A. Malik *et al.*, “Germanium-on-silicon mid-infrared arrayed waveguide grating multiplexers,” *IEEE Photonics Technology Letters*, vol. 25, no. 18, pp. 1805–1808, 2013.

[13] H. Takahashi, Y. Hibino, and I. Nishi, “Polarization-insensitive arrayed-waveguide grating wavelength multiplexer on silicon,” *Optics letters*, vol. 17, no. 7, pp. 499–501, 1992.

[14] K. Kodate and Y. Komai, “Compact spectroscopic sensor using an arrayed waveguide grating,” *Journal of Optics A: Pure and Applied Optics*, vol. 10, no. 4, p. 44011, 2008.

[15] T. Kurokawa *et al.*, “Time-space-conversion optical signal processing using arrayed-waveguide grating,” *Electronics Letters*, vol. 33, no. 22, pp. 1890–1891, 1997.

[16] K. A. McGreer, “Arrayed waveguide gratings for wavelength routing,” *IEEE Communications Magazine*, vol. 36, no. 12, pp. 62–68, 1998.

[17] A. J. Lowery, “Design of arrayed-waveguide grating routers for use as optical OFDM demultiplexers,” *Optics express*, vol. 18, no. 13, pp. 14129–14143, 2010.

[18] R. Proietti, Z. Cao, C. J. Nitta, Y. Li, and S. J. ben Yoo, “A scalable, low-latency, high-throughput, optical interconnect architecture based on arrayed waveguide grating routers,” *Journal of Lightwave Technology*, vol. 33, no. 4, pp. 911–920, 2015.

[19] S. Pathak, “Silicon nano-photonics based arrayed waveguide gratings,” Ghent University, 2014.

[20] Pathak, Shibnath, “Silicon nano-photonics based arrayed waveguide gratings,” Ghent University. Faculty of Engineering and Architecture, 2014.

[21] Y. Chu, X. Zheng, H. Zhang, X. Liu, and Y. Guo, “The impact of phase errors on arrayed waveguide gratings,” *IEEE Journal of selected topics in quantum electronics*, vol. 8, no. 6, pp. 1122–1129, 2002.

[22] E. Kleijn, M. K. Smit, and X. J. M. Leijtens, “New analytical arrayed waveguide grating model,” *Journal of lightwave technology*, vol. 31, no. 20, pp. 3309–3314, 2013.

[23] A. Klekamp and R. Münzner, “Imaging errors in arrayed waveguide gratings,” *Optical and quantum electronics*, vol. 35, no. 4, pp. 333–345, 2003.

[24] P. Munoz, D. Pastor, and J. Capmany, “Modeling and design of arrayed waveguide gratings,” *Journal of lightwave technology*, vol. 20, no. 4, p. 661, 2002.

[25] O.-U. Guide, “RSOFT Design Group,” *Inc*, 2010.

[26] W. Bogaerts, M. Fiers, M. Sivilotti, and P. Dumon, “The IPKISS photonic design framework,” in *Optical Fiber Communication Conference*, 2016, pp. W1E--1.

[27] K. Okamoto and A. Sugita, “Flat spectral response arrayed-waveguide grating multiplexer with parabolic waveguide horns,” *Electronics letters*, vol. 32, no. 18, p. 1661, 1996.

[28] M. R. Amersfoort, J. B. D. Soole, H. P. LeBlanc, N. C. Andreadakis, A. Rajhel, and C. Caneau, “Passband broadening of integrated arrayed waveguide filters using multimode interference couplers,” *Electronics letters*, vol. 32, no. 5, p. 449, 1996.

[29] S. Pathak, M. Vanslembrouck, P. Dumon, D. van Thourhout, and W. Bogaerts, “Optimized silicon AWG with flattened spectral response using an MMI aperture,” *Journal of Lightwave Technology*, vol. 31, no. 1, pp. 87–93, 2013.

[30] D. K. Gifford, B. J. Soller, M. S. Wolfe, and M. E. Froggatt, “Optical vector network analyzer for single-scan measurements of loss, group delay, and polarization mode dispersion,” *Applied optics*, vol. 44, no. 34, pp. 7282–7286, 2005.

Chapter 4 SPIDER New Generation PICs

4.1 System Overview and Interferometric Imaging

Traditional optical telescopes collect light from a scene and map the received photon to the image plane, further analyzed by an array of detectors at the focal plane. The size, weight and power (*SWaP*) value of traditional telescopes is determined by the bulky optical components and the supporting electronic driving circuits. The longitudinal system length *L* for conventional telescopes scales linearly with the optical aperture diameter *D*, resulting in the considerable system size. We propose the Segmented Planar Imaging Detector for Electro-optical Reconnaissance (SPIDER) concept [1]–[7] based on interferometric imaging theory [8], [9] shown Fig 4. 1 as an alternative to reduce the *SWaP* value of the system by at least an order of magnitude for a given spatial resolution. This SPIDER imager will provide comparable image resolution to the conventional telescope with the minimized system mass and volume. The SPIDER system replaces the traditional bulky optical telescope and focal plane detector arrays with CMOS-nanofabrication-compatible Photonic Integrated Circuits (PICs) composed of several identical 1D interferometers arrays arranged in a radial-spoke pattern shown as the "Image Modules" in Fig 4. 1. The "Shutter Assembly" controls the electronic shutter in a timely manner to pass the object light. The following "Array Housing" components mechanically hold the lenslets paired to the radially placed PICs sitting in the "Image Modules". Specifically, the "Image Module" is shown in Fig 4. 1.(b) in detail. The lenslets are placed to form different interferometric baselines at the inputs of each PIC. Object light will couple through lenslets with maximum coupling ratio into the on-chip path-length-matched waveguides. Then light rays will propagate through AWG-based Demux to be divided into 18 different wavelength channels. In the end, light rays coming through same baselines and

the same wavelength channel will constructively interfere at the end of multimode interferometers (MMIs), generating complex visibility functions at linear detector arrays. The received light visibility function will be digitized and reproduced to retrieve the object image. In this way, light from different baselines can be processed within a single PIC, forming a 1D interferometer array. Several of these 1D arrays are arranged radially to form 2D arrays. The spatial coherent measurement of the complex visibility function at the linear detector arrays is equivalent to a sample of the object's 2D Fourier transform through the Van Cittert-Zernike theorem [10], [11].

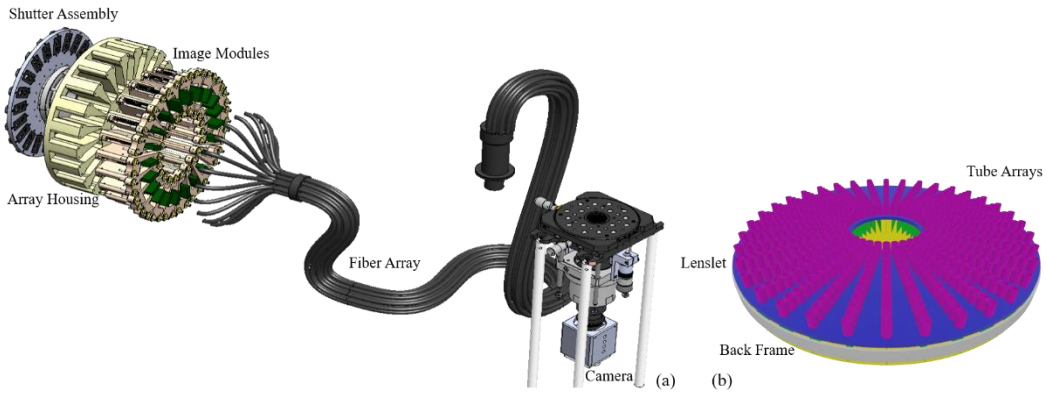

Fig 4. 1 (a) A diagram of the SPIDER system; (b) The zoom-in design of the "Image Module".

Fig 4. 2 further expands our proposed image module into different components in a top-down view. The module consists of various 1D interferometers arrays arranged in the radial pattern. Many interferometer tube assemblies (shown in purple) at the top help to couple light into the PICs waveguides. A lenslet array plate (shown in blue) is designed accordingly to hold interferometer tube assemblies firmly. Then various PICs (shown in green) are held in between aligning cylinders to fulfill the spatial resolution. All above components sit on a stiff back frame (shown in yellow), containing readout and Digital Signal Processing (DSP) electronics. The overall module form factor is comparable to a flat-screen TV or a solar panel. The spatial resolution of the whole system

is determined by the maximum interferometer baseline distance (*B*) in an individual PIC. It is comparable to the conventional imager having the aperture diameter approximately equal to this maximum baseline distance.

Fig 4. 2.(b) presents the fundamental interferometric imaging theory under the one-baseline condition. The whole system consists of a distant light source, a pair of lenslets, a couple of receiving apertures separated by a certain baseline distance (*B*), two tunable delay lines, and the balanced detectors. The combined light field at balanced detectors is:

$$A\{\exp(ik[\vec{L}.\vec{B}+\vec{D}_1])+\exp(ik[\vec{D}_2])\}\exp(-i\omega t) \tag{4.1}$$

And the time-averaged intensity controlled by delay lines is further calculated from Eq.(4.1):

$$I \propto 2+2\cos(k[\vec{L}.\vec{B}+\vec{D}_1-\vec{D}_2]) \tag{4.2}$$

The visibility function is defined as:

$$abs(V)=\frac{I_{max}-I_{min}}{I_{max}+I_{min}} \tag{4.3}$$

Where $\vec{L}$ denotes distance between the light source to the baseline, $\vec{B}$ represents the baseline value, $\vec{D}_1$ denotes the length of the delay line 1, $\vec{D}_2$ denotes the length of the delay line 1, and V represents the visibility function. The Van Cittert-Zernike theorem states that the visibility function represents the Spatial Fourier Transform of the object. Thus, we could obtain the corresponding visibility function at various baseline values with different light frequencies. Finally, we could reconstruct the 2D object image performing the inverse Spatial Fourier Transform on visibility functions we captured on the *u*-*v* plane.

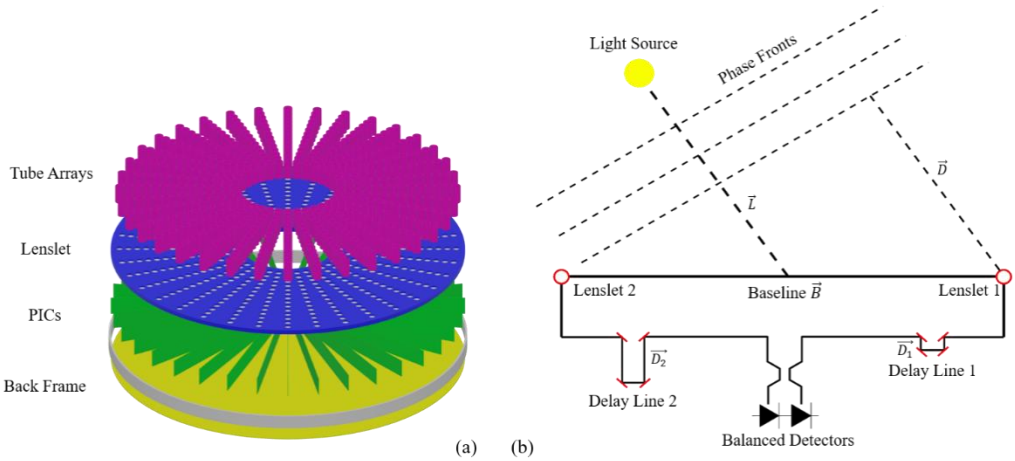

Fig 4. 2 (a) SPIDER imaging module (exploded view); (b) A one-baseline Interferometric imaging system illustration.

The resolution of the SPIDER system is determined by the maximum baseline distance B_{max} and the imaging light wavelength λ. The maximum spatial frequency of the visibility function defined in Eq.(4.3) is calculated as $u_{cutoff} = B_{max}/\lambda_{min}$, where λ_{min} is the shortest light wavelength used in the imaging system. Thus, when the maximum baseline value of the system is similar to the diameter of the conventional imager aperture, the resolution of the SPIDER system is comparable to such imager. We also guarantee our dense Fourier sampling rate is close to the Nyquist rate to realize the maximum resolution.

4.2 SPIDER Si_3N_4 PICs Design

4.2.1 PICs and baselines overviews

Fig 4. 3 illustrates photonic components within a single PIC of the SPIDER system with lenslets in front, including path-length-matching waveguides, interferometers (MMIs), AWGs based Demuxs, and detector arrays.

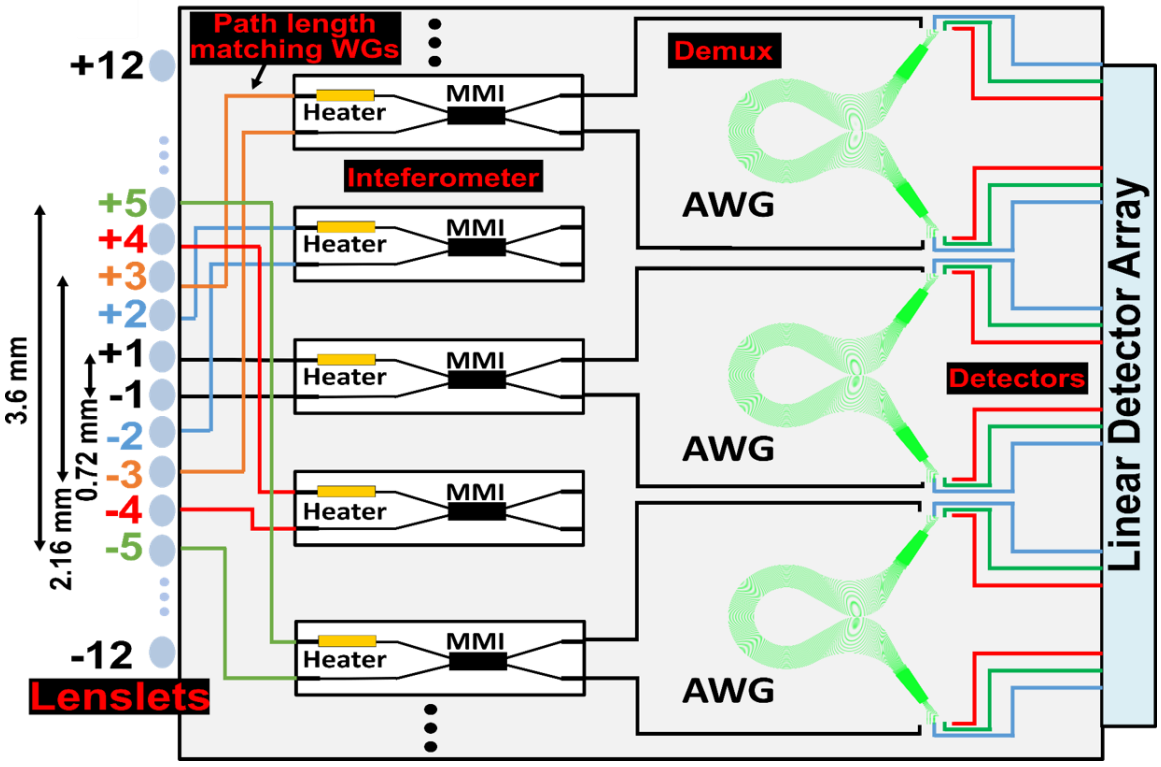

Fig 4. 3 PIC overview with a sketch of path-length-matching waveguides, demultiplexer, Multimode Interferometer, and Detectors.

The light is coupled from the free space to path-length-matching waveguides on the chip through various lenslets marked from -12 to +12 in pairs on the left-hand side of Fig 4. 3. In this PIC design, we include 12 baselines illustrated by 12 different numbers where the minimum baseline distance is 0.72 mm. The rest 11 baselines' distances are integer number times of the minimum baseline distance, i.e., the No.2 baseline distance is 1.44 mm and the No.3 baseline distance is 2.16 mm, shown in Fig 4. 4. We use Si_3N_4/SiO_2 waveguides with the 150 nm-thick Si_3N_4 as the waveguide core providing around *30%* refractive index difference percentage ($\Delta n\%$), which is orders of magnitude higher than the silica waveguide platform. This Si_3N_4 based high index contrast waveguide platform could further minimize the PIC size and the power consumption while maintaining the optical loss margin compared to the silica waveguide platform. When light couples

into this Si_3N_4 PIC, it travels through a section of path-length-matching waveguides starting from the corresponding baselines to maintain the in-phase condition and the spatial coherence between two receiving apertures. These path-length-matching waveguides are marked with different colors for different baseline values in Fig 4. 3. We encounter unavoidable waveguide crossings when routing all 12 baselines. Thus, we develop the multilayer coupling technology within the Si_3N_4 platform employing a thinner 50 nm-thick Si_3N_4 layer as a transition layer. The relevant Si_3N_4 waveguide platform designs with simulations of waveguide mode, mode size, mode refractive index, and bending loss are presented in the following sections. After paired lenslets, the light rays passing through baseline waveguides recombine at a heater-assisted MMI section to generate visibility interference fringes. In this specific PIC design, we move the interferometer section ahead of the Demux to decrease the number of interferometers for each baseline from 18 to 1 (we have a total 18 wavelength channels to meet the Nyquist sampling rate). The MMI structure has a broadband interference capability comparing to the directional-coupler alternative covering the entire 1200 nm ~ 1600 nm wavelength range utilized in the system. We will perform BPM simulations for MMI structures covering the desired wavelength band. The interfered light rays coming out of the MMIs are demultiplexed through AWG Demuxs into 18 different wavelength channels covering the complete wavelength range. We use the AWG Demux to achieve the desired demultiplexing capability since it not only has excellent wavelength filtering performance but also utilizes both star couplers as Demux outputs, cutting down the number of AWGs needed by a factor of two. As discussed in the previous chapter, the length of waveguides in arrayed arms of AWGs increases linearly to introduce a linear optical phase shift. This induced phase shift in arrayed waveguides varies with the wavelength due to the wavelength dependence of the propagation constant. This phase delay of different wavelength channels will induce the phase tilt

at the output star-coupler. Thus, different wavelength channels will constructively interfere with the output mode profile at different angular locations at the output star-coupler. Phase errors generated alongside the propagation through AWGs should be mitigated to reduce intra-crosstalk and inter-crosstalk levels. Lights coming out of the same wavelength channel but from different star-couplers in one AWG are guided towards to end of the PIC shown in different waveguide colors (red, green, and blue) in Fig 4. 3. Paired wavelength channels are further directed towards a balanced coherent detection system to retrieve the complex visibility information. Linear detector arrays are connected to the end of the PIC to digitize both the amplitude and phase of complex visibility fringes. We perform DSP to mitigate the extra noise generated within the whole system and retrieve the original object image.

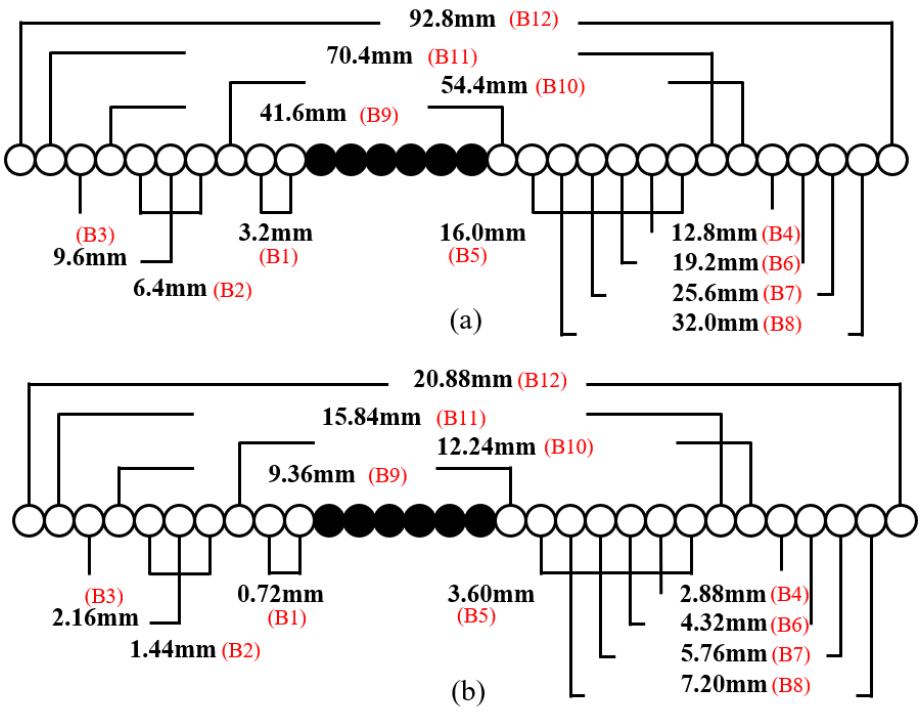

Fig 4. 4 (a) The low-resolution PIC baseline arrangement; (b) The high-resolution PIC baseline arrangement.

Fig 4. 4 presents the front view of PICs' baselines configurations (lenslets locations show in Fig 4. 3). We include total 12 baselines in the PIC design marked with red numbers. In the low-resolution case (shown in Fig 4. 4.(a)), the shortest baseline distance is 0.72 mm while the longest baseline distance is 20.88 mm. Lengths of intermediate baselines are integer number times of the shortest baseline distance. Twelve baselines together with the complete wavelength range could be further mapped to the *u*-*v* spatial frequency domain to sample the received image. We place 12 different baselines in such sequence to minimize the number of waveguide crossings needed in the PIC. Having 20.88 mm as the longest baseline distance in the low-resolution PIC, we could successfully fabricate the chip utilizing the 248 nm projection lithography technology in our cleanroom. And we also include a high-resolution baseline PIC design shown in Fig 4. 4.(b) where the corresponding baseline distance is four times of that in the low-resolution PIC.

This increased baseline distance could help to enhance the resolution of the image by a factor of four. Because we design the longest baseline distance in the high-resolution PIC to be 92.88 mm (close to the diameter of a four-inch wafer), we have to use contact lithography on a six-inch wafer to achieve this layout. The most minor feature resolved by our current contact aligner is around 1 μm, four times larger than the minimum feature generated by the projection lithography. This mismatch could introduce lateral misalignments and the extra coupling loss.

Fig 4. 5 presents the radial spatial frequency mapping of both low-resolution and high-resolution baseline configurations. The radial spatial frequency relates to the functioning wavelength and the baseline distance in the following relationship:

$$u = \vec{B}/\lambda \tag{4.4}$$

Where B denotes the baseline distance, and λ indicates the functioning wavelength. 12 baselines provide the radial sampling frequency continuously. The high-resolution PIC baselines could provide the radial spatial frequency from 0 to approximately 80 *cycles/mrad*. In comparison, a low-resolution PIC could only offer the sampling frequency from 0 to 18 *cycles/mrad*. This difference in the maximum sampling frequency leads to the resolution contrast in the factor of four. We could alternatively arrange low-resolution and high-resolution PICs in the radial pattern to maximize the frequency sampling capability of the entire system to realize the best tradeoff between the size and the resolution.

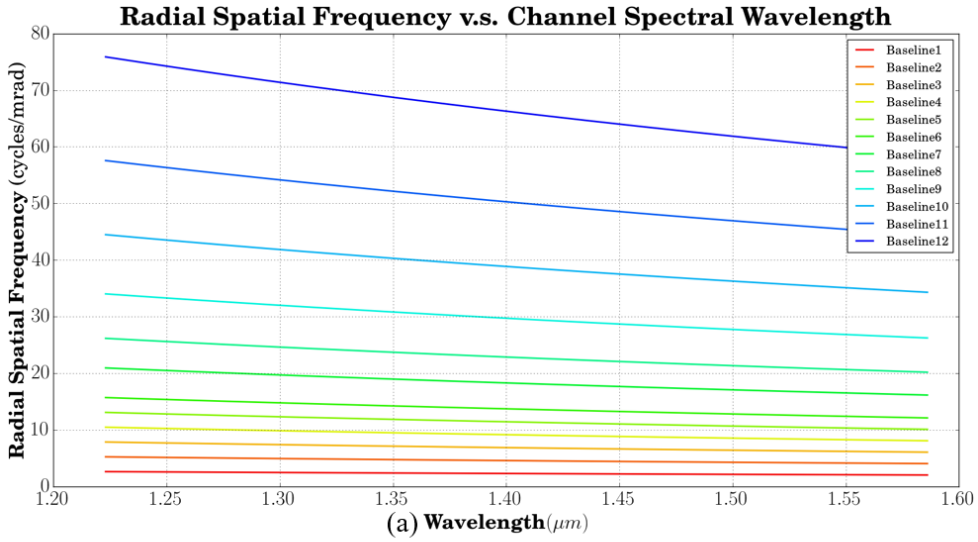

Fig 4. 5 Equivalent *u-v* spatial frequency domain mapping of (a) high-resolution PIC baselines; (b) low-resolution PIC baselines.

4.2.2 Multilayer Si_3N_4 Waveguide Platform

We use the 150 nm-thick Si_3N_4 waveguides platform for functional devices to decrease the *SWaP* value of the entire system and the 50 nm-thick Si_3N_4 waveguides platform for layer-to-layer transitions. This section starts with the Si_3N_4 waveguide mode simulation of the multi-layer Si_3N_4 platform to overcome the waveguide crossing problems. Then we define the single-mode waveguide core width for both 50 nm-thick and 150 nm-thick Si_3N_4 waveguides. We will also perform the mode effective index simulation with respect to the waveguide core width, facilitating designs of MMIs and AWGs. Finally, we present the waveguide bending loss simulation to choose the minimum bending radius for the multi-layer platform.

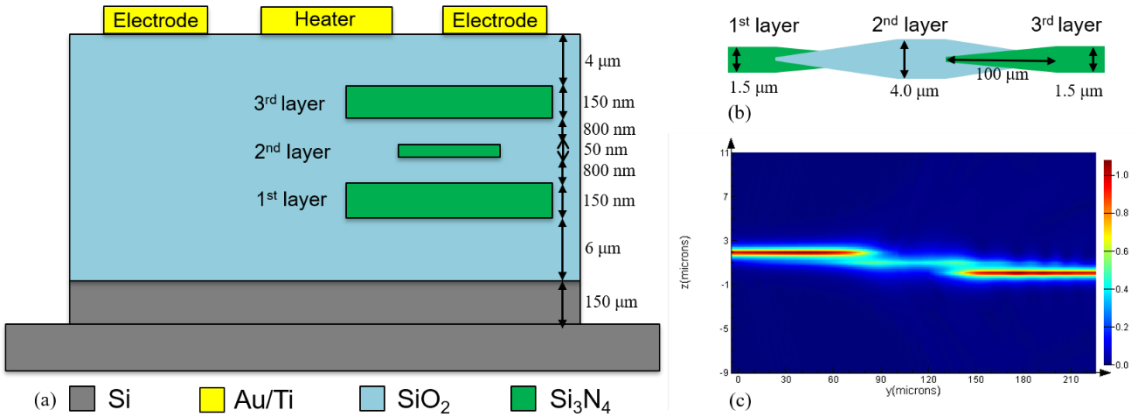

Fig 4. 6 (a) Multi-layer Si_3N_4 waveguide platform cross-section view; (b) Three-layer vertical transition couplers in the top-down view; (c) Power transmission simulation of the three-layer vertical couplers in the cross-section view.

Fig 4. 6.(a) illustrates the cross-section view of the three-layer Si_3N_4 waveguides platform [12]–[14] developed for the SPIDER system. The platform starts with a 6 µm-thick SiO_2 bottom layer

as the waveguide sub-cladding, thick enough to avoid the power leakage into the Silicon substrate. The 1st layer is a 150 nm-thick Si_3N_4 waveguide layer containing necessary functional devices (i.e., AWGs, MMIs, path-length-matching waveguides). It also contains the three-layer vertical coupler section shown in Fig 4. 6.(b). The 2nd layer, the 50 nm-thick Si_3N_4 waveguide layer, acts only as the transition layer between the top and bottom waveguide layers to avoid the waveguide crossing loss. These three-layer vertical couplers consist of top and bottom waveguides tapered down to 250 nm in width with an adiabatic 100 μm-long taper section. The 50 nm-thick Si_3N_4 waveguide layer stays in the middle layer utilizing the overlapped vertical tapers to propagate the optical power. The simulated power transmission from the top to the bottom waveguide layer is shown in Fig 4. 6.(c). We could achieve below 0.1 dB loss for this three-layer transition. We keep the SiO_2 layer between waveguide layers to be approximately 800 nm, balancing the tradeoff between the vertical coupling loss and the device thickness. Finally, we use a 4 μm-thick SiO_2 layer as the waveguide top-cladding and Au/Ti heater/electrodes to control the baseline phase difference.

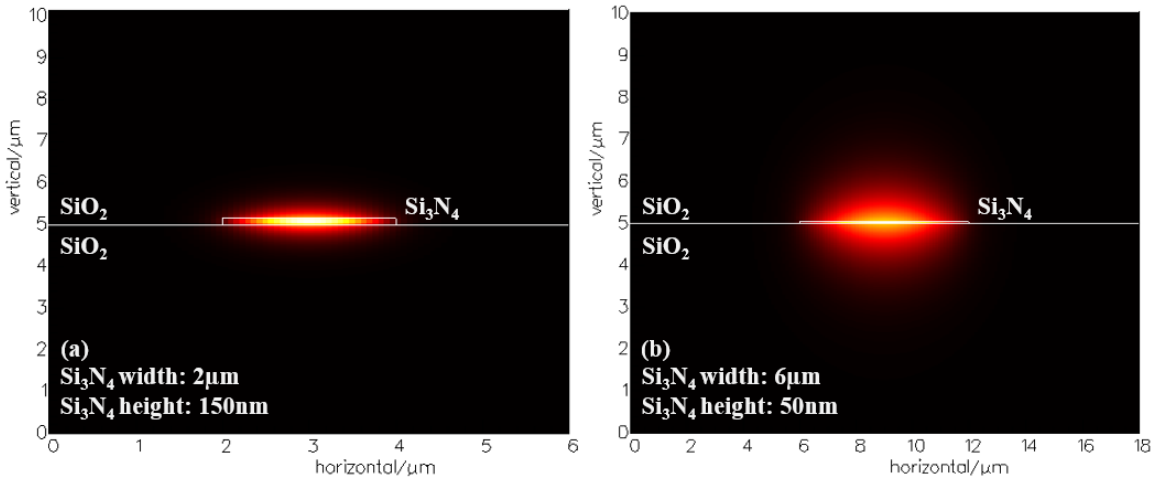

Fig 4. 7 Mode simulation results at 1550 nm center wavelength for (a) 50 nm × 6 μm Si_3N_4 single-mode waveguides; (b) 150 nm × 2 μm Si_3N_4 single-mode waveguides.

Fig 4. 7 shows the simulated mode profile of single-mode 50 nm-thick Si_3N_4 and 150 nm-thick Si_3N_4 waveguides. We use the Film Mode Matching (FMM) algorithm [15] to calculate the first-order TE mode with the high accuracy numerically. The 150 nm-thick Si_3N_4 waveguide mode on the left-hand side has a smaller mode size compared to the 50 nm-thick Si_3N_4 waveguide on the right-hand side. Thus, we choose to use the 150 nm-thick Si_3N_4 waveguide platform for functional devices (path-length-matching waveguides, AWGs, MMIs) and the 50-nm thick Si_3N_4 waveguide for layer-to-layer couplers. The large mode size in the 50-nm thick Si_3N_4 waveguide platform helps to increase the vertical coupling coefficient.

We also run the sweep simulation of the mode size (both lateral and vertical) with respect to the waveguide core (Si_3N_4) width to justify the best waveguide configuration for the layer-to-layer coupling and the end-facet coupling shown in Fig 4. 6.(b). Referring to the mode effective index simulation result (Fig 4. 8), we choose the single-mode waveguide core width for 50 nm-thick Si_3N_4 and 150 nm-thick Si_3N_4 waveguides to be 6 μm and 2 μm, respectively. The mode size of both waveguides tends to increase when the core width decreases. Therefore, we design adiabatic negative tapers for the end-facet coupling based on this result to maximize the 150 nm-thick Si_3N_4 waveguide mode power coupling to the standard lens-fiber mode (mode spot size: 2.5 μm or 5 μm in diameter). We also employ such adiabatic taper designs in three-layer vertical couplers to maximize the coupling ratio with geometric details shown in Fig 4. 6.(b).

Fig 4. 8 illustrates the effective index simulation of both 50 nm-thick Si_3N_4 waveguides and 150 nm-thick Si_3N_4 waveguides. The effective index of the first-order mode increases as the core width increases, which matches well with the analytical anticipation. We simulate the 90° bending loss of both 150 nm and 50 nm Si_3N_4 waveguides for future MMI and AWGs designs. We perform the 90° bending loss simulation of the 150 nm × 2 μm Si_3N_4 waveguide and the 50 nm × 6 μm Si_3N_4

waveguide presented in Fig 4. 9. The bending loss drops below 0.01 dB at approximately 150 µm bending radius for the 150 nm × 2 µm Si_3N_4 waveguide. We choose to use 200 µm minimum bending radius in the practical design based on the zoom-in simulation in Fig 4. 9.(a). Following the same reasoning, we choose to use 3 mm minimum bending radius for the 50 nm × 6 µm Si_3N_4 waveguide presented in Fig 4. 9.(b)

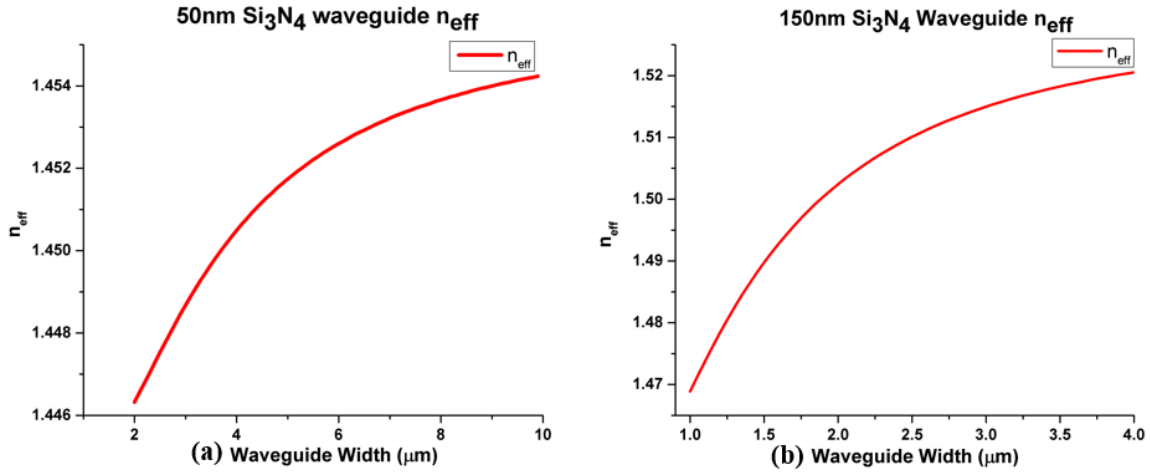

Fig 4. 8 (a) 50 nm-thick Si_3N_4 waveguide effective index simulation with respect to waveguide core width; (b) 150 nm-thick Si_3N_4 waveguide effective index simulation with respect to waveguide core width.

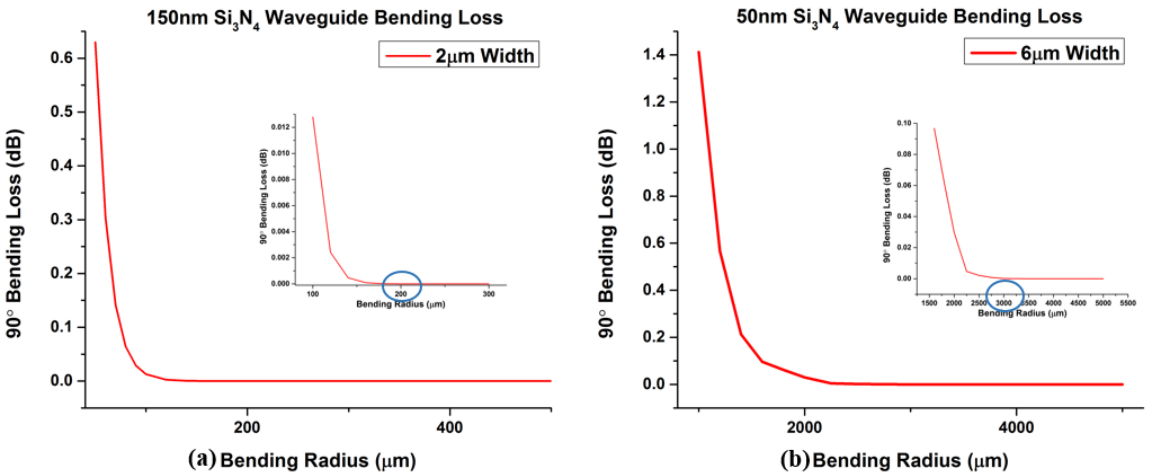

Fig 4. 9 (a) 150 nm × 2 µm Si_3N_4 waveguide bending loss simulation with respect to bending radius; (b) 50 nm × 6 µm Si_3N_4 waveguide bending loss simulation with respect to bending radius.

4.2.3 MMIs and AWGs

There are multiple coupling and routing devices suitable for the interferometric imaging process, including MMIs, directional couplers, adiabatic "X" junctions, and diffractive star couplers. MMI is superior to the rest of devices in its broadband performance while maintaining a constant power coupling ratio simultaneously. Since we use the imaging light wavelength from 1200 nm to 1600 nm, we decide to use MMIs to fulfill our need for broadband interferometers. The operation of optical MMI devices is based on the self-imaging principle [16], [17]. Self-imaging is a property of multimode waveguides by which an input mode profile is reproduced in multiple images at periodic intervals along the direction of the waveguide. As shown in Fig 4. 10.(a), the center of the MMI structure is a wide multi-mode waveguide section designed to support various optical modes (typically > 3). In our 2 × 2 interferometer case, we place two input waveguides symmetrically to the center plane of the MMI structure to excite the optical mode into the multimode section. And we also mount two output waveguides symmetrically to collect optical power out of the multimode region. Through a guided-mode propagation analysis (MPA), we could conclude several equations below to explain mode interactions inside the multimode waveguide region. MPA is a 2D (finite-element or finite-difference method) cross-section calculation which is a simplification and approximation of the practical 3D mode propagation. But MPA method is still accurate under this simple step-index, box-shape mode propagation situation by obtaining the effective refractive index information from 3D structures employing effective index method (EIM).

In Fig 4. 10.(a), we denote the functioning wavelength to be λ, the effective multimode waveguide width W_{ev} is approximately the geometric waveguide width W under the assumption that we are using comparatively high-index-contrast waveguide, the effective index of the multimode

waveguide for the functioning wavelength λ is n_{eff}, and the mode number is υ. The propagation constant of individual mode inside the multimode region β_υ could be calculated as:

$$\beta_\upsilon \approx kn_{eff} - \frac{(\upsilon+1)^2 \pi\lambda_0}{4n_{eff}W^2} \tag{4.5}$$

Where k is the propagation constant of the light with wavelength λ in a relationship $k = 2\pi/\lambda$. From Eq.(4.5) we discover a nearly quadratic dependence of the propagation constant in the multimode region with respect to the mode number υ. We could further define a characteristic length (L_π) of MMIs as the beat length of the two lowest-order modes in the multimode region:

$$L_\pi = \frac{\pi}{\beta_0 - \beta_1} \approx \frac{4n_{eff}W^2}{3\lambda} \tag{4.6}$$

And the propagation constant spacing could be written as:

$$(\beta_0 - \beta_\upsilon) \approx \frac{\upsilon(\upsilon+2)\pi}{3L_\pi} \tag{4.7}$$

We decompose the input waveguide mode as $\Phi(y,0) = \sum_\upsilon c_\upsilon \varphi_\upsilon(y)$ by calculating the amplitude coefficient of each multimode waveguide mode (c_υ) through the overlap integral between the input mode and this exact mode ($\varphi_\upsilon(y)$). After propagating through the multimode waveguide length L, the field of the output mode could be written as below by taking the phase of the fundamental mode as a common factor out of the sum and dropping the time dependence term for the future calculation:

$$\Phi(y,L) = \sum_{\upsilon=0}^{m-1} c_\upsilon \varphi_\upsilon(y) \exp[j\frac{\upsilon(\upsilon+2)\pi}{3L_\pi}L] \tag{4.8}$$

When we place input waveguides at specific positions ($s = \pm \frac{1}{6} W$), some orders of modes ($\upsilon = 2,5,8\cdots$) do not excite inside the multimode region. Thus, the two-fold image formation distance could be summarized as:

$$L = \frac{p}{2}(L_\pi) \tag{4.9}$$

Where p ($p \geq 0$) denotes the number of periods of images along the multimode waveguide length. Thus, combining Eq.(4.6) and Eq.(4.9), we could design MMI structures (an example shown in Fig 4. 10.(a)) at the specific wavelength.

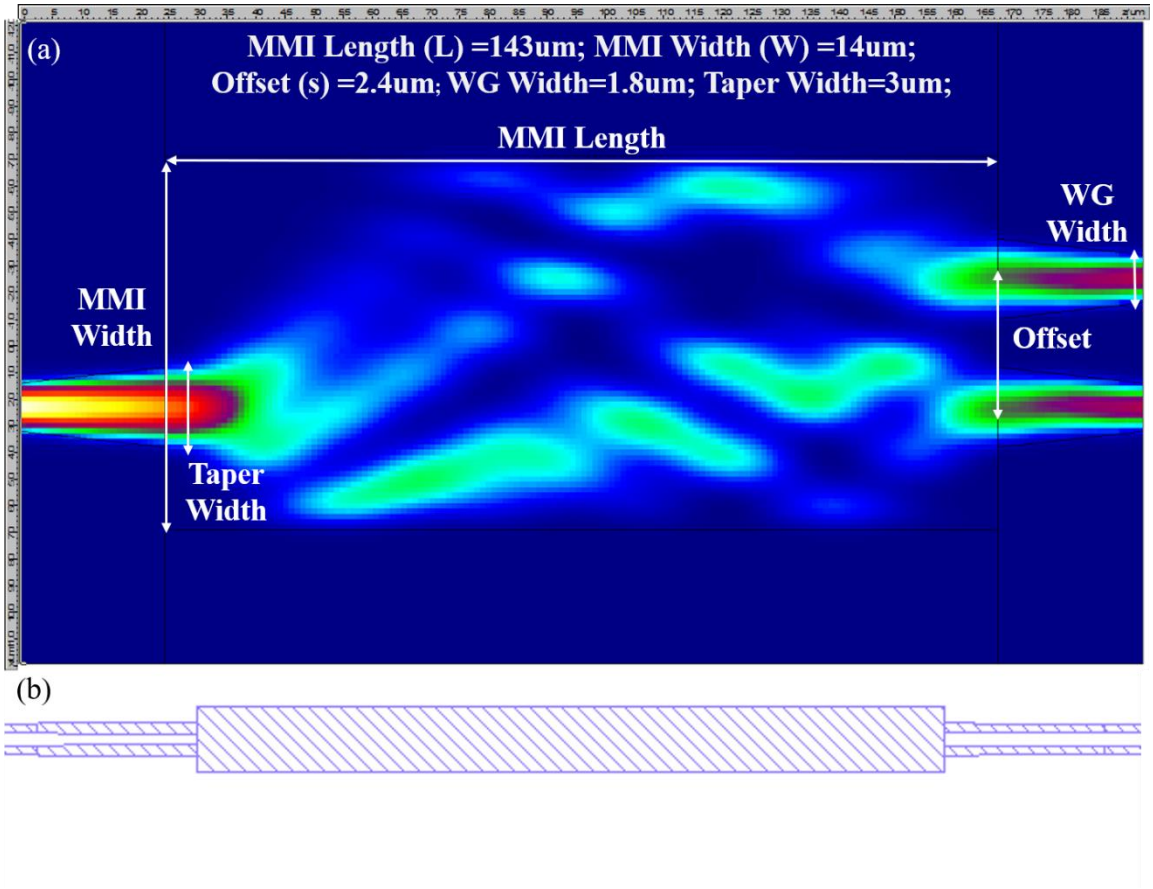

Fig 4. 10 (a) 1533 nm MMI power simulation result with geometric values; (b) The MM layout.

We present a design example of the MMI structure in Fig 4. 10.(a) at the 1533 nm functioning wavelength to fulfill the need for the balanced interference in the proposed wide wavelength range (1220 nm~1590 nm). Fig 4. 10.(a) shows the simulation setup and the corresponding power transmission result of this MMI structure. The depicted MMI is designed for equal power splitting at the 1533 nm wavelength (the detailed structure parameters are listed inside the picture). We set the multimode waveguide width to be 14 μm, which is wide enough to support over five optical modes. Following Eq.(4.8) and Eq.(4.9), the theoretical waveguide separation should be set to be $s = W/6 = 2.33\mu m$, and the multimode waveguide length should be set to be $L = \frac{2n_{eff}W^2}{3\lambda} = 127.8\mu m$.

We further set up the simulation environment to confirm device parameters utilizing Beam Propagation Method (BPM). Simulated parameters for the practical 50/50 splitting ratio are listed in Fig 4. 10.(a). Differences between the theoretical analysis and the simulation result from the expanded effective multimode waveguide width and the non-ideality induced by Goos–Hänchen shift [18]. After performing several sweep simulations, we could conclude the best design parameters for the equal power splitting with the minimum insertion loss.

Fig 4. 10.(b) illustrates the corresponding mask layout for this equal power splitting 1533 nm MMI structure. Then, we repeat the above simulation steps for all wavelength channels (1223nm~1586nm). The 18 MMIs have the multimode waveguide width ranging from 11.2 μm to 14.5 μm. The rest design parameters (MMI length, waveguide separations) are calculated and simulated accordingly. Specifically, we include a positive taper region before input and output waveguides to reduce the mode coupling loss resulting from the mode mismatch.

We follow the AWG Demux design routine introduced in the previous chapter to deliver the 18 channels 3.3 THz channel spacing AWG Demux shown in Fig 4. 11 with the 2.7 mm × 3 mm

device footprint. We connect three circular routings to achieve the 1.8 μm path length difference on the 150 nm-thick Si_3N_4 waveguide platform. We intentionally use both star-couplers within the same AWG to function as the Demux to cut down the number of AWG needed to a half. Fig 4. 11 shows that we separate the input waveguides into "North Set" and "South Set" utilizing the side-input configuration. All output waveguides are routed towards the end of the PIC. We also design metal heaters before all MMIs to be approximately 200 Ω. Finally, we place 12 designed AWG Demuxs into the PIC to divide entire wavelength channels.

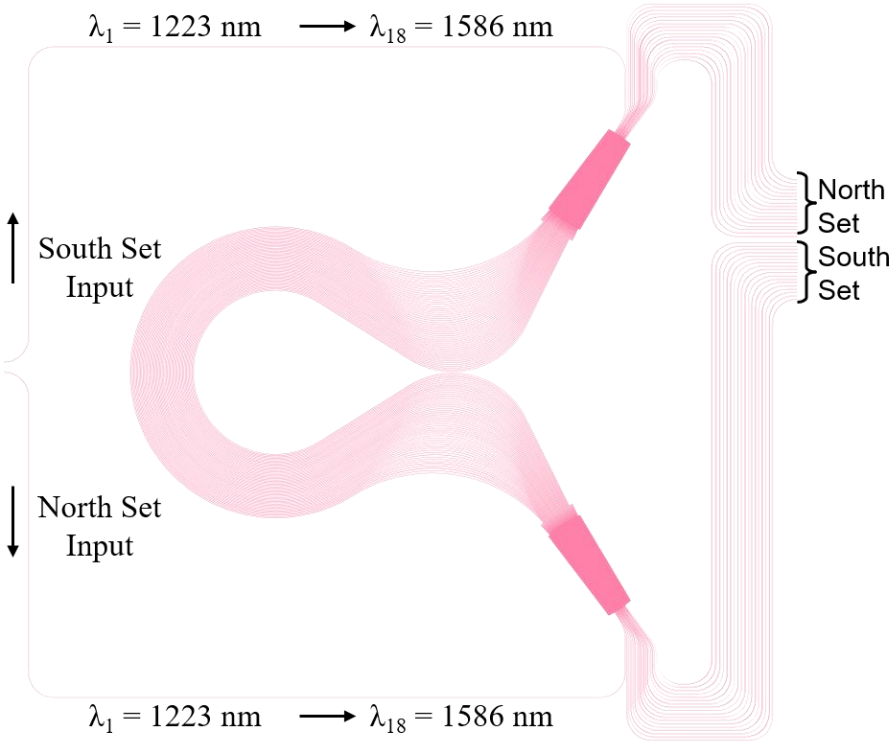

Fig 4. 11 A 18 channels 3.3 THz channel spacing AWG Demux layout.

4.2.4 Final Mask Layout

To facilitate the imaging experiment, we conduct optimizations on the current mask layout shown in Fig 4. 12 and Fig 4. 13.(a). We add additional polishing rulers shown as Fig 4. 12.(a) to help

with the final dicing, lapping, and polishing on the chip facet. The distance between adjacent polishing tooth (*P*) is 20 μm and the length period (*L*) for polishing tooth is 30 μm. Fig 4. 12.(b) and Fig 4. 12.(c) present two additional pass-through waveguides at the top and the bottom of PIC. These two additional guiding waveguides are designed to mitigate the unwanted angular rotation at the experimental imaging stage.

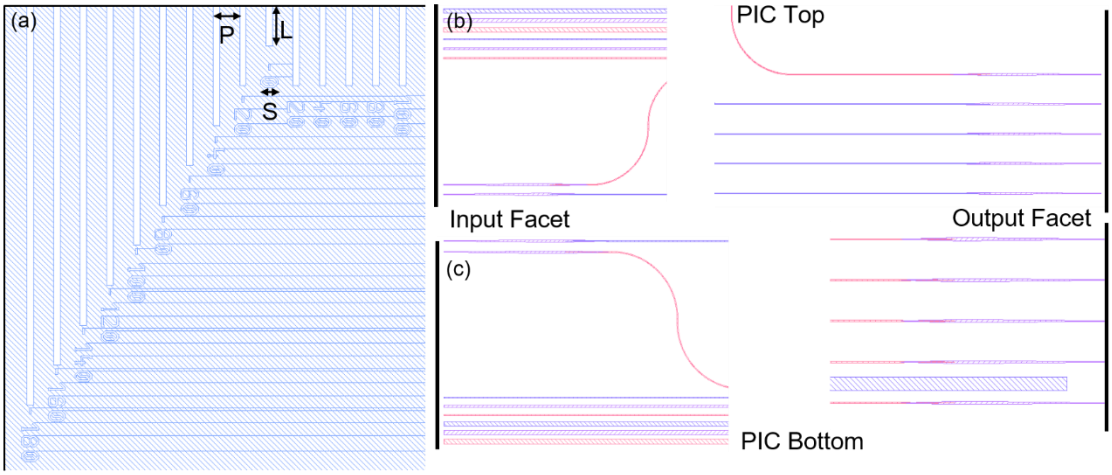

Fig 4. 12 Optimizations on the mask layout: (a) additional polishing rulers on the metal electrode layer; (b) the pass-through waveguide at top of the PIC; (c) the pass-through waveguide at bottom of the PIC.

The entire five-layer mask layouts (shown in five different colors) of the integrated SPIDER PIC, including polishing rulers on the metal layer, top/bottom pass-through waveguides, and all functional devices are shown in Fig 4. 13.(a). The 1st and 3rd waveguide layers are 150 nm-thick Si_3N_4 waveguide layers containing functional components (AWGs, MMIs). The 2nd layer is the 50 nm-thick Si_3N_4 waveguide layer designing for the low-loss and the low-crosstalk interlayer coupling. The 4th layer is the metal heater layer, and the 5th layer is the metal electrode layer. Four polishing rulers are marked as the circle *No.1* with the distance between adjacent polishing tooth to be 20 μm and the length period for polishing tooth to be 30 μm. The top and the bottom pass-

through waveguides are marked as the circle *No.2* on the 1st waveguide layer for the convenience of the angular alignment during imaging experiments.

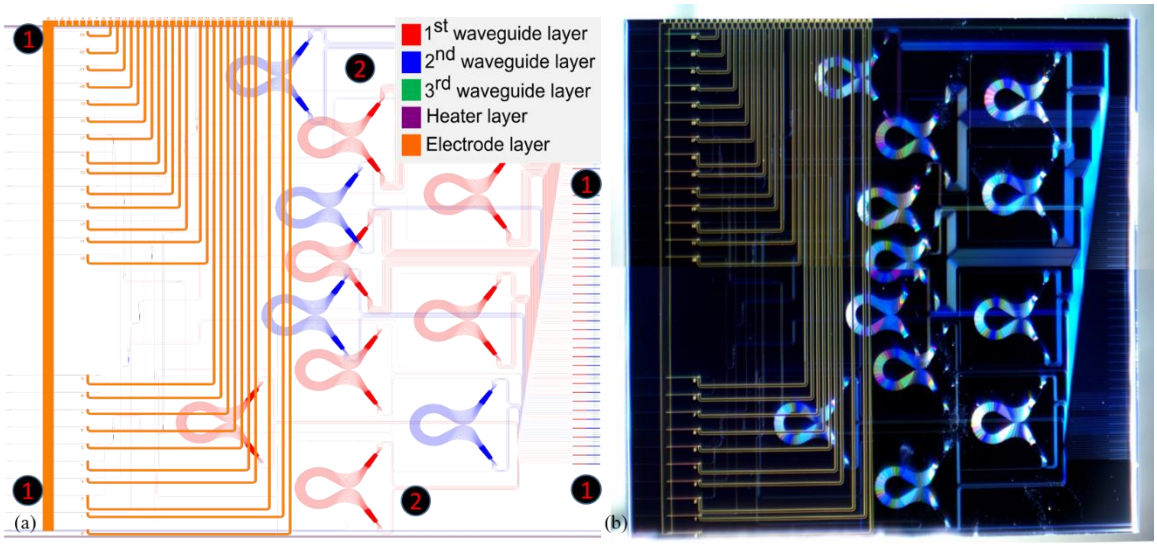

Fig 4. 13 (a) Five-layer overlaid mask layout with polishing rulers and pass-through waveguides at the top and bottom of the PIC. (b) The photo of the fabricated SPIDER PIC on the multilayer Si_3N_4 waveguide platform.

4.3 SPIDER Si_3N_4 PICs Characterization and Experiments

We accomplish the three-layer Si_3N_4 SPIDER PIC following the fabrication process shown in Fig 4. 14. We start the fabrication process with the 6 μm-thick SiO_2 bottom layer deposition on six-inch wafers employing the low-pressure chemical vapor deposition (LPCVD) in step.2). Then we deposit the 1st waveguide layer with the 150 nm-thick Si_3N_4 using LPCVD in step.3). We pattern functional devices on the 1st waveguide layer in step.4) with a-Si hard-mask assisted etching process followed by the interlayer SiO_2 deposition chemical mechanical planarization (CMP) in step.5) and step.6). The CMP process helps us to control the interlayer gap to be approximately 800 nm for the best vertical coupling condition. The surface roughness after the CMP process is measured below 2 nm in the AFM measurement subplot. We repeat the core layer deposition and the cladding layer CMP through step.7) to step.14) to form the 2nd and 3rd waveguide layers. Two

layers of metal heaters (~200 Ω resistance) and electrodes are deposited on the top of the tri-layer stack using the lift-off process. Finally, we perform a deep-etching into the silicon substrate to generate device facets.

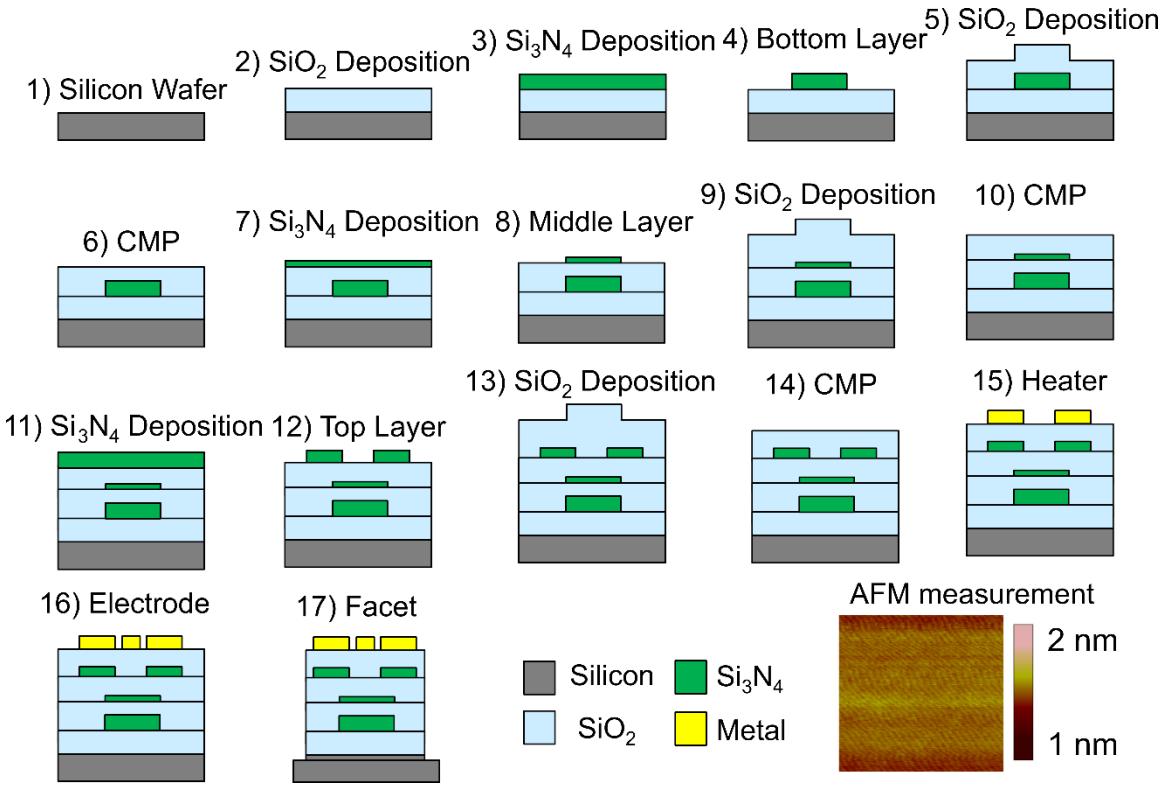

Fig 4. 14 CMOS-compatible SPIDER PIC fabrication process based on the three-layer Si_3N_4 waveguide platform.

Fig 4. 15.(c) presents 21 SPIDER PICs in the 22 mm × 22 mm die size before step.17) in the fabrication process shown in Fig 4. 14. Details of the left-top polish rulers are shown in Fig 4. 15.(b). We take SEM photos for every critical step during the fabrication process, guaranteeing the below 200 nm Si_3N_4 waveguide taper tip presented in Fig 4. 15.(a).

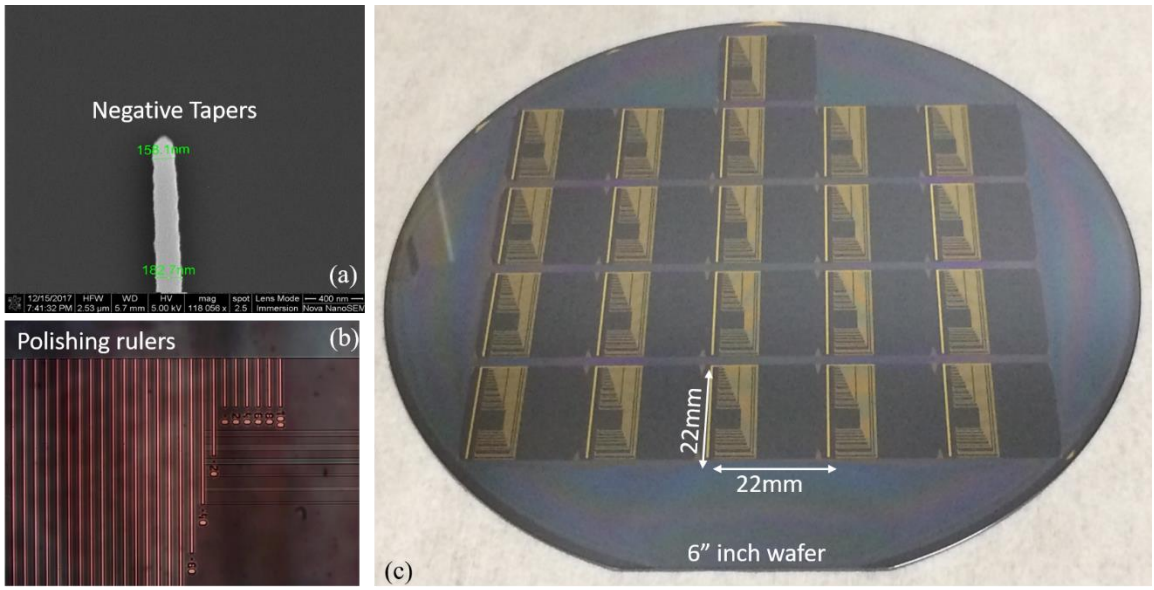

Fig 4. 15 (a) The SEM photo of the negative taper structure within the vertical couplers; (b) The microscope photo of the metal polishing rulers; (c) The fabricated six-inch wafer with SPIDER PIC in 22 mm × 22 mm die size.

Fig 4. 16 presents the photo of the SPIDER PIC transmission characterization and fringe measurement setup, including the input fiber stage (containing TE-polarized input polarization-maintaining (PM) fiber), device-under-test (DUT), DUT holder, and the output fiber stage (containing single mode lens fiber). The light ray coming out of the broadband light source (1000 nm ~ 1600 nm wavelength range) is guided through the polarization beam splitter (PBS) with the help of a polarization controller (PC) to maximize the light power intensity at one output of the PBS. Then this polarized light ray is guided through a specifically tuned PM fiber to maintain the TE polarization towards the PIC. The single-mode lens fiber on the output stage is used and adjusted to collect the transmitted light coming out of the DUT and propagate towards the OSA for data collection. Two input fibers will be used for the point-source fringe measurement. Two probe stations will provide controlled voltages to metal heaters to vary the baseline shift.

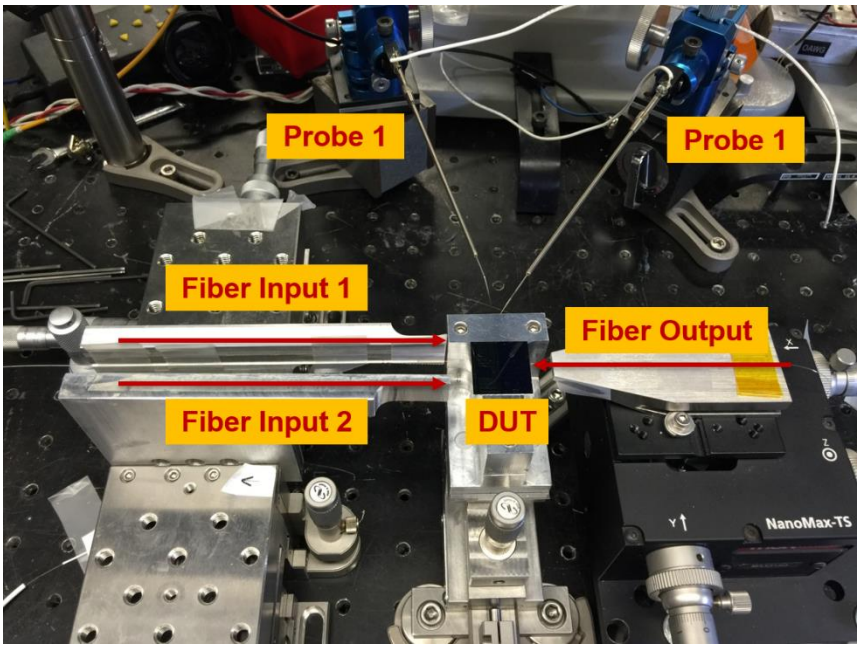

Fig 4. 16 SPIDER PIC optical transmission and fringe measurement setup.

Before characterizing the total transmission performance in the PIC, we examine the output power of the broadband light-source and the two output ports of the PBS. For the characterization of the broadband light source, we directly link the output of the light-source to the optical spectrum analyzer (OSA) and obtain the transmission data shown as "Source" in Fig 4. 17.(a). Then, we connect the PBS to the output of the light source and connect both of PBS outputs to the OSA in sequence. The spectra out of the PBS are shown as "O1" and "O2" in Fig 4. 17.(b). This combined transmission data confirms a ~5 dB optical loss from adding the PC, PBS, and relevant connected fibers. Afterward, we insert the DUT into the measurement setup, as shown in Fig 4. 16, and measure the transmission data of straight-through waveguides at the top and the bottom waveguide layer (1st and 3rd layer). The raw transmission data of straight-through waveguides confirms a dip near 1350 nm wavelength due to the *–OH* bond absorption in the free space and the DUT. This

straight waveguide characterization data will serve as the reference data for the future DUT functional device performance.

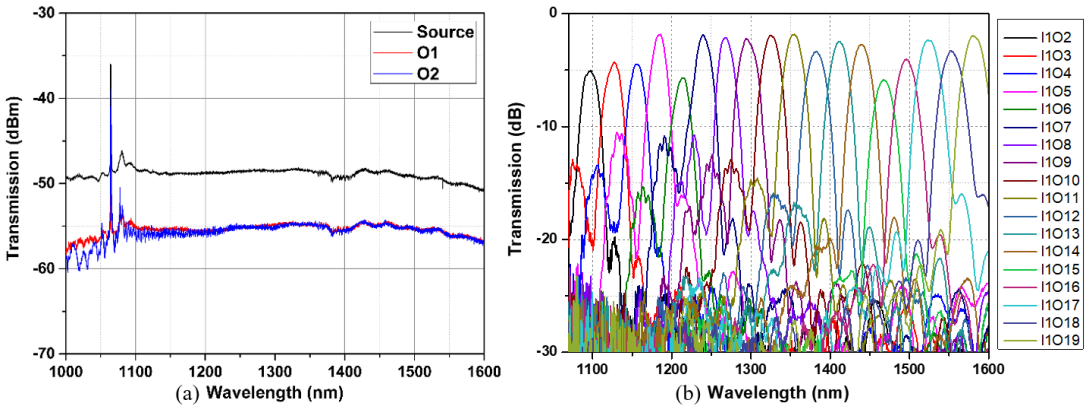

Fig 4. 17 (a) Transmission spectrum of the broadband light source and two output ports of the PBS; (c) Transmission spectrum of the single layer test AWG Demux.

The normalized (to the straight-through waveguide transmission data) transmission spectrum of the AWG on a single 150 nm-thick Si_3N_4 test chip is shown in Fig 4. 17.(b). The average insertion loss is approximately 3 dB, and the channel-to-channel loss variation results from different facet qualities. We experience higher inter-channel crosstalk below 1300 nm wavelength due to the higher-order modes excited in the bending region. We also measure the AWG Demux with ~30 nm channel spacing satisfying the SPIDER system requirements.

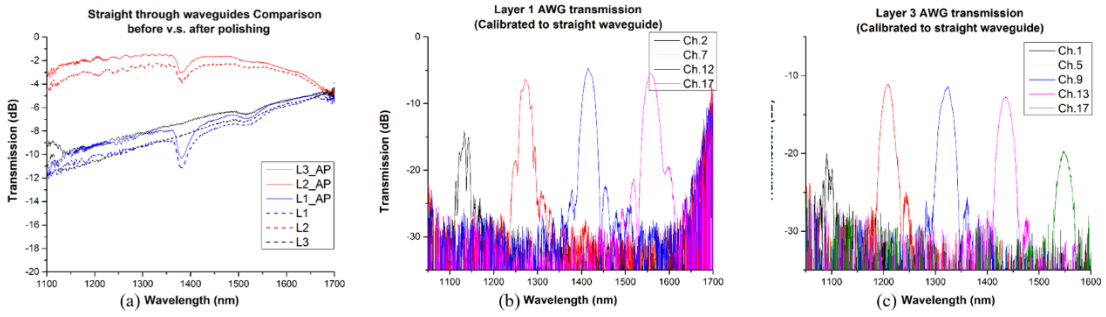

Fig 4. 18 (a) The insertion loss comparison of straight-through waveguides before and after the facet polishing process; (b) SPIDER baseline demultiplexing result on the 1st waveguide layer; (c) SPIDER baseline demultiplexing result on the 3rd waveguide layer.

We employ the facet polishing step at the end of the fabrication process to reduce the optical scattering loss on PIC facets shown in Fig 4. 15.(b). Fig 4. 18.(a) shows the total insertion loss comparison between chips before and after the polishing process on three waveguide layers. We could conclude the approximately 1.5 dB loss reduction after the polishing process, which confirms the excellent quality of PIC facets. Fig 4. 18.(b) presents the normalized SPIDER PIC transmission spectrum on the 1st waveguide layer (bottom layer). We only use four wavelength channels at the specific baseline for the imaging process. The extra total insertion loss (6 dB) compared to the single-layer case (presented in Fig 4. 17.(b)) should result from the inherent 3 dB transmission loss of the MMI, waveguide propagation loss, and the scattering loss due to rough waveguide sidewalls and PIC facets. Fig 4. 18.(c) shows the normalized SPIDER PIC transmission spectrum on the 3rd waveguide layer (bottom layer). We experience approximately 6 dB power reduction on the top waveguide. The non-uniformity in the 3rd waveguide core layer and the interlayer coupling loss should account for such loss degradation.

To verify the radiation effects on the SPIDER PIC, we utilize the unique cyclotron in Crocker Nuclear Lab (CNL) in UC Davis, whose external beams of light could be tuned between 4 *MeV* and 67.5 *MeV*. We target at around 1 *Mrad* total radiation dosage from the cyclotron onto SPIDER chips to represent total ten years' exposure in the Low Earth Orbit (LEO). This cyclotron's large tenability and energy level provides a distinct advantage over other cyclotrons, which are mainly operating at higher energy levels and need degraders to shape to lower energy levels. The CNL's cyclotron could deliver a high-quality and stable beam with a lower energy level that meets our mission requirements with primary particles such as protons, deuterons, helions, and alphas.

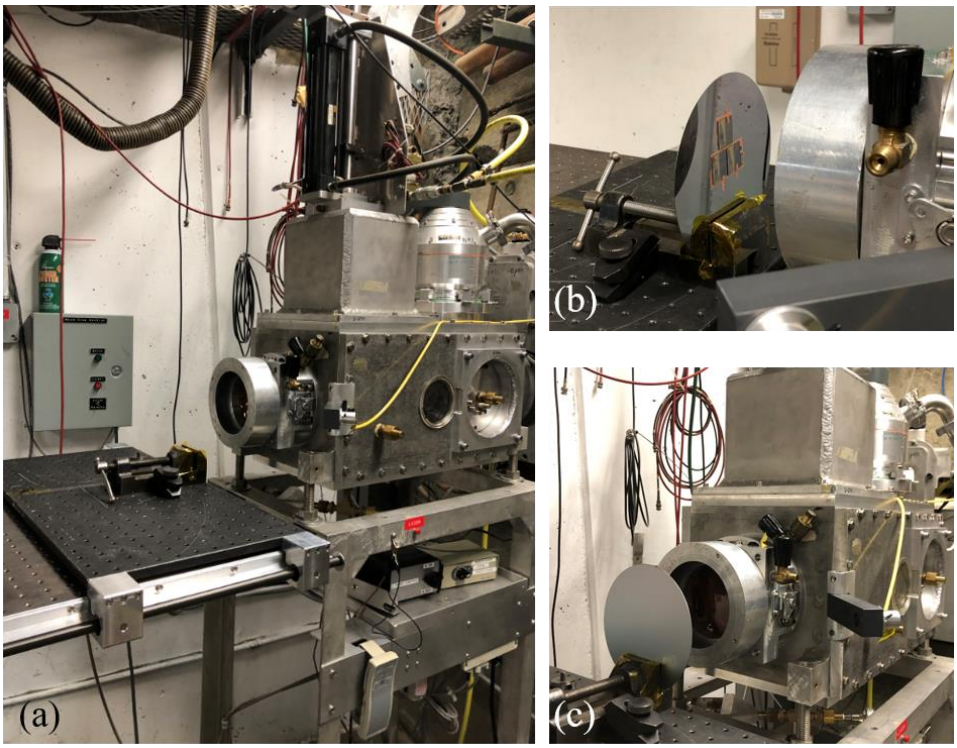

Fig 4. 19 (a) Crocker Nuclear Laboratory's 76-inch isochronous cyclotron radiation line with 5 cm diameter collimation accessories; (b) Front view of three SPIDER PICs allocated in a 4 cm diameter circle aligned to the radiation center of the cyclotron line; (c) Back view of the radiation experiments setup with carrier wafer aligned to the beam center.

Fig 4. 19 presents experimental photos of setups and device-under-tests (DUTs) for the radiation exposure. The output of accelerated beams within the cyclotron is guided through a large aperture collimator, focused with an approximately 5 cm diameter as the center circular apparatus. The optical table and clamp outside the cyclotron beam output are set on a table with three degrees of freedom in movements for optical aligning. We prepare three SPIDER PIC samples to be tested under 1 *Mrad* total run dose on a six-inch carrier wafer shown in Fig 4. 19.(a). PIC samples are arranged in a 4 cm diameter area, staying within the collimation range of the cyclotron beam. We align the center of the carrier wafer to the center of the cyclotron output beam, followed by the leakage check to maintain the leakage current of the system down to 11.2 *pA*. We seal the radiation room with a thick metal door filled with water. Then we start the radiation process after confirming the low leakage current of the system. The average beam current is 19.2 *nA*. The total run fluence is $7.49e^{+12}$ p/cm^2. And the total run time is calculated and conducted as 1 hour. We left the DUTs for cooling down and lowering the radiation dosage for four days before the optical characterization.

After radiation experiments, we retrieve DUTs and use optical setups based on OSA to conduct transmission measurements. The setup uses a broadband light source (NKT COMPACT), which provides the diffraction-limited light in the entire 450 nm~2400 nm range with the superior brightness and the wide bandwidth. Fig 4. 20.(a) provides the characterized result of the pass-through waveguides on both 150 nm-thick (red/layer 1) and 50 nm-thick (green/layer 2) waveguide layers before and after radiation exposure experiments. The average transmission loss of 50 nm-thick Si_3N_4 waveguides is 4 dB with negligible difference before and after the radiation. On the other hand, the average transmission loss of 150 nm-thick Si_3N_4 waveguides is 6 dB with negligible difference before and after the radiation. These results prove the stability of SPIDER PICs under

ten years' radiation exposure for sustainable workload in outer-space. The transmission dip around the 1400 nm wavelength results from the dangling *N-H* and *O-H* bond and could be mitigated through a high-temperature annealing process. We also move forward to characterize the SPIDER chip transmission performance shown in Fig 4. 20.(b) with four designed functioning wavelength channels before (solid line) and after (dashed line) the radiation experiment. The average peak transmission power of four wavelength channels stays at -12.5 dB before and after the radiation, proving the stability of the system under the outer-space radiation. The channel spacing of the system remains at 33 nm, and the 3 dB bandwidth remains at approximately 20 nm.

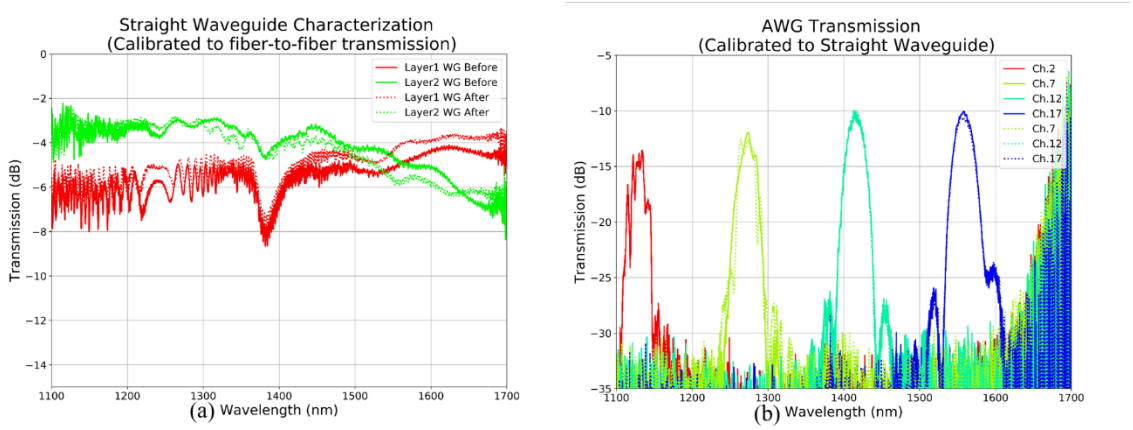

Fig 4. 20 (a) Straight waveguide transmission results before (solid line) and after (dashed line) the radiation experiments on the 150 nm-thick (red line/layer1) and 50 nm-thick (green line/layer2) nitride layers; (b) SPIDER PIC baseline demultiplexing result on the 1st waveguide layer before and after the radiation experiments.

Finally, we construct the point-source visibility fringe measurement on the 1540 nm wavelength with results shown in Fig 4. 21. The laser light is coherently divided by a fiber 2×2 coupler, generating two inputs for the 3.6 mm baseline. We utilize two current sources connected to probe stations to apply variable voltages onto the meatal heater to control delay lengths of the baseline. In the end, we collect the fringe visibility data at balanced detectors. We could fit the result to a

sinusoidal wave after normalizing the raw data to the intensity of both individual input optical beams. The spectrum provides excellent agreement with the interferometric theory. We obtain 320 *mW* electric power for the 2π phase shift. We could integrate all PICs into a multi-baseline, multi-spatial domain interferometric imager and continue fringe measurements to regenerate the object scene shown in Fig 4. 1.(a).

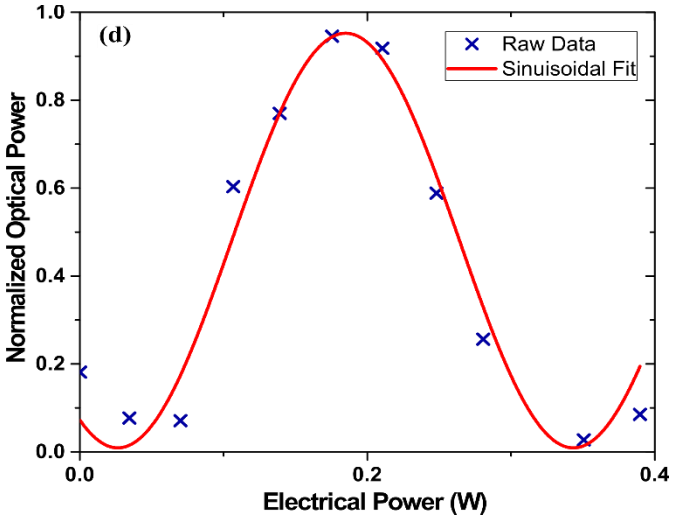

Fig 4. 21 Point-source fringe measurement result at the 1540 nm wavelength.

Reference

[1] R. P. Scott *et al.*, "Demonstration of a photonic integrated circuit for multi-baseline interferometric imaging," in *2014 IEEE Photonics Conference*, 2014, pp. 1–2.

[2] R. L. Kendrick *et al.*, "Flat-panel space-based space surveillance sensor," in *Advanced maui optical and space surveillance technologies conference*, 2013, p. E45.

[3] T. Su *et al.*, "Interferometric imaging using Si 3 N 4 photonic integrated circuits for a SPIDER imager," *Opt. Express*, vol. 26, no. 10, pp. 12801–12812, 2018.

[4] T. Su *et al.*, "Experimental demonstration of interferometric imaging using photonic integrated circuits," *Opt. Express*, vol. 25, no. 11, pp. 12653–12665, 2017.

[5] K. Badham *et al.*, “Photonic integrated circuit-based imaging system for SPIDER,” in *2017 Conference on Lasers and Electro-Optics Pacific Rim (CLEO-PR)*, 2017, pp. 1–5.

[6] G. Liu *et al.*, “Si 3 N 4 photonic integrated circuit for multi-baseline interferometric imaging,” in *2017 IEEE Photonics Conference (IPC)*, 2017, pp. 51–52.

[7] S. T. Thurman, R. L. Kendrick, A. Duncan, D. Wuchenich, and C. Ogden, “System design for a SPIDER imager,” in *Frontiers in Optics*, 2015, pp. FM3E--3.

[8] M. Françon, “Optical interferometry,” in *Neutron interferometry*, 1979.

[9] P. Hariharan, *Optical Interferometry, 2e*. Elsevier, 2003.

[10] R. Barakat, “Imaging via the van Cittert Zernike theorem using triple-correlations,” *J. Mod. Opt.*, vol. 47, no. 10, pp. 1607–1621, 2000.

[11] R. Mallart and M. Fink, “The van Cittert--Zernike theorem in pulse echo measurements,” *J. Acoust. Soc. Am.*, vol. 90, no. 5, pp. 2718–2727, 1991.

[12] K. Shang, S. Pathak, B. Guan, G. Liu, and S. J. B. Yoo, “Low-loss compact multilayer silicon nitride platform for 3D photonic integrated circuits,” *Opt. Express*, vol. 23, no. 16, pp. 21334–21342, 2015.

[13] K. Shang, S. Pathak, C. Qin, and S. J. Ben Yoo, “Low-loss compact silicon nitride arrayed waveguide gratings for photonic integrated circuits,” *IEEE Photonics J.*, vol. 9, no. 5, pp. 1–5, 2017.

[14] K. Shang *et al.*, “Silicon nitride tri-layer vertical Y-junction and 3D couplers with arbitrary splitting ratio for photonic integrated circuits,” *Opt. Express*, vol. 25, no. 9, pp. 10474–10483, 2017.

[15] A. S. Sudbo, “Film mode matching: a versatile numerical method for vector mode field calculations in dielectric waveguides,” *Pure Appl. Opt. J. Eur. Opt. Soc. Part A*, vol. 2, no. 3, p. 211, 1993.

[16] M. Bachmann, P. A. Besse, and H. Melchior, “General self-imaging properties in N$\times$ N multimode interference couplers including phase relations,” *Appl. Opt.*, vol. 33, no. 18, pp. 3905–3911, 1994.

[17] J. Leuthold and C. H. Joyner, “Multimode interference couplers with tunable power splitting ratios,” *J. Light. Technol.*, vol. 19, no. 5, p. 700, 2001.

[18] A. W. Snyder and J. D. Love, “Goos-Hänchen shift,” *Appl. Opt.*, vol. 15, no. 1, pp. 236–238, 1976.

Chapter 5 Prism-waveguide for Ultrahigh-Q Resonators

Million-level quality factor (Q-factor) resonators have been investigated and realized on traditional photonic integrated platforms such III-V platform, SOI Platform, Nitride platform, and Lithium niobate platform [1]–[3], enabling novel applications in micro-resonator modulators, on-chip frequency comb source, and biochemical sensors [4]–[6]. Moreover, dielectric materials (SiO_2, MgF_2, and CaF_2) could provide whispering gallery mode (WGM) resonators [7], [8] with the intrinsic Q factor exceeding a billion resulting from the extremely low material absorption and scattering loss. This billion-level Q factor in WGM resonators [9] has led to diverse photonic elements, including high-speed electro-optical modulators and the low-noise frequency comb source. These Kerr frequency comb sources have already contributed to LIDAR applications, optical communications, optical clocks, and the precision navigation. The Kerr frequency comb sources utilize the billion level Q factor dielectric resonators as the engine with superior advantages over other cavities:

Kerr resonators fabricated from wide energy gap dielectrics enjoy much less intrinsic loss and scattering loss compared to those made of amorphous materials. This low loss characteristic within the dielectric resonators guarantees the billion level Q factor and a high finesse, contributing to the minimum attenuation in Photonic PICs and relatively long confinement of the light propagation in the nonlinear medium.

We possess the chemical and mechanical flexibility to shape the morphology of dielectric resonators. Thus, we could easily control the transparent spectrum of these dielectric resonators.

These resonators still maintain enough mechanical and chemical strength to avoid the influence of pressure and temperature vibration. We could achieve mass production and dense packaging on these resonators, promising for the heterogeneous electro-optical integration.

Besides the benefits of low-intrinsic-loss, high-finesse, engineering flexibilities, and environmental stability, it is critical to integrate and package dielectric resonators without any degradation on the mentioned advantages. Unlike the million level on-chip waveguide-coupled resonators on the integrated photonic platforms, the dielectric resonators have not been equipped with low-loss on-chip couplers. People utilized either angle-cut fibers, tapered fiber, and free-space prisms [10], [11] to couple light in and out from dielectric resonators, suffering from the manual alignment and packaging complexity. To achieve a low-loss coupling in and out of dielectric resonators, we need to keep the mode-matched and phase-matched power exchange between WGMs in resonators and guided modes in the coupling waveguides. Besides, the optimal spatial overlap between WGMs and coupler modes, phase synchronization, mode selectivity, and the criticality of the coupling are essential qualities of integrated couplers [12], [13]. However, the relatively low refractive index (e.g. 1.37) of the typical dielectric resonators and the incompatibility between crystalline materials and traditional photonic integrated platform (SOI, nitride, Silica) materials are initial challenges for the realizing of such on-chip couplers.

In following sections, I will introduce and demonstrate a novel on-chip coupler, prism-waveguide coupler, utilizing the principle of the evanescent wave coupling [14], [15] and optical mode shaping with mode size converter fabricated on the low-loss 50 nm-thick Si_3N_4 waveguide platform [16]. This prism-waveguide coupler successfully couple light into and out of ultrahigh-Q MgF_2 resonators with 1 dB extra loss and achieve record 1.9×10^9 loaded Q factor [17], [18]. In the

end, we deliver a packaged Kerr frequency comb source [8], [19], [20] at the 26 GHz repetition rate based on this on-chip integrated dielectric resonator.

5.1 Design and Simulations

5.1.1 Ultrahigh Q MgF_2 Resonators

We use the MgF_2 resonator shown in Fig 5. 1.(a) on a metal host with an intrinsic finesse exceeding one million. We will present the corresponding fabrication technique in the following section. MgF_2 stands out of the dielectric materials due to its large optical transparent window, relatively large hardness, and superior chemical-mechanical stability. Moreover, the MgF_2 material possesses an anomalous group velocity dispersion (GVD) and a small thermo-refractive constant at the traditional telecommunication wavelength band. The phase matching between the anomalous GVD and the nonlinear process is critical for the Kerr optical frequency comb generation. Furthermore, the small thermo-refractive constant prevents the material from a low thermal instability threshold and helps the optical mode-locking between comb harmonics.

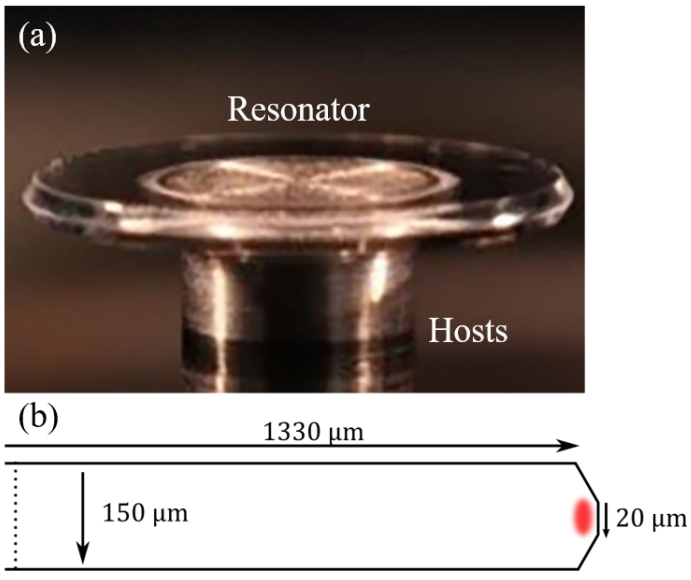

Fig 5. 1 (a) Camera photo of a transparent ultrahigh-Q MgF_2 resonator on the holding pedestal; (b) Geometric dimension of the cross-section view of a half resonator with 1.33 μm radius, 150 μm

height, and 20 μm-high wedge shape for WGM shown in red. Reprinted with permission from [17] © The Optical Society.

We design and fabricate the MgF_2 resonator with a cross-section view of a half resonator shown in Fig 5. 1.(b). The resonator is mechanically polished into a wedge shape with 2.66 mm diameter and 150 μm thickness. The edge of the resonator is fabricated into the wedge shape with 20 μm thickness, leading to a 10 μm×15 μm localized mode area illustrated in a red oval in Fig 5. 1.(b). The mode profile of the lowest order WGM is presented in Fig 5. 2.(a) with shape and power details. Moreover, we use a standard *BK7* prism coupler to measure the quality factor of the MgF_2 resonator under the critical coupling condition utilizing the ring down technique [9]. As a result, we estimate the ring-down time of the resonating power amplitude to be 10 μs at the 1550 nm wavelength, corresponding to a 6×10^9 loaded Q factor.

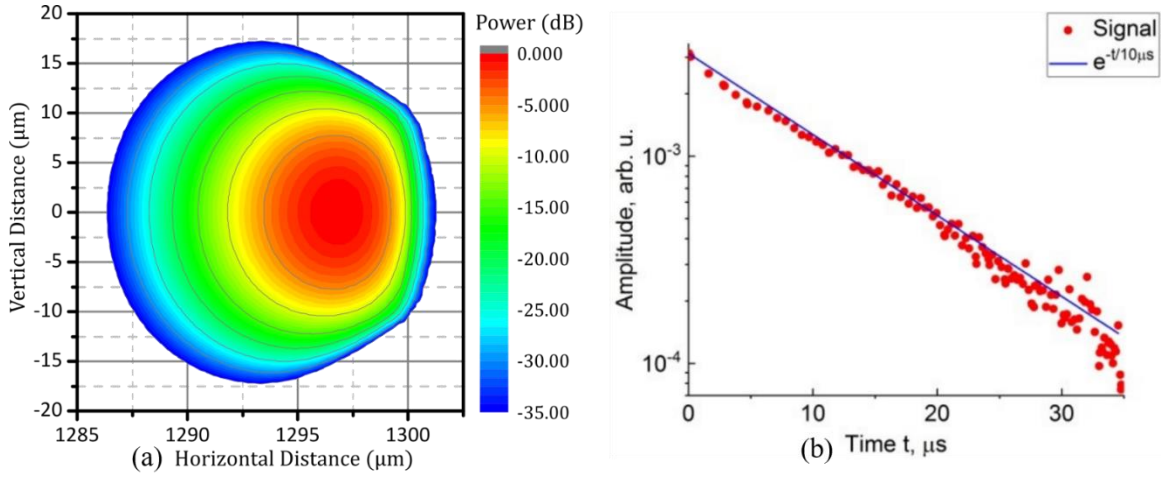

Fig 5. 2 (a) Lowest order WGM profile within the resonator with approximate 10 μm×15 μm (x axis × y axis) mode size; (b) Ring down measurement of the resonator indicating intrinsic Q factor of 6×10^9. Reprinted with permission from [17] © The Optical Society.

5.1.2 Prism-waveguide Couplers

We select the nitride waveguide platform to achieve the on-chip coupler towards the resonator introduced in the previous chapter. The nitride waveguide platform enjoys flexibility in the optical mode shaping and could achieve ultra-low-loss based on the fabrication process detailed in Chapter.2. Fig 5. 3.(a) presents the simulation result of the single-mode nitride waveguide bending radius and the mode confinement factor in the core region with respect to the waveguide core thickness. We observe a continuous decrease of the optical mode confinement factor as the waveguide core thickness reduces from 300 nm to 50 nm. The 50 nm-thick nitride waveguide platform is in favor of its lowest confinement factor (below 5%), which is essential for the mode expansion to better match the WGM shape shown in Fig 5. 2.(a). It is also demonstrated with ultra-low propagation loss in chapter 2, which helps to release the threshold in the frequency comb generation. We use the Low Pressure Chemical Vapor Deposition (LPCVD) technique to deposit the SiO_2 over-cladding for the nitride waveguide platform instead of the wafer bonding approach, free of the process complexity and suitable for the heterogeneous integration. The minimum bending radius for the 50 nm-thick Si_3N_4 waveguide platform is simulated to be 2 mm, low enough for the adiabatic condition. Fig 5. 3.(b) shows the mode power distribution of the single-mode waveguide with the core size of 6 μm×50 nm. The vertical mode radius is 0.825 μm, and the lateral mode radius is 2.7 μm, much smaller and extended compared to the WGM profile shown in Fig 5. 2.(a). However, one of the critical requirements for the successful power transmission between prism-waveguide couplers towards the dielectric resonator is the ideal optical mode matching.

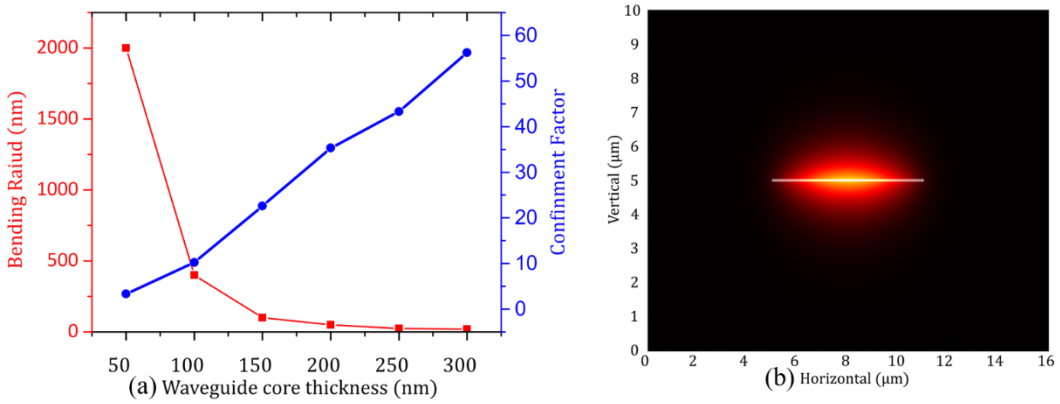

Fig 5. 3 (a) Bending radius and power confinement factor simulation with respect to Si_3N_4 waveguide platforms with different core thickness; (b) Si_3N_4 fundamental mode profile with the core size of 6 μm × 50 nm. Reprinted with permission from [17] © The Optical Society.

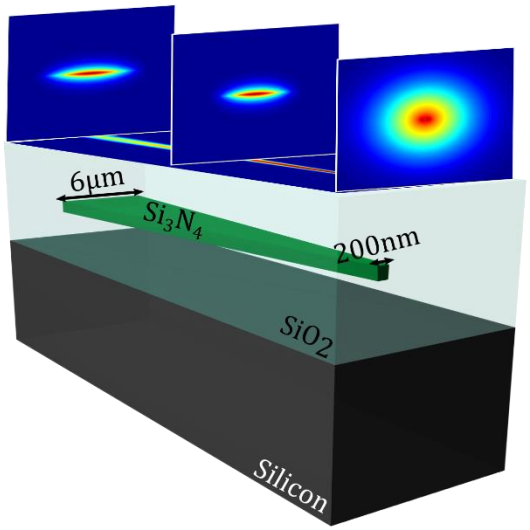

Fig 5. 4 Diagram of the Si_3N_4 waveguide negative taper mode size converter inserted with mode profiles at different taper locations. Reprinted with permission from [17] © The Optical Society.

To maximize the mode matching between the prism-waveguide coupler mode at the interaction area (at the reflection normal line shown in Fig 5. 10.(a)) and the parallel WGM (Fig 5. 2.(a)) in the MgF_2 resonator, we design and simulate a 200 μm-long adiabatic taper (shown in Fig 5. 4) to

expand the nitride waveguide mode to approximately a round shape in 10 μm diameter [21]. This expanded waveguide mode profile at the 200 nm width tip could realize the best mode matching with the target WGM in the resonator. We use the FDTD algorithm introduced in chapter 2 to simulate this negative taper spot size converter. The simulation region starts with the single-mode waveguide width of 6 μm and continuously decreases to 200 nm at the taper tip. We observe the near 100% power transmission with the taper length of 200 μm, representing the optimized adiabatic taper length. This adiabatic transmission characteristic also guarantees the single-mode condition in the structure, leading to better mode selectivity to the lowest order WGM in the MgF_2 resonator. The cross-section view of the power transmission at the top of the Fig 5. 4 confirms the optical mode power expansion at the end of the taper structure.

Moreover, three optical mode profiles above the taper diagram in Fig 5. 4 at the beginning, middle, and the end of taper interceptions demonstrate an evident mode expansion in both lateral and vertical directions. We capture the optical mode diameter along the entire taper length with results shown in Fig 5. 5. Both vertical and horizontal mode field diameter rapidly increase to approximately 10 μm at the taper tip, providing over 80% power coupling towards the lowest order WGM presented in Fig 5. 2.(a).

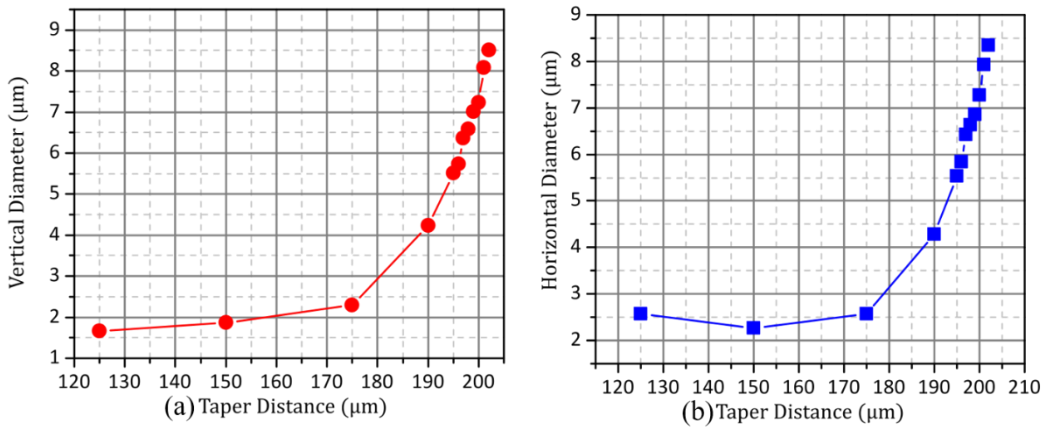

Fig 5. 5 (a) The vertical mode field diameter at different taper locations; (b) The horizontal mode field diameter at different taper locations. Reprinted with permission from [17] © The Optical Society.

Fig 5. 9 illustrates the three-dimensional packaging of the prism-waveguide coupler PIC coupling to the ultra-high-Q MgF_2 resonator. We take the top-down view of this coupling region shown in Fig 5. 10.(a) to analyze and understand another critical requirement for the low-loss coupling condition. As shown in Fig 5. 10.(a), *L* denotes the length of the adiabatic taper; *tw* indicates the taper tip core width; *d* represents the distance between the tip of the prism-waveguide coupler and the edge of the PIC; θ denotes the incident angle; *D* indicates the distance between the reflection surface normal in the PIC and the taper tip of the prism-waveguide coupler; *G* represents the gap distance between the photonic integrated chip (PIC) and resonator. θ and *G* values are the primary design parameters for achieving the phase-matching condition. First, we must select a specific θ value to satisfy the prism-like evanescent wave coupling from the prism-waveguide towards the resonator under the total internal reflection (TIR) condition. The effective index of the prism-waveguide taper tip should be close to the surrounding SiO_2 cladding material ($n_{waveguide}$ = 1.44) at the 1550 nm wavelength, and the effective index of the lowest order WGM in the resonator is simulated to be 1.37 ($n_{resonator}$ = 1.37). The fundamental phase-matching condition for the evanescent coupling requires that the propagation constant of the lowest order WGM inside the resonator equals the horizontal portion of the optical mode at the prism-waveguide coupler tip. This leads to a relationship between $n_{waveguide}$ and $n_{resonator}$: $\theta = \sin^{-1} n_{resonator}/n_{waveguide}$. Thus, we calculate the analytical incident angle value to be approximately 71.5°. The minimum incident angle for achieving TIR is calculated to be 44.0°. Therefore, the TIR condition is automatically fulfilled at the 71.5° incident angle.

We further separate the simulation process into two sections: 1) numerical simulation of the power coupling at the reflection surface presented in Fig 5. 6; 2) systematic analysis of the add-drop coupling model illustrated in Fig 5. 7. The simulation step.1) could provide essential parameters such as self-coupling coefficient, cross-coupling coefficient, and coupling loss to the analytical add-drop coupling model in the simulation step.2). Then, this add-drop coupling model could efficiently calculate the power transmission with respect to the designed variables. We use a MgF_2 waveguide of $\Delta n = 0.17$ to resemble the practical MgF_2 crystalline resonator with a 1.33 mm radius in the Lumerical FDTD®. This MgF_2 waveguide shown in Fig 5. 6 could provide a similar mode field shape (10 μm × 15 μm) compared to the practical resonator. We define following parameters in the simulation environment: W_1 represents the waveguide core width at the beginning of the taper; L indicates the linear taper length; W_2 denotes the waveguide core width at the end of the taper; θ represents the reflection angle; G indicates the air gap between the chip and resonator; d denotes the distance between the tip of the taper and the edge of the chip; D represents the distance between the tip of the taper and the reflection surface center.

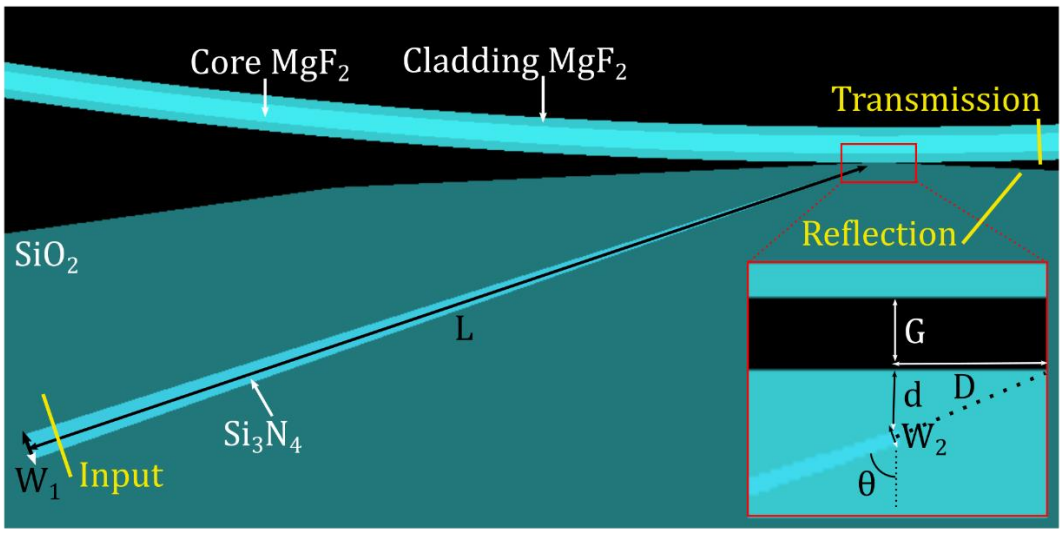

Fig 5. 6 The FDTD numerical simulation region of prism-waveguide to resonator coupling region. Three monitors (Input, Transmission and Reflection) are shown in yellow. Reprinted with permission from [17] © The Optical Society.

We set the L value to be 200 μm, the adiabatic linear taper length confirmed in the simulation presented in Fig 5. 4. We also choose the W_1 and W_2 values to be 6 μm and 200 nm, respectively. Besides, we keep the d value to be 2 μm to avoid the possible damage on the tip of the prism-waveguide taper during the fabrication process. The θ value is maintained at 71.5° to satisfy both the phase-matching condition and the TIR requirement. Finally, we excite the fundamental TE mode at the "Input" monitor shown in Fig 5. 6 and record the power reflected to the PIC at the "Reflection" monitor and the power transmitted into the MgF_2 resonator at the "Transmission" monitor. Positions of three monitors are marked with yellow lines in Fig 5. 6. Furthermore, we could summarize the self-coupling coefficient (r_1), cross-coupling coefficient (k_1), and the coupler loss (γ) with respect to the gap value G in the sweep simulation, providing critical parameters to be used in the add-drop resonator model [22], [23] in Fig 5. 7.

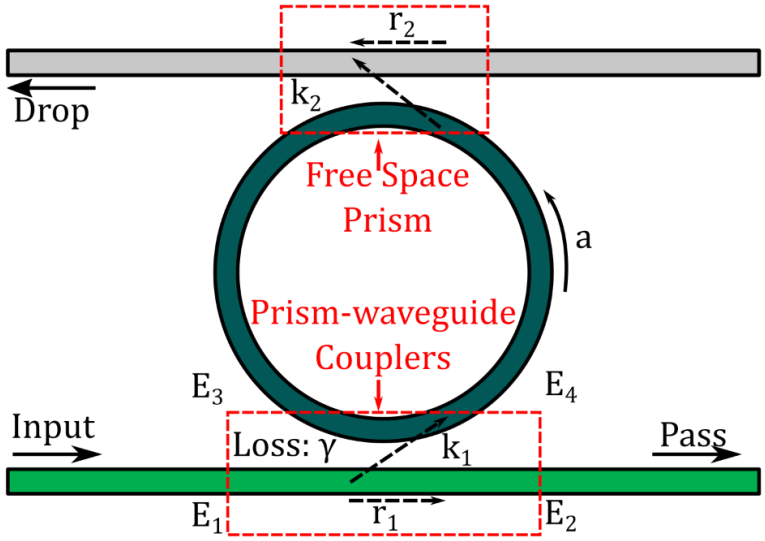

Fig 5. 7 Add-drop resonator system, an analogy to testing setup. Reprinted with permission from [17] © The Optical Society.

We depict the add-drop model shown in Fig 5. 7 analogous to our prism-waveguide PIC coupling to the crystalline resonator system. We use the prism-waveguide coupler (light-green straight waveguide) to send light into the resonator (dark-green ring) and a free space prism (grey waveguide) to couple light out of the resonator. We use the self-coupling coefficient (r_1), the cross-coupling coefficient (k_1), and the coupling loss (γ) in the prism-waveguide coupling region simulated from FDTD software shown in Fig 5. 6. We define the self-coupling coefficient and cross-coupling coefficient in the free space prism coupling area as r_2 and k_2, respectively. We neglect the coupling loss in the free space prism coupling region under the assumption that this prism coupling is ideal. To maintain the critical coupling condition in the add-drop resonator system, we ensure that $r_2 a$ equals to r_1, where a represents the amplitude coefficient in a single trip within the resonator. The a value in the ultrahigh-Q MgF_2 resonator is close to 1 due to the extremely low intrinsic scattering loss. Thus, we need to achieve a full power coupling (k_1 value is close to 1) from the prism-waveguide PIC to the resonator by controlling the G value in the simulation and characterization steps.

Once we have completed the simulation in the FDTD environment shown in Fig 5. 6, we could insert all parameters into the add-drop resonator model to derive the transmitted power spectrum. The transmission matrix model of the prism-waveguide coupling region concerning all electric field amplitudes could be summarized as Eq.(5.1). When we define the round-trip propagation length within the resonator as L_r, we could obtain the amplitude transmission coefficient (a) in terms of the power attenuation coefficient (α) in Eq.(5.2). We use the crystalline resonator with the intrinsic Q factor exceeding 10^{10} in experiments and simulations. Moreover, we could calculate the power attenuation coefficient (α) in terms of the intrinsic Q value (Q_0) following Eq.(5.3),

where ω indicates the center frequency and n_r represents the effective index of the lowest order WGM in the resonator. In the end, we could combine Eq.(5.1) to Eq.(5.3) to derive the normalized drop port power spectrum following Eq.(5.4).

$$\begin{pmatrix} E_4 \\ E_2 \end{pmatrix} = \sqrt{1-\gamma} \begin{bmatrix} r_1 & jk_1 \\ jk_1 & r_1 \end{bmatrix} \begin{pmatrix} E_3 \\ E_1 \end{pmatrix} \tag{5.1}$$

$$a = \exp\left(-\alpha L_r/2\right) \tag{5.2}$$

$$\alpha = \frac{\omega n_r}{Q_0 c} \tag{5.3}$$

$$T_d = \frac{(1-\gamma)(1-r_1^2)(1-r_2^2)a}{1-2r_1r_2\cos\Psi+(r_1r_2a)^2} \tag{5.4}$$

Where Ψ is the optical field phase shift in a single trip within the resonator defined βL_r.

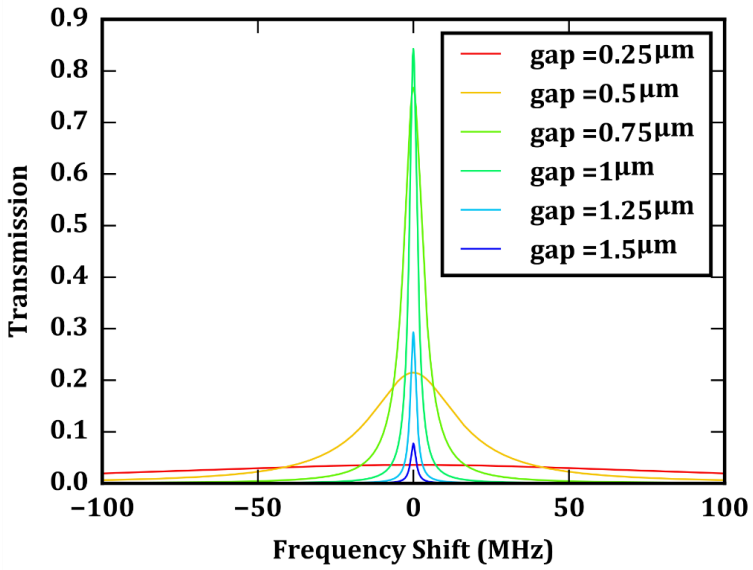

Fig 5. 8 Drop port transmission spectrum at different gap values between the prism-waveguide coupler chip and the resonator. Reprinted with permission from [17] © The Optical Society.

We obtain the normalized drop port transmission spectrum with respect to different gap values in Fig 5. 8 after applying the simulated coefficients from Fig 5. 6 into the add-drop resonator model and assuming the low loss condition in the free space prism coupling area. We could realize the maximum power transmission (approximately 1 dB loss) at the center wavelength with the gap value close to 1 μm, which confirms the principle and the feasibility of on-chip evanescent coupling between prism-waveguide couplers and the ultrahigh-Q crystalline resonator.

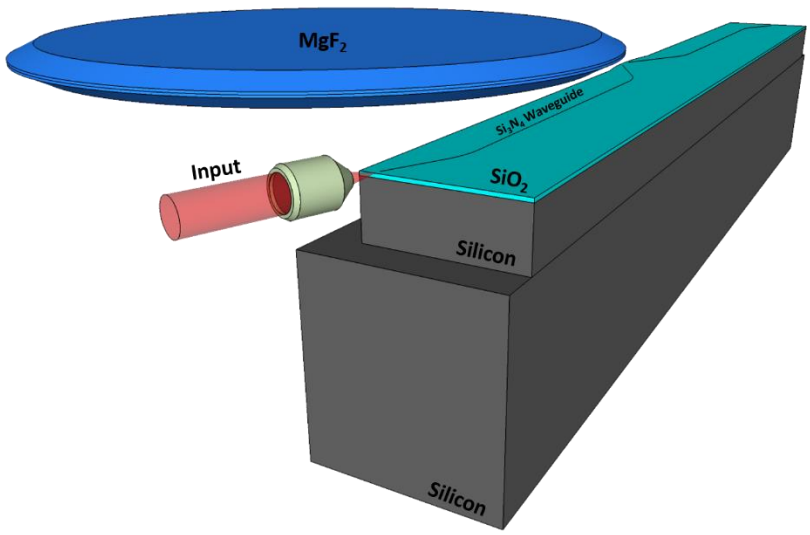

Fig 5. 9 The three-dimensional diagram of the MgF_2 resonator coupling to the paired prism-waveguide couplers.

We include variations in the design value *d*, *tw*, and θ in the first version of the single prism-waveguide lithography mask layout (10 mm × 4.5 mm PIC size) shown in Fig 5. 10.(a) to justify the best parameter combinations after the practical fabrication process. Then, we characterize the best parameter combinations following the fabrication and characterization technique described in following sections for this single prism-waveguide coupler. Furthermore, we design the second version of the paired prism-waveguide coupler lithography mask layout (3.6 mm × 0.42 mm PIC

size) shown in Fig 5. 10.(c), consisting of one pass-through waveguide for the power normalization and mirror-positioned single prism-waveguide couplers, to facilitate the power coupling out of the resonator in the same PIC. The paired prism-waveguide couplers are separated with a distance *2D*, relying on the trigonometric relationship between the incident angle (θ) and the distance between taper tip and the PIC edge (*d*). This specific separation value is chosen to realize the best phase-matching condition for both input and output prism-waveguide couplers. Besides, we apply the 20° angular rotation on all input and output waveguide ports to suppress the optical power reflection at PIC facets to better achieve the self-injection locking [24], [25] with a distributed feedback laser (DFB) module based on the Rayleigh scattering light from the crystalline resonator.

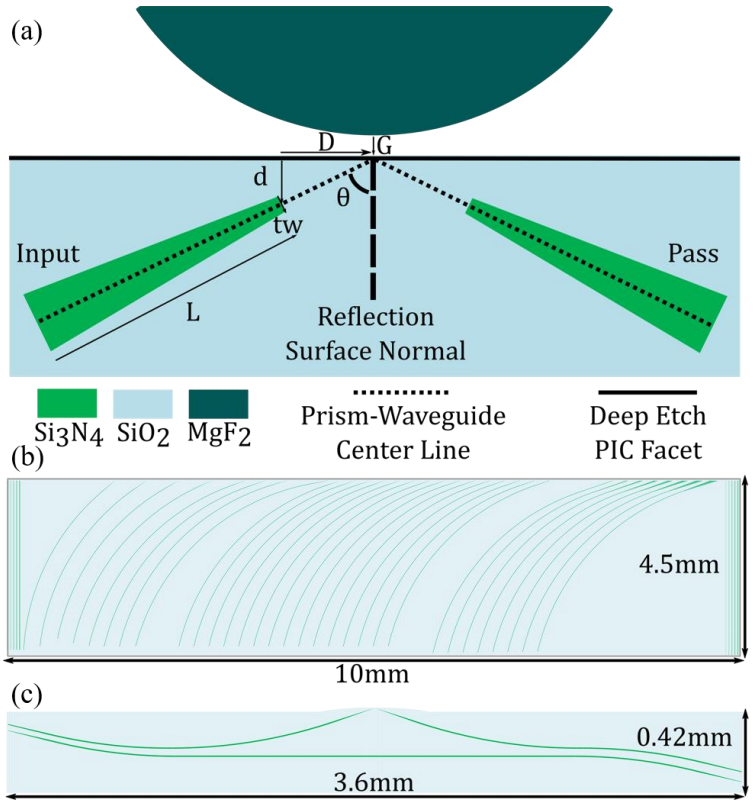

Fig 5. 10 (a) Geometric configuration of prism-waveguide couplers maintaining phase synchronized coupling towards resonator (used in FDTD simulation); (b) The testing PIC (10 × 4.5 mm^2) containing individual prism-waveguide couplers with variations in θ, *d* and *tw*; (c) The PIC (3.6 × 0.42 mm^2) containing a pair of prism-waveguide couplers (single prism-waveguide

coupler with the best performance tested through mask shown in (b) and an end-to-end waveguide for alignment assistance. Reprinted with permission from [17] © The Optical Society.

5.2 Fabrications

5.2.1 Ultrahigh Q MgF_2 Resonators Fabrication Techniques

We start the fabrication of the ultrahigh-Q MgF_2 resonator from a high-quality MgF_2 wafer grounded from a cylindrical MgF_2 preform. Then, we mechanically polished the preform into the geometry shown in Fig 5. 1.(a) utilizing a diamond slurry, shaping the WGM profile into a 10 μm×15 μm mode area to be matched with the nitride prism-waveguide coupler. We carefully select the mechanical polishing parameters best for the MgF_2 material at the specific angle cut to realize the high finesse and ultralow loss performance. Moreover, we precisely control the resonator surface quality during the fabrication process to ensure no Rayleigh scattering light is observed in the resonator. The surface roughness at the order of a crystalline lattice period is confirmed by scanning electron microscopy (SEM) measurements.

5.2.2 Prism-waveguide Couplers Fabrication Techniques

We complete the single-layer 50 nm-thick Si_3N_4 prism-waveguide coupler PIC fabrication following the process flow shown in Fig 5. 11. The description of the fabrication details is:

1) We prepare the p-type six-inch silicon wafer after the 120 ℃ piranha cleaning to avoid any pre-deposition dusts.

2) We deposit over 5 μm-thick low temperature oxide (LTO) at 450 ℃ employing the LPCVD technique.

3) We deposit the 50 nm-thick nitride waveguide layer at 800 ℃ using the LPCVD technique.

4) We accomplish the lithography and exposure on photoresists for alignment marks on the waveguide layer using the ASML™ 5500/300 DUV stepper. The three-dimensional illustration of the PIC die is presented in Fig 5. 12.(a).1.

5) We etch into the SiO_2 bottom-cladding to form the optical alignment marks.

6) We perform the DUV lithography process to develop photoresist patterns for the waveguide core region.

7) we use the developed low-loss nitride etching recipe to process the waveguide core by inductively coupled plasma (ICP) etching. Fig 5. 12.(a).2 shows the patterned nitride layer with pass-through waveguides and paired prism-waveguide couplers.

8) We deposit another 5 μm-thick LTO as the waveguide top-cladding. Fig 5. 12.(a).3 illustrates the prism-waveguide coupler PIC after the top-cladding deposition step.

9) We deposit the 500 nm-thick amorphous Silicon (a-Si) at the top of the cladding as the hard-mask for the facet deep-etching.

10) We finish the lithography of the 5μm-thick DUV photoresist to assist the deep-etching process.

11) We etch through the oxide layer and into the Silicon substrate for approximately 100 μm in depth.

12) We perform a Xenon Difluoride (XeF_2) dry etching on the fabricated PIC to remove approximately 30 μm-thick Silicon substrate underneath the edge of the PIC.

This step is critical for the low-loss coupling from the laser light into the PIC illustrated in Fig 5. 9. It prevents the optical power leakage into the high index Silicon substrate. Fig 5. 12.(a).4 shows

the PIC diagram after the entire fabrication process. In the end, we perform a mechanical dicing on the fabricated wafer to shape the PIC into the 3.6 × 0.42 mm^2 area to integrate with the MgF_2 resonator shown in Fig 5. 1.(a).

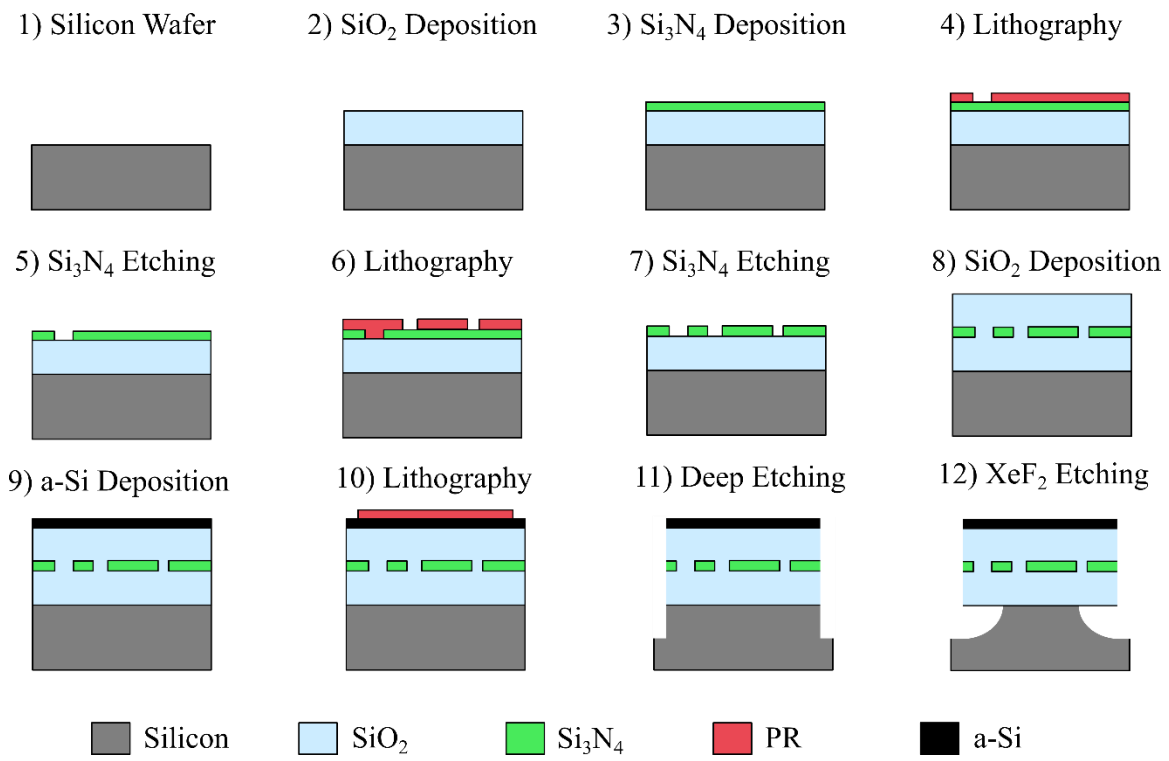

Fig 5. 11 CMOS-compatible fabrication process of the paired prism-waveguide PIC based on the low-loss Si_3N_4 waveguide platform.

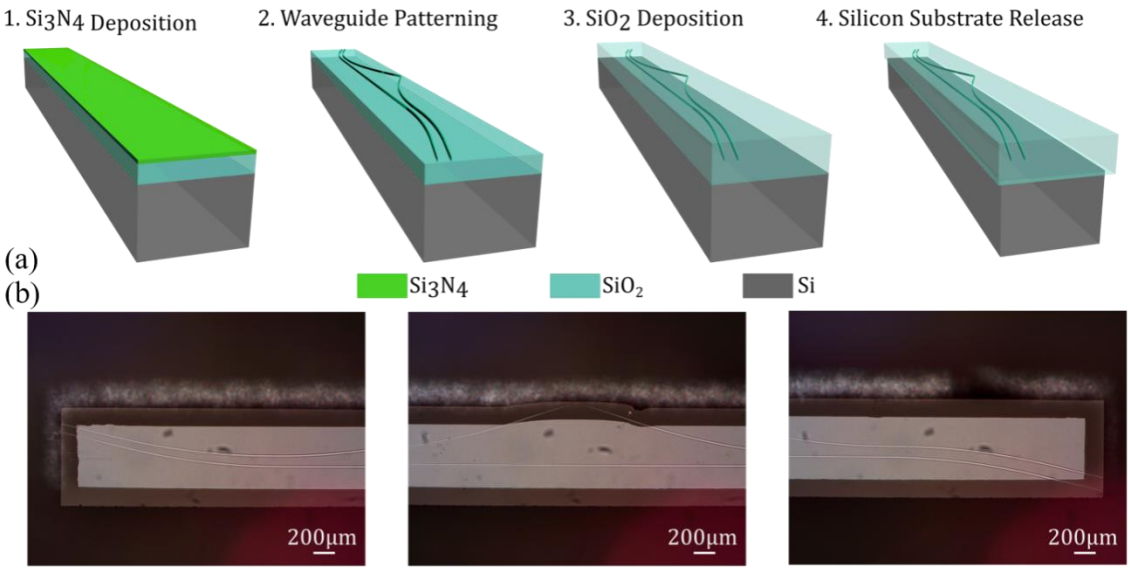

Fig 5. 12 (a) Three-dimensional illustration of the critical fabrication steps: 1. Si_3N_4 LPCVD deposition; 2. Si_3N_4 waveguide core patterning; 3. SiO_2 over-cladding deposition; 4. PIC Facet deep etching followed by XeF_2 release of substrate Silicon at the PIC edge; (b) The fabricated PIC picture at the left, center and right position based on mask shown in Fig 5. 10.(c). Reprinted with permission from [17] © The Optical Society.

5.3 Integration and Characterizations

5.3.1 Demonstration of single prism-waveguide coupled to the ultrahigh-Q MgF_2 resonator

We start transmission experiments by confirming the loaded Q factor of the testing resonator in the over-coupling condition with a tunable narrow linewidth laser. The transmission spectrum shows that the excess loss does not exceed 3 dB and the loaded Q factor is on the order of a billion. Thus, the intrinsic Q factor of the resonator does not degrade a lot during the integration process, beneficial for applications such as efficient band-pass filters. We establish the measurement setup shown in Fig 5. 13.(a) for single prism-waveguide couplers in the first mask layout presented in Fig 5. 10.(b). We could utilize this setup to efficiently couple light into and out of the resonator towards the single prism-waveguide coupler and estimate the coupling efficiency between the prism-waveguide coupler and the crystalline resonator.

Moreover, we could obtain the waveguide transmission loss on the prism-waveguide PIC and estimate the power coupling efficiency from the prism-waveguide PIC. The insert in Fig 5. 13.(a) presents the actual interface between the angled tip of the prism-waveguide coupler and the corresponding resonator. The Silicon substrate is completely removed under the transparent region to avoid the WGM coupling towards the high index substrate region.

The "Waveguide Mode Launcher 1" contains a *SMF-28* fiber, collimated and focused by Thorlabs *C230* and *C280* aspheric lenses, providing the mode field diameter of approximately 5 μm at the focal point. This optical mode profile matches well with the input mode profile at the prism-waveguide PIC. We assess the insertion loss by comparing the optical power out of straight-through waveguides (shown as the green straight line in Fig 5. 13.(a)) to the optical power excited in the single-mode fiber. A 3.8 dB insertion loss is measured due to the optical mode coupling loss, facet scattering loss, and the propagation loss in straight-through waveguides.

Furthermore, we align the "Waveguide Mode Launcher 1" to the single prism-waveguide coupler (shown as the green curved line in Fig 5. 13.(a)), and position the crystalline resonator to the proximity of the edge of the PIC with details shown in the insert photo of Fig 5. 13.(a). Then, we operate another translation stage to bring the free-space prism to couple the optical power out of the MgF_2 resonator. Finally, we use a large area multimode fiber ("Light pipe") to collect the light power exiting the free-space prism, and send the collected light power into a photodetector to analyze the fundamental WGM. Moreover, we use an additional "WG Launcher 2" to match the lowest order WGM field at the TIR surface of the prism to maintain the symmetry between input and output power coupling. Thus, we could maximize the optical power transmission in the setup and obtain the transmission loss with respect to the loaded bandwidth by controlling the two gaps

illustrated in Fig 5. 7. We use a tunable laser at the 1550 nm wavelength and a fiber interferometer to estimate the loaded optical bandwidth of the system.

We obtain the minimum coupling loss between the PIC and the resonator of 1 dB with a heavily loaded bandwidth of 3.2 MHz. This best single prism-waveguide coupler is designed with following geometric parameters: $\theta = 71.5°$, $d = 2\ \mu m$, $tw = 200\ nm$. Fig 5. 13.(b) presents the measurement result of the loaded Q factor of 1.9 billion at the 1550 nm wavelength with a 100 kHz bandwidth.

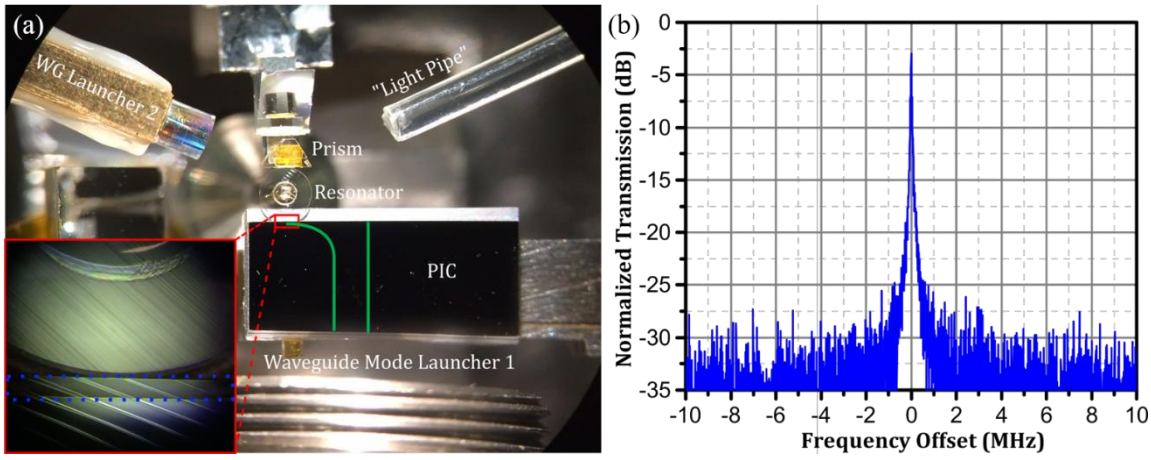

Fig 5. 13 (a) Measurement setup for a single prism-waveguide coupler with straight calibration waveguides (shown in green lines). The insert is the microscope picture of the fabricated chip containing prism-waveguide couplers aligned to the resonator where Silicon substrate released region (step.4 in Fig 5. 12.(a)) is shown in blue dotted rectangle. (b) Normalized transmitted power received at the light pipe from (a), indicating the loaded quality factor of 1.9×10^9. Reprinted with permission from [17] © The Optical Society.

5.3.2 Demonstration of prism-waveguide-assisted optical injection locking of DFB laser to the resonator

Next, we prepare the experimental setup shown in Fig 5. 14 to examine the quality of the optical injection locking from the prism-waveguide coupled resonator system to a DFB laser. The optical injection locking phenomenon is a critical step to achieve the waveguide coupled Kerr optical frequency comb source based on the MgF_2 resonator, where low coupling loss is required to realize

the sufficient back-scattering in both propagating and reflection direction of the laser light. We couple two single prism-waveguide couplers to the MgF_2 resonator (1 in Fig 5. 14) simultaneously in Fig 5. 14. The DFB laser assembly (4 in Fig 5. 14) sends the light power through the beam profile transformer to better match the optical mode profile in the best prism-waveguide coupler in the PIC (2 in Fig 5. 14). We use an active micro-stage to hold the DFB laser assembly for a rapid alignment process.

Furthermore, we utilize a second, weakly coupled, prism-waveguide coupler PIC (3 in Fig 5. 14) to capture the light power out of the resonator. Finally, we use a "Light pipe" (5 in Fig 5. 14) to collect this light power and transfer it to the photodetector. We also use an additional multimode waveguide to receive the reflected light in the first prism-waveguide coupler PIC as a reference. As a result, we could successfully maintain the injection locking phenomenon in a 5 GHz range with the optimal gap distance obtained from the previous experiment. This 5 GHz injection locking range is comparable to the existing crystalline resonator injection-locked lasers relying on the free-space prisms as couplers [26], [27].

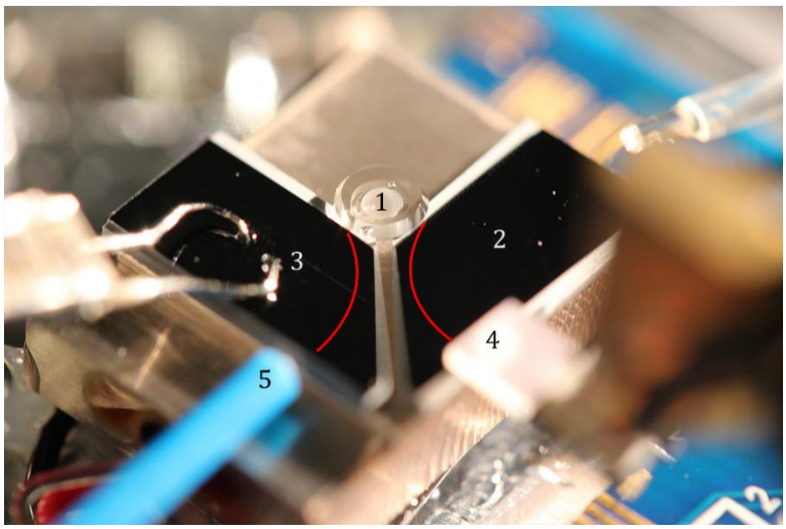

Fig 5. 14 Photo of the injection locking setup illustrating two chips containing the single prism-waveguide coupler integrated to a resonator. (1) is the resonator, (2) and (3) are the prism-waveguide PIC, (4) and (5) are fiber launchers. Reprinted with permission from [17] © The Optical Society.

5.3.3 Demonstration of packaged Kerr frequency comb source based on paired prism-waveguide couplers

We fabricate and deliver the paired prism-waveguide couplers PIC following the lithography mask shown in Fig 5. 10.(c) and the fabrication methods detailed in the fabrication chapter, utilizing the best design parameters tested in the previous section. We use the in-house OVNA step shown in Fig 5. 15.(a) to characterize the transmission spectrum of the pass-through waveguide and the total internal reflected signals through both input and output prism-waveguide couplers. “TLS” stands for the tunable laser source, “PC” represents the polarization controller, “BD” denotes the balanced detector, “90/10” and “50/50” are the fiber power spitters at the specific ratio. As a result, we could extract the reflected power spectrum presented in Fig 5. 15.(b) with approximately 2 dB excess loss compared to the ideal TIR condition. This degradation should result from the scattering light at the reflection surface, unguided optical power at the prism-waveguide tip, and the insufficient cladding material at the tip region.

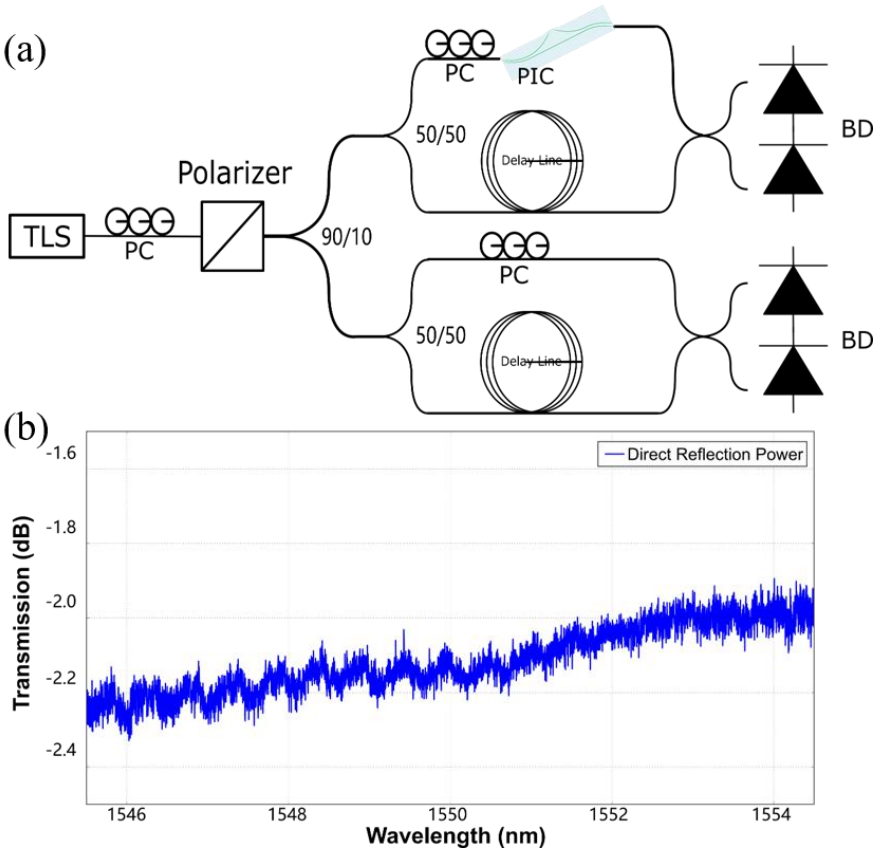

Fig 5. 15 (a) The OVNA measurement setup for 20° angled paired prism-waveguide couplers chips; (b) The measurement result of the total internal reflected signal power.

Fig 5. 16.(a) presents the top-down configuration of the packaged comb unit based on the fabricated paired prism-waveguide couplers PIC. We rotate the PIC 20° counterclockwise to prevent the laser light reflection at the input facet for a stable optical injection locking condition. The desired Kerr frequency comb at the specific repetition frequency will be generated when we satisfy the following requirements: (1) The laser light should be coupled to the MgF_2 resonator with sufficiently low loss; (2) The optical power within the resonator exceeds the frequency comb threshold; (3) The laser light is injection-locked to the WGM in the resonator. We could achieve the optical injection locking in the paired prism-waveguide PIC when we increase the laser pump

current to over 80 mA. Fig 5. 16.(b) and Fig 5. 16.(c) show the sketch and the actual photo of the packaged comb unit. We excite the coherent frequency comb by generating the positive optical feedback and choosing the optimal detuning value. Fig 5. 16 presents the optical frequency comb at the 26 GHz repetition rate captured in an optical spectrum analyzer.

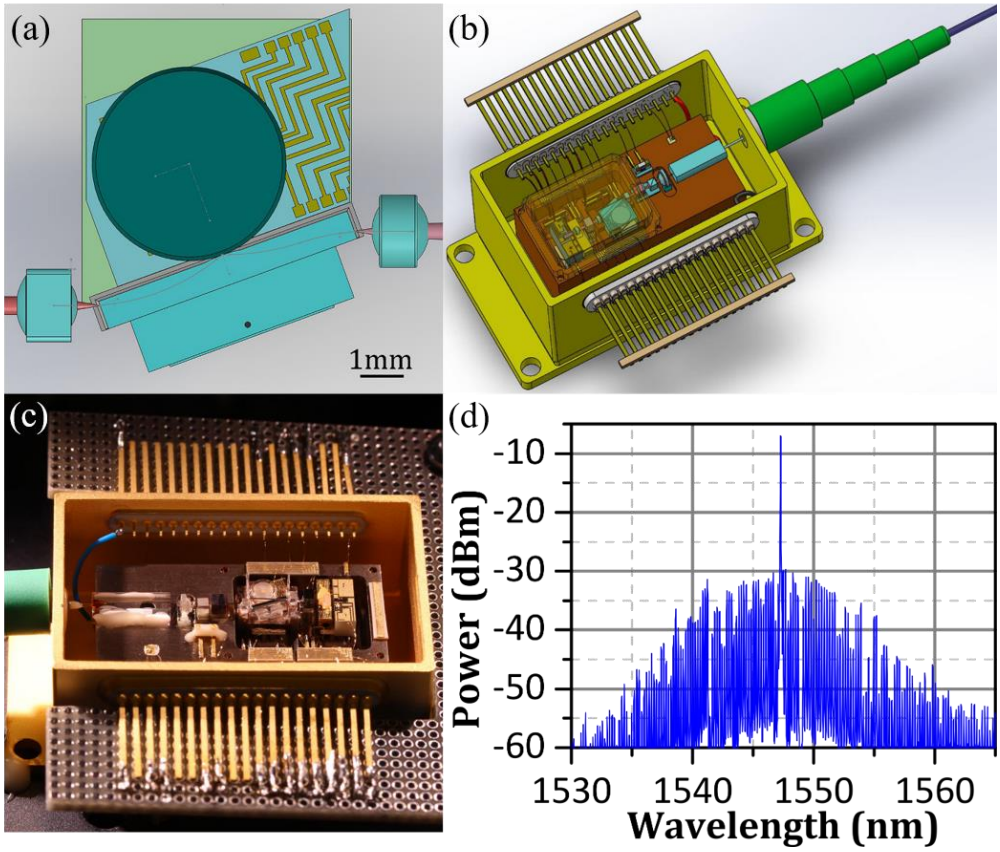

Fig 5. 16 (a) 3D Diagram of paired-prism-waveguide couplers integrated to the resonator for comb generation; (b) Illustration of the delivered Kerr frequency comb source; (c) Photo of packaged on-chip waveguide integrated frequency comb source; (d) Representative Kerr frequency comb output from the integrated package. Reprinted with permission from [17] © The Optical Society.

Reference

[1] L. Razzari *et al.*, "CMOS-compatible integrated optical hyper-parametric oscillator," *Nat. Photonics*, vol. 4, no. 1, pp. 41–45, 2010.

[2] J. S. Levy, A. Gondarenko, M. A. Foster, A. C. Turner-Foster, A. L. Gaeta, and M. Lipson, "CMOS-compatible multiple-wavelength oscillator for on-chip optical interconnects," *Nat. Photonics*, vol. 4, no. 1, pp. 37–40, 2010.

[3] D. T. Spencer, J. F. Bauters, M. J. R. Heck, and J. E. Bowers, "Integrated waveguide coupled Si 3 N 4 resonators in the ultrahigh-Q regime," *Optica*, vol. 1, no. 3, pp. 153–157, 2014.

[4] M. Aspelmeyer, T. J. Kippenberg, and F. Marquardt, "Cavity optomechanics," *Rev. Mod. Phys.*, vol. 86, no. 4, p. 1391, 2014.

[5] J. Pfeifle *et al.*, "Coherent terabit communications with microresonator Kerr frequency combs," *Nat. Photonics*, vol. 8, no. 5, pp. 375–380, 2014.

[6] J. Zhu *et al.*, "On-chip single nanoparticle detection and sizing by mode splitting in an ultrahigh-Q microresonator," *Nat. Photonics*, vol. 4, no. 1, pp. 46–49, 2010.

[7] K. J. Vahala, "Optical microcavities," *Nature*, vol. 424, no. 6950, pp. 839–846, 2003.

[8] V. S. Ilchenko, A. A. Savchenkov, A. B. Matsko, and L. Maleki, "Nonlinear optics and crystalline whispering gallery mode cavities," *Phys. Rev. Lett.*, vol. 92, no. 4, p. 43903, 2004.

[9] A. A. Savchenkov, A. B. Matsko, V. S. Ilchenko, and L. Maleki, "Optical resonators with ten million finesse," *Opt. Express*, vol. 15, no. 11, pp. 6768–6773, 2007.

[10] V. S. Ilchenko, X. S. Yao, and L. Maleki, "Pigtailing the high-Q microsphere cavity:? a simple fiber coupler for optical whispering-gallery modes," *Opt. Lett.*, vol. 24, no. 11, pp. 723–725, 1999.

[11] M. Cai, O. Painter, and K. J. Vahala, "Observation of critical coupling in a fiber taper to a silica-microsphere whispering-gallery mode system," *Phys. Rev. Lett.*, vol. 85, no. 1, p. 74, 2000.

[12] S. M. Spillane, T. J. Kippenberg, O. J. Painter, and K. J. Vahala, "Ideality in a fiber-taper-coupled microresonator system for application to cavity quantum electrodynamics," *Phys. Rev. Lett.*, vol. 91, no. 4, p. 43902, 2003.

[13] M. L. Gorodetsky and V. S. Ilchenko, "Optical microsphere resonators: optimal coupling to high-Q whispering-gallery modes," *JOSA B*, vol. 16, no. 1, pp. 147–154, 1999.

[14] R. Ulrich, "Theory of the prism--film coupler by plane-wave analysis," *JOSA*, vol. 60, no. 10, pp. 1337–1350, 1970.

[15] M. L. Gorodetsky and V. S. Ilchenko, "High-Q optical whispering-gallery microresonators: precession approach for spherical mode analysis and emission patterns with prism couplers," *Opt. Commun.*, vol. 113, no. 1–3, pp. 133–143, 1994.

[16] K. Shang, S. Pathak, B. Guan, G. Liu, and S. J. B. Yoo, "Low-loss compact multilayer silicon nitride platform for 3D photonic integrated circuits," *Opt. Express*, vol. 23, no. 16, pp. 21334–21342, 2015.

[17] G. Liu *et al.*, "Low-loss prism-waveguide optical coupling for ultrahigh-Q low-index monolithic resonators," *Optica*, vol. 5, no. 2, pp. 219–226, 2018.

[18] G. Liu *et al.*, "Low-loss on-chip prism-waveguide coupler to high-Q micro-resonator and optical frequency comb generation," in *Optical Fiber Communication Conference*, 2017, pp. Tu3K--6.

[19] W. Liang *et al.*, "High spectral purity Kerr frequency comb radio frequency photonic oscillator," *Nat. Commun.*, vol. 6, no. 1, pp. 1–8, 2015.

[20] T. J. Kippenberg, R. Holzwarth, and S. A. Diddams, “Microresonator-based optical frequency combs,” *Science (80-.).*, vol. 332, no. 6029, pp. 555–559, 2011.

[21] V. R. Almeida, R. R. Panepucci, and M. Lipson, “Nanotaper for compact mode conversion,” *Opt. Lett.*, vol. 28, no. 15, pp. 1302–1304, 2003.

[22] W. Bogaerts *et al.*, “Silicon microring resonators,” *Laser \& Photonics Rev.*, vol. 6, no. 1, pp. 47–73, 2012.

[23] Q. Xu, D. Fattal, and R. G. Beausoleil, “Silicon microring resonators with 1.5-$μ$m radius,” *Opt. Express*, vol. 16, no. 6, pp. 4309–4315, 2008.

[24] R. Lang, “Injection locking properties of a semiconductor laser,” *IEEE J. Quantum Electron.*, vol. 18, no. 6, pp. 976–983, 1982.

[25] M. L. Gorodetsky, A. D. Pryamikov, and V. S. Ilchenko, “Rayleigh scattering in high-Q microspheres,” *JOSA B*, vol. 17, no. 6, pp. 1051–1057, 2000.

[26] B. Dahmani, L. Hollberg, and R. Drullinger, “Frequency stabilization of semiconductor lasers by resonant optical feedback,” *Opt. Lett.*, vol. 12, no. 11, pp. 876–878, 1987.

[27] W. Liang, V. S. Ilchenko, A. A. Savchenkov, A. B. Matsko, D. Seidel, and L. Maleki, “Whispering-gallery-mode-resonator-based ultranarrow linewidth external-cavity semiconductor laser,” *Opt. Lett.*, vol. 35, no. 16, pp. 2822–2824, 2010.

Chapter 6 Summary

This dissertation introduced the design, fabrication, and characterization flow of photonic integrated circuits, emphasizing the low-loss silicon nitride waveguide platform in chapter 2. The developed hard-mask assisted fabrication technique delivered the nitride waveguide platform with the dB/m level propagation loss. We also investigated the multilayer nitride platform to increase the integration density and mitigate the routing complexity. Moreover, the nitride platform possesses the flexibility to design the waveguide core thickness. As a result, we could simultaneously achieve ultra-low loss and a small device footprint. Moreover, the stoichiometric Si_3N_4 material is CMOS compatible with the popular SOI platforms and maintains the opportunity for heterogeneous integration to active devices in the vertical direction.

Chapter 3 introduced the principle and the developed modelling technique for arrayed waveguide gratings serving as multiplexers and routers. First, we established the Gaussian models for AWGs with the simulation time at the minute level. Then, we presented detailed simulation results of AWG demultiplexers and routers for both optical communication O band and C band. In the end, we delivered the eight-channel AWGs with the 1 dB insertion loss and the 30 dB crosstalk level. The performance degradation compared to the simulation results from the fabrication non-ideality and the additional scattering loss at interfaces. Moreover, we utilized the multimode interferometer as AWG inputs to expand the mode profile, successfully realized the flat-top AWG router at CWDM wavelength grids.

Chapter 4 demonstrated the new generation of the SPIDER PIC consisting of edge couplers, path-length-matching waveguides, metal heater assisted multimode interferometers, wide bandwidth AWG demultiplexers. The entire PIC is fabricated on a three-layer nitride waveguide platform in

the 22 mm × 22 mm die size. We realized a dual-port, 18 wavelength channels, 3.3 THz channel spacing, and side-input AWG demultiplexer following the design routine established in Chapter 3. Furthermore, we concluded the excellent anti-radiation capability of the PIC, meeting requirements for the possible outer space mission. Our collaborators also help to accomplish imaging experiments in the Fourier spatial domain.

Chapter 5 presented prism-waveguide couplers for the ultra-high-Q crystalline resonator to achieve the packaged Kerr frequency comb source. We developed the prism-waveguide coupler concept by combing traditional bulky prisms and integrated waveguide couplers, exploiting the evanescent coupling mechanism. We built the semi-analytical simulation environment for this prism-waveguide coupled resonator system and obtained initial gap values under the critical coupling condition. Then, we applied the low-loss nitride fabrication process flow to deliver the paired prism-waveguide couplers PICs, packaged MgF_2 resonators with a record 1.9 billion loaded Q factor. In the end, we assembled a Kerr frequency comb source at the 26 GHz repetition rate in the commercial butterfly package.

APPENDIX A: LIST OF PUBLICATIONS

Publications in international journals

1. **Liu, Guangyao**, Vladimir S. Ilchenko, Tiehui Su, Yi-Chun Ling, Shaoqi Feng, Kuanping Shang, Yu Zhang et al. "Low-loss prism-waveguide optical coupling for ultrahigh-Q low-index monolithic resonators." *Optica 5, no. 2 (2018): 219-226*.
2. Su, Tiehui, **Guangyao Liu**, Katherine E. Badham, Samuel T. Thurman, Richard L. Kendrick, Alan Duncan, Danielle Wuchenich et al. "Interferometric imaging using Si 3 N 4 photonic integrated circuits for a SPIDER imager." *Optics express 26, no. 10 (2018): 12801-12812*.
3. Shang, Kuanping, Chuan Qin, Yu Zhang, **Guangyao Liu**, Xian Xiao, Shaoqi Feng, and S. J. B. Yoo. "Uniform emission, constant wavevector silicon grating surface emitter for beam steering with ultra-sharp instantaneous field-of-view." *Optics express 25, no. 17 (2017): 19655-19661*.
4. Shang, Kuanping, Shibnath Pathak, **Guangyao Liu**, Shaoqi Feng, Siwei Li, Weicheng Lai, and S. J. B. Yoo. "Silicon nitride tri-layer vertical Y-junction and 3D couplers with arbitrary splitting ratio for photonic integrated circuits." *Optics express 25, no. 9 (2017): 10474-10483*.
5. Shang, Kuanping, Shibnath Pathak, Binbin Guan, **Guangyao Liu**, and S. J. B. Yoo. "Low-loss compact multilayer silicon nitride platform for 3D photonic integrated circuits." *Optics Express 23, no. 16 (2015): 21334-21342*.
6. Shen, Yang, Feng, Shaoqi, Xie, Xiaojun, Zang, Jizhao, Li, Siwei, Su, Tiehui, Shang, Kuanping, Lai, Weicheng, **Liu, Guangyao**, Yoo, S.B. and Campbell, J.C., 2017. "Hybrid integration of modified uni-traveling carrier photodiodes on a multi-layer silicon nitride platform using total reflection mirrors." *Optics express, 25(9), pp.9521-9527*.
7. Feng, Shaoqi, Chuan Qin, Kuanping Shang, Shibnath Pathak, Weicheng Lai, Binbin Guan, Matthew Clements, Tiehui Su, **Guangyao Liu**, Hongbo Lu, Ryan P. Scott, and S. J. Ben Yoo. "Rapidly reconfigurable high-fidelity optical arbitrary waveform generation in heterogeneous photonic integrated circuits." *Optics express 25, no. 8 (2017): 8872-8885*.

Publications in international conferences

8. **Liu, Guangyao**, Argishti Melikyan, SJ Ben Yoo, and Po Dong. "Modelling directly reflectivity modulated lasers." In *CLEO: Applications and Technology, pp. JTu2A-76. Optical Society of America, 2019*.
9. Zhang, Yu, Chuan Qin, Kuanping Shang, Gengchen Liu, **Guangyao Liu**, and SJ Ben Yoo. "Sub-wavelength spacing optical phase array nanoantenna emitter with vertical silicon photonic vias." In *2018 Optical Fiber Communications Conference and Exposition (OFC), pp. 1-3. IEEE, 2018*.
10. Prost, Mathias, **Guangyao Liu**, and SJ Ben Yoo. "A compact thin-film lithium niobate platform with arrayed waveguide gratings and MMIs." In *2018 Optical Fiber Communications Conference and Exposition (OFC), pp. 1-3. IEEE, 2018*.

11. **Liu, Guangyao**, Tiehui Su, Siwei Li, Jaeyi Chun, Weicheng Lai, Mathias Prost, Chad Ogden et al. "Si 3 N 4 photonic integrated circuit for multi-baseline interferometric imaging." In *2017 IEEE Photonics Conference (IPC), pp. 51-52. IEEE, 2017*.

12. Qin, Chuan, Kuanping Shang, Shaoqi Feng, Gengchen Liu, **Guangyao Liu**, Shibnath Pathak, and SJ Ben Yoo. "1× 256 Multi-layer, low-loss, Si3N4 waveguide optical phased arrays with 0.050 Instantaneous-Field-of-View." In *CLEO: Science and Innovations, pp. STh1M-2. Optical Society of America, 2017*.

13. Su, Tiehui, Siwei Li, Shaoqi Feng, Weicheng Lai, **Guangyao Liu**, and S. J. B. Yoo. "A 2/3-octave-spanning three spectral band splitter on a Si 3 N 4 photonic integrated circuit platform." In *2017 Conference on Lasers and Electro-Optics (CLEO), pp. 1-2. IEEE, 2017*.

14. Shang, Kuanping, Shaoqi Feng, **Guangyao Liu**, Siwei Li, and S. J. B. Yoo. "Silicon nitride tri-layer 1× 3 couplers with arbitrary splitting ratio for 3D photonic integrated circuits." In *2017 Optical Fiber Communications Conference and Exhibition (OFC), pp. 1-3. IEEE, 2017*.

15. **Liu, Guangyao**, Kuanping Shang, Siwei Li, Tiehui Su, Yu Zhang, Shaoqi Feng, Roberto Proietti et al. "Low-loss on-chip prism-waveguide coupler to high-Q micro-resonator and optical frequency comb generation." In *Optical Fiber Communication Conference, pp. Tu3K-6. Optical Society of America, 2017*.

16. Shang, Kuanping, Shibnath Pathak, Binbin Guan, **Guangyao Liu**, Shaoqi Feng, and S. J. B. Yoo. "Tri-layer, vertical Y-junction, Si3N4/SiO2 3D photonic integrated circuits with arbitrary splitting ratio." In *2016 Optical Fiber Communications Conference and Exhibition (OFC), pp. 1-3. IEEE, 2016*.

17. Shang, Kuanping, Shibnath Pathak, Binbin Guan, **Guangyao Liu**, Chuan Qin, Ryan P. Scott, and S. J. B. Yoo. "Si3N4 multilayer platform for photonic integrated circuits." In *CLEO: Science and Innovations, pp. STu2F-6. Optical Society of America, 2015*.

18. Shang, Kuanping, Shibnath Pathak, **Guangyao Liu**, and S. J. B. Yoo. "Ultra-low loss vertical optical couplers for 3D photonic integrated circuits." In *Optical Fiber Communication Conference, pp. Th1F-6. Optical Society of America, 2015*.